Global instability of mixing layers created by confinement

Richard Danyi

Submitted in partial fulfilment of the requirements of the degree of Ph.D.

School of Computing and Mathematics, University of Keele.

June 2018

Declaration

I certify that this thesis submitted for the degree of Ph.D. is the result of my own research, except where otherwise acknowledged, and that this thesis (or any part of the same) has not been submitted for a higher degree to any other university or institution.

Signed: .....
(Richard Danyi)

Date: .....

Abstract

This problem is concerned with the inviscid linear stability of parallel stratified shear layer. Most flows do not form well-defined layers, but have density and/or velocity that varies smoothly and continuously with a spatial coordinate. Even in these cases, dividing the flow into layers may be a useful modelling strategy to simplify the equations of motion. A parallel stratified shear layer is where layers of fluid of different density parallel to one another are moving with different speeds creating shear in between them. If the fluid has constant density then we say it is unstratified or homogeneous. Stratified shear layers can arise in the upper oceans, and this motivates our work. We investigate the temporal, absolute and global stability properties of model stratified flows. In temporal instability the disturbances are assumed to be periodic in the streamwise direction, and propagation properties are not determined, it does determine if a flow is stable or unstable. Absolute instability considers propagation of a spatially localized disturbance and determines whether there is a growth in the rest frame or not. Both temporal and absolute instability assume parallel flow. Global instability takes account of variation of the basic flow in the streamwise direction, and determines if there is a growth in the rest frame when the flow is not parallel. Often shear layers develop slowly in the streamwise direction which justifies a local stability approach, i.e. obtaining dispersion relations based on velocity and density profiles found at particular streamwise positions. Streamwise variation of the basic flow is neglected in the local theory, i.e. the flow is assumed to be parallel.

A mixing layer is the region of high shear between two layers of uniform, but different, velocity. The existence of a mixing layer also implies the presence of surrounding uniform (or nearly uniform) flows. Huerre & Monkewitz (1985) showed that

mixing layers become locally absolutely unstable if there is a sufficiently strong reverse flow in one of the two streams, and then, disturbances spread and grow both upstream and downstream. Healey (2009) showed that the presence of boundaries parallel to the shear layer can increase the absolute instability so that even mixing layers without reverse flow can become absolutely unstable. We show that for weakly stratified mixing layers typical of the upper ocean, the sea surface and the sea bed can provide the necessary confinement for the creation of local absolute instability. We also show that absolute instability is sometimes increased by stable stratification. Furthermore, typical bed topographies can create zones of absolute instability parallel to the shoreline that have the potential to act as wavemaker regions for global instability. This mechanism could operate in coastal areas with wind blowing offshore. Results are presented for global instabilities of mixing layers where one layer is essentially stationary, a common scenario in geophysical flows. We consider flows where the distance from mixing layer to a boundary varies slowly with the streamwise coordinate, which can create a pocket of absolute instability, and which in turn can produce global instability. Flows of this type can arise, for example, when wind blows over the sea leading to an upper layer moving at nearly uniform velocity lying above an essentially stationary lower layer, with a relatively thin mixing layer between them. We have identified flows that become globally unstable and on the other hand we have found flows that have a region of absolute instability and yet remain globally stable. It is shown here that typical sea bed topographies can generate global instabilities even when stabilizing stratification is included. It is expected that the appearance of global instability would significantly enhance mixing.

Acknowledgements

Tato prace je venovana mamce Katerine a detem Risankovi, Lukaskovi, Juliance a Jessice, a taky trosku babickam a dedouskovi, aby taky meli.

I would like to thank for the support and patience of my supervisors, Prof Jonathan Healey and Prof Victor Shrira. Thanks to all my colleagues for supporting me throughout the study and thank to Andrew for morning coffee. Thank you to all my family as this would not be possible without their support.

Contents

List of Figures

List of Tables

1 Introduction

The field of hydrodynamic stability goes back to 19th century. The essential problems of hydrodynamic stability were recognized and formulated in the 19th century by Kelvin 1871[1], Helmholtz 1868 [2], Reynolds 1883 [3] and Rayleigh 1879 [4]. Due to the central role in many research areas, the application of stability theory has grown into a mature discipline. For example, hydrodynamic stability analysis is used in modelling the wings of an air plane for drag reduction or in increasing mixing of fuel injected into pistons. In geophysical hydrodynamics mixing in the ocean is very important as the top $2.5m$ of the oceans has the same heat capacity as the whole atmosphere, see Shrira 2015 [5]. In addition mixing in the upper ocean is responsible for providing nutrients into the deeper ocean, where sunlight can not penetrate.

In 1883 Reynolds [3] described a series of experiments on flow in a pipe, which was the first experiment studying hydrodynamic stability. Arrangement was made so that highly coloured water entered clear water as shown in figure 1.1, and the results are shown in figure 1.2. When the flow velocities were sufficiently low, the flow remained laminar as shown in figure 1.2(a). As the flow velocity was increased, at some point the coloured streak would mix with the surrounding fluid as shown in figure 1.2(b). The point of break down approached the trumpet as the flow velocity was increased further and when illuminated by a spark, the mass of mixed coloured fluid resolved into distinct curls, showing eddies, as shown in figure 1.2(c). This experiment lead to the first account of the idea that laminar flows stay laminar at low speeds and then become turbulent at higher speeds, which is the generic pattern seen across all fluid mechanics.

Kelvin , Helmholtz and Rayleigh were among first to study the problem of par-

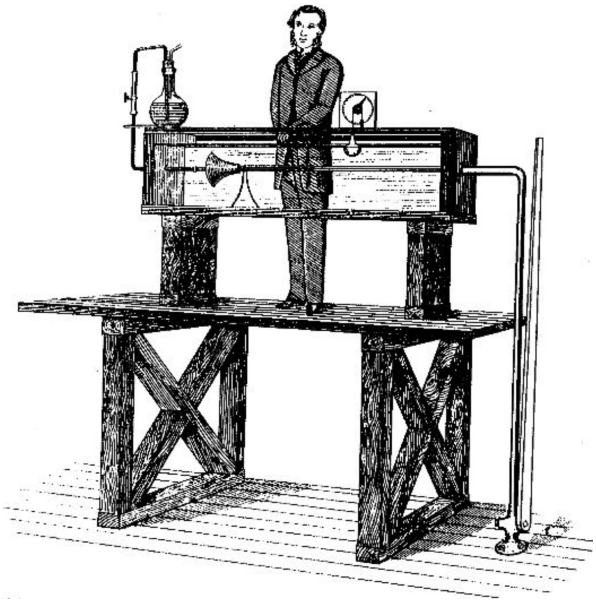

Figure 1.1: Arrangement of Reynolds experiment. Water flows from the tank near the experimenter down to below the ground, through a transparent tube, and dye is injected in the middle of the flow. The turbulent or laminar nature of the flow can therefore be observed precisely. Illustration taken from fluid dynamicist Osborne Reynolds 1883 [3] influential paper on "An experimental investigation of the circumstances which determine whether the motion of water in parallel channels shall be direct or sinuous and of the law of resistance in parallel channels".

allel fluid flow analytically. At the time of Rayleigh the analysis of oscillations and instabilities of a dynamic system of particles and rigid bodies was highly developed. Known solutions of Newton's or Lagrange's equations were perturbed, linearised and the perturbation of each quantity resolved into modes varying in time as e^{st} for some s.

Rayleigh adapted this method of normal modes to model inviscid parallel fluid flow. The essential difference is that the equations are partial rather than ordinary differential equations which leads to many technical difficulties in hydrodynamic stability (see Drazin and Reid 1981 [6]). However, Rayleigh showed that for parallel flow

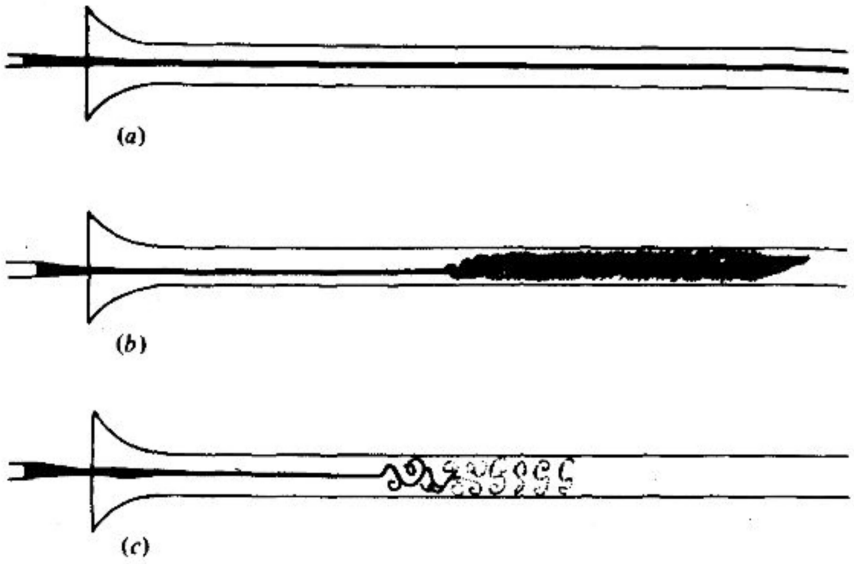

Figure 1.2: Water flow observed in a pipe, as drawn by Osborne Reynolds in his best-known experiment on fluid dynamics in pipes. Water flows from left to right in the transparent tube, and dye (represented in black) flows in the middle. Results from Reynolds experiment show a) laminar flow in a pipe, b) transition to turbulent flow in a pipe, c) transition to turbulent flow as seen when illuminated by a spark.(From Reynolds 1883 [3]).

the equations reduce to an ordinary differential equation. From the times of Rayleigh the subject of hydrodynamic stability has developed through a combination of theory, observations, experiments, and most recently numerical simulations.

The mathematical problem of the stability of a shear layer of homogeneous or stratified fluid flow can be approached by two main methods. One is numerical approximation, which is especially powerful since the invention of the computer, the second is based on analytical techniques such as linearization. Direct Numerical Simulation (DNS) of disturbances is now a common approach and requires specialist dedicated software packages, or considerable expertise in numerical methods to develop Navier-

Stokes solvers, however this has not been attempted here. In our work we use perturbation methods to simplify the governing equations by linearising about parallel basic flow states. The assumption of parallel flow, allows the disturbances to be expressed in terms of normal modes, which reduces the disturbance equations to ordinary differential equations. We consider model flows whose stability can be solved analytically, and also more realistic models that require numerical solutions to the stability equations. In chapter 3 we consider model flows over sea beds that vary slowly in the flow direction and we use WKB theory to study these cases. The flow can then be treated as locally parallel and we identify cases where local and global theories give different results in that a flow can be locally absolutely unstable yet remain globally stable.

The ideas underlying perturbation methods appeared in the early 1800s when there was considerable interest in developing formulas to evaluate special functions. In the 1950s the methods were extended and applied to a wide variety of physical problems with excellent results, for historical development of the method see for example Nayfeh (1973) [7] or Van Dyke (1975)[8]. The numerical solutions considered in this work are for solutions to linearised equations of motion which result in ordinary differential equations (ODE). Numerical solutions can be determined using any mathematical packages such as Mathematica [9] or Matlab [10].

The class of shear layer flows that we study here are motivated by those that arise in the ocean, although the methods described here can be easily adapted to other physical flows, for example in the atmosphere.

1.1 Stratified shear layers

We consider shear layer fluid flow with some velocity profile $U(z)$, with or without some density stratification $\rho(z)$ as shown in figure 1.3. For the case of homogeneous fluid

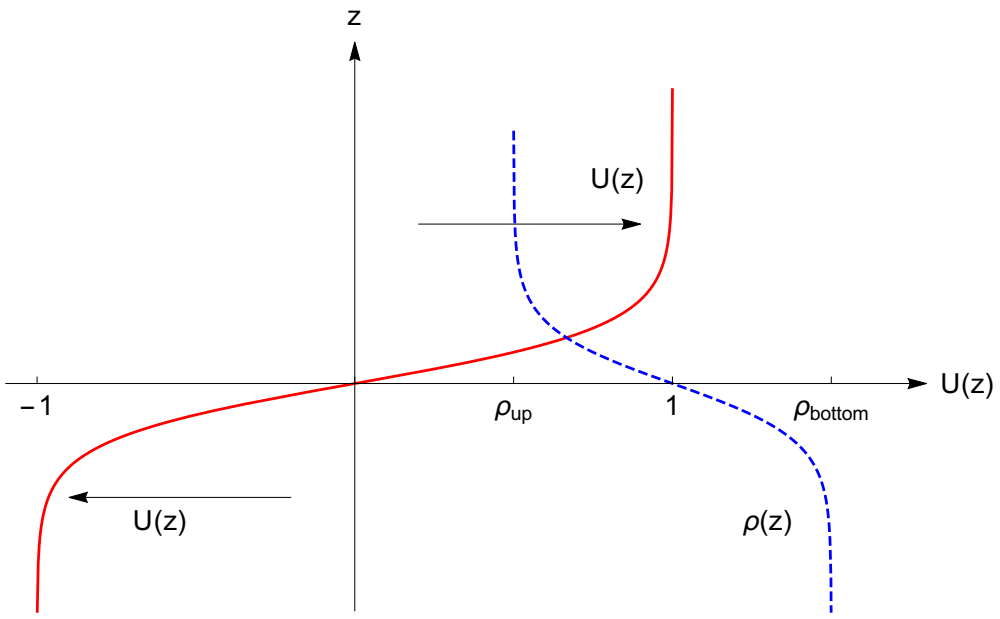

Figure 1.3: Layout of the non dimensional fluid flow with tanh velocity $U(z)$ (red line) and tanh density $\rho(z)$ (blue dashed line) profile.

flow the density profile is constant and does not contribute to the stability analysis.

Consider a fluid particle which has mass m, volume V and density ρ, moving on a streamline with velocity $\bar{u}(\bar{r}, t) = \bar{u}[x(t), y(t), z(t), t]$. We define the rate of change of some quantity of interest $h(x, y, z, t)$ in the fluid motion following the fluid particle as

$\frac{D}{Dt}$ such that

$$\begin{aligned}\frac{Dh}{Dt} &= \frac{d}{dt}h[x(t), y(t), z(t), t] \\ &= \frac{\partial h}{\partial x}\frac{dx}{dt} + \frac{\partial h}{\partial y}\frac{dy}{dt} + \frac{\partial h}{\partial z}\frac{dz}{dt} + \frac{\partial h}{\partial t} \\ &= \frac{\partial h}{\partial t} + \bar{u} \cdot \nabla h. \end{aligned} \tag{1.1}$$

The equations describing this model inviscid flow are equation of motion, continuity and incompressibility. The equation of momentum is

$$\rho\left(\frac{\partial \bar{u}}{\partial t} + \bar{u} \cdot \nabla \bar{u}\right) = -\nabla p + g\rho, \tag{1.2}$$

where g is the acceleration due to gravity and p is the pressure. The second equation needed for the analysis is the equation of incompressibility

$$\int_V \nabla \cdot \bar{u} dV = 0 \implies \nabla \cdot \bar{u} = 0, \tag{1.3}$$

and last equation is simply the representation of mass continuity,

$$\frac{\partial \rho}{\partial t} + \bar{u} \cdot \nabla \rho = 0. \tag{1.4}$$

All together we have equations for momentum, continuity and incompressibility:

$$\left.\begin{aligned}\rho\left(\frac{\partial \bar{u}}{\partial t} + \bar{u} \cdot \nabla \bar{u}\right) &= -\nabla p + g\rho \\ \nabla \cdot \bar{u} &= 0 \\ \frac{\partial \rho}{\partial t} + \bar{u} \cdot \nabla \rho &= 0\end{aligned}\right\} \tag{1.5}$$

Assume that the flow has characteristic length L, characteristic velocity V and characteristic density ρ_0 scales, and we use dimensionless variables based on these scales. Note that the characteristic scales of time, pressure and acceleration are therefore L/V, $\rho_0 V^2$ and V^2/L respectively. We assume that the flow is inviscid, which is relevant for

flows in ocean and atmosphere given their kinematic viscosity ν, typical velocity scales V and typical length scales L. Typical Reynold $Re = VL/\nu$ number in oceanic flow is of order 10^5 and in atmosphere is of order 10^7 (see for example Turner 1973 [11]), which satisfies inviscid flow assumption. We also neglect diffusion of the density field for non-homogeneous flows since the time scale for instabilities to grow is much faster in our considered scenarios.

1.1.1 Non-homogeneous problem and Taylor-Goldstein equation

Consider an arbitrary flow $U(z)$ in the x-direction and arbitrary density distribution $\rho(z)$, as shown in figure 1.3, satisfying some set of boundary conditions and also satisfying equations of motion, incompressibility and continuity.

We let velocity $\bar{u}(\bar{r},t) = (u,v,w)$, pressure $p(\bar{r},t)$ and density $\rho(\bar{r},t)$ be separated into a steady flow/state and an unsteady perturbation:

$$\left.\begin{aligned} \bar{u}(\bar{r},t) &= U(z)\bar{i} + \bar{u}^*(\bar{r},t) \\ p(\bar{r},t) &= p_0 - \tilde{F}^{-2}\int^z \bar{\rho}(z')dz' + p^*(\bar{r},t) \\ \rho(\bar{r},t) &= \bar{\rho}(z) + \rho^*(\bar{r},t) \end{aligned}\right\} \tag{1.6}$$

where $\tilde{F} = V/\sqrt{gL}$ is the Froude's number, and $\bar{u}^* = (u^*, v^*, w^*)$, p^* and ρ^* are the disturbance velocity, pressure and density respectively. For parallel flow we can write the solutions in normal mode form as follows

$$\left.\begin{aligned} \bar{u}^*(x,y,z,t) &= \hat{\bar{u}}(z)\exp[i(\alpha x + \beta y - \omega t)] \\ p^*(x,y,z,t) &= \hat{p}(z)\exp[i(\alpha x + \beta y - \omega t)] \\ \rho^*(x,y,z,t) &= \hat{\rho}(z)\exp[i(\alpha x + \beta y - \omega t)] \end{aligned}\right\} \tag{1.7}$$

where $\omega = \alpha c$. We consider linear stability theory which is justified for small enough disturbances and can predict which disturbances will grow fastest and will then require

non-linear treatment. Linear stability theory is also important because it allows us to classify types of instability and this can give indications about likely transition scenarios, like the appearance of steep-fronted non-linear modes situated at locations where there is a transition from convective to absolute instability (see Huerre 2000 [12]).

Substitute (1.6) and (1.7) into (1.5) and linearise equations by setting non-linear terms $\hat{\gamma}\hat{\gamma}$ and $\hat{\gamma}\hat{\gamma}'$ to zero where $\gamma = u, v, w, p, \bar{\rho}$ to get

$$\left.\begin{aligned}
\bar{\rho}\Big\{-i\omega\hat{u} + U\hat{u}i\alpha + \hat{w}U'\Big\} &= -i\alpha\hat{p} \\
\bar{\rho}\Big\{-i\omega\hat{v} + U\hat{v}i\alpha\big)\Big\} &= -i\beta\hat{p} \\
\bar{\rho}\Big\{-i\omega\hat{w} + U\hat{w}i\alpha\big)\Big\} &= -\hat{p}' - \tilde{F}^{-2}\hat{\rho} \\
i\alpha\hat{u} + i\beta\hat{v} + \hat{w}' &= 0 \\
-i\omega\hat{\rho} + i\alpha\hat{\rho}U + \bar{\rho}'\hat{w} &= 0
\end{aligned}\right\} \tag{1.8}$$

which can be written as

$$i\alpha\bar{\rho}\big(U-c)\hat{u} + \bar{\rho}U'\hat{w} = -i\alpha\hat{p} \tag{1.9}$$

$$i\alpha\bar{\rho}(U-c)\hat{v} = -i\beta\hat{p} \tag{1.10}$$

$$i\alpha\bar{\rho}(U-c)\hat{w} = -\hat{p}' - \tilde{F}^{-2}\hat{\rho} \tag{1.11}$$

$$i\alpha\hat{u} + i\beta\hat{v} + \hat{w}' = 0 \tag{1.12}$$

$$i\alpha(U-c)\hat{\rho} + \bar{\rho}'\hat{w} = 0 \tag{1.13}$$

By elimination of $\hat{u}$ from (1.9), $\hat{v}$ from(1.10), $\hat{p}$ from (1.11), $\hat{\rho}$ from (1.13) and substi-

tuting into (1.12) we get

$$(U-c)\{\hat{w}''-(\alpha^2+\beta^2)\hat{w}\}-U''\hat{w}-\frac{\tilde{F}^{-2}(\alpha^2+\beta^2)\bar{\rho}'}{\alpha^2(U-c)\bar{\rho}}\hat{w}+\frac{\bar{\rho}'}{\bar{\rho}}\{(U-c)\hat{w}'-U'\hat{w}\}=0 \quad (1.14)$$

with conditions at rigid boundaries

$$\hat{w}=0 \text{ at } z=z_1,z_2. \quad (1.15)$$

The use of rigid lid boundaries is satisfied since the time scale of our growing perturbations is of order of minutes, whereas the time scale of surface waves is of order of seconds. In addition the time scale of surface gravity waves is order 1000 times shorter than those of internal gravity waves, because the density differences due to salinity and temperature gradients are so much smaller than the density difference between air and water. This separation of scales allows us to de-couple the branches of the dispersion relation associated with internal waves from those of surface gravity waves, and the rigid-lid boundary condition achieves this by excluding surface gravity waves.

This problem for three-dimensional waves can be reduced to a problem for two dimensional waves by using Squire's [13] transformation, which demonstrates a correspondence between wave numbers (α,β) and $(\sqrt{\alpha^2+\beta^2},0)$. We will consider only two dimensional basic flows which is often a good approximation to flows set in motion by wind induced shear stress, and Squire's theorem proves that two-dimensional disturbances are the first to become unstable(Squire 1933 [13]). We define Froude's number for two dimensional problem using this transformation as

$$F=\frac{\alpha}{\sqrt{\alpha^2+\beta^2}}\tilde{F}, \quad (1.16)$$

leading to

$$(U-c)\{\hat{w}''-\alpha^2\hat{w}\}-U''\hat{w}-\frac{\bar{\rho}'}{F^2(U-c)\bar{\rho}}\hat{w}+\frac{\bar{\rho}'}{\bar{\rho}}\{(U-c)\hat{w}'-U'\hat{w}\}=0 \quad (1.17)$$

For later representation of results of stratified flows we will be using global Richardson number defined as $J_0 = dF^{-2}$, where $d = (\rho_{bottom} - \rho_{top})/(\rho_{bottom} + \rho_{top})$, where ρ_{bottom} and ρ_{top} is the density at the top and bottom of our investigated flow. If $\bar{\rho}'/\bar{\rho} \ll 1$ then we can use the Boussinesq approximation where we neglect the effect of variation of density in the inertia term, but retain the buoyancy term by assuming $\bar{\rho}'/(F^2\bar{\rho}) = O(1)$ and then equation (1.17) reduces to the well known Taylor-Goldstein equation (see Drazin and Ried 1981 [6] or Turner 1973 [11]):

$$(U-c)\{D^2\phi - \alpha^2\phi\} - U''\phi - \frac{\bar{\rho}'}{F^2(U-c)\bar{\rho}}\phi = 0, \tag{1.18}$$

where ϕ is the eigenfunction and c is the eigenvalue. The boundary conditions are

$$\alpha\phi = 0 \quad \text{at} \quad z = z_1, z_2 \tag{1.19}$$

where

$$\hat{u} = \phi' \quad \text{and} \quad \hat{w} = -\mathrm{i}\alpha\phi \tag{1.20}$$

and

$$\psi^* = \phi(z)\mathrm{e}^{\mathrm{i}\alpha(\mathrm{x}-\mathrm{ct})}. \tag{1.21}$$

The homogeneous boundary conditions (1.19) define an eigenvalue problem relating α, c and F. In our investigation we will consider stratification which satisfies the Boussinesq approximation and therefore the Taylor-Goldstein equation (1.18) will be the basis of our stability calculations.

Note that if the density $\bar{\rho}$ is constant, then $\bar{\rho}' = 0$, and the Taylor-Goldstein equation (1.18) reduces to Rayleigh equation,

$$(U-c)(\phi'' - \alpha^2\phi) - U''\phi = 0. \tag{1.22}$$

The eigenvalue problem can be expressed as a dispersion relation written in the form $\Delta(\alpha, \omega) = 0$. We shall first consider real α and solve the dispersion relation for

ω, which is called temporal stability theory. If $\omega_i > 0$ for some real α then this wave number is unstable and its amplitude grows in time as explained below

$$\omega = \omega_r + \mathrm{i}\omega_\mathrm{i}, \tag{1.23}$$

where ω_r and ω_i are the real and imaginary parts of the frequency, giving

$$\begin{aligned} \mathrm{e}^{\mathrm{i}(\alpha \mathrm{x} - \omega \mathrm{t})} &= \mathrm{e}^{\mathrm{i}(\alpha \mathrm{x} - \omega_\mathrm{r} \mathrm{t} - \mathrm{i}\omega_\mathrm{i} \mathrm{t})} \\ &= \mathrm{e}^{\omega_\mathrm{i} \mathrm{t}} \mathrm{e}^{\mathrm{i}(\alpha \mathrm{x} - \omega_\mathrm{r} \mathrm{t})}. \end{aligned} \tag{1.24}$$

1.2 Review of piecewise-linear approximations to stratified shear layers

Consider first the homogeneous problem (1.22). The main difficulty in solving (1.22) analytically arises because of the $z-$ dependence of the coefficients of ϕ and ϕ''. However in the special case where U is linear, i.e. $U = a + bz$ for some constants a, b, we have $U'' = 0$ and (1.22) can be reduced to

$$\phi'' - \alpha^2 \phi = 0, \tag{1.25}$$

which has general solution

$$\phi = A\mathrm{e}^{\alpha \mathrm{z}} + \mathrm{B}\mathrm{e}^{-\alpha \mathrm{z}}. \tag{1.26}$$

If an arbitrary basic velocity profile $U(z)$ is approximated using piecewise-linear profile then the dispersion relation can be obtained in closed form as a polynomial in c. To solve the Rayleigh equation with piecewise-linear velocity profile we will need to apply the matching conditions that relate the solution in one layer to the solution in an adjacent layer. The layers are defined by junctions between two linear segments of piecewise linear velocity profile $U(z)$. There are two matching conditions for Rayleigh's

equation. In both cases we assume that $U - c \neq 0$ near the junction. First rewrite Rayleigh's equation (1.22) as

$$[(U-c)\phi' - U'\phi]' - \alpha^2(U-c)\phi = 0. \tag{1.27}$$

Integrate equation (1.27) across a junction between two linear segments at $z = z_0$ from $z_0 - \epsilon$ to $z_0 + \epsilon$ and let $\epsilon \to 0$

$$\lim_{\epsilon\to 0}\int_{z_0-\epsilon}^{z_0+\epsilon}[(U-c)\phi' - U'\phi]'dz = \lim_{\epsilon\to 0}\int_{z_0-\epsilon}^{z_0+\epsilon}\alpha^2(U-c)\phi dz \quad \text{at} \quad z = z_0. \tag{1.28}$$

The right hand side of (1.28) is zero hence we get the first matching condition

$$\Delta[(U-c)\phi' - U'\phi] = 0 \quad \text{at} \quad z = z_0, \tag{1.29}$$

where $\Delta[\ ]$ represents the change in a quantity across a junction. The matching condition (1.29) corresponds to continuity of pressure, as can be seen from (1.9), and is called the dynamic condition.

The second matching condition can be obtained from writing (1.9) as

$$\left(\frac{\phi}{U-c}\right)' = -\frac{\hat{p}}{(U-c)^2}. \tag{1.30}$$

We integrate across the discontinuity at $z = z_0$ from $z_0 - \epsilon$ to $z_0 + \epsilon$ and let $\epsilon \to 0$ which will give the second matching condition

$$\lim_{\epsilon\to 0}\int_{z_0-\epsilon}^{z_0+\epsilon}\left[\frac{\phi}{U-c}\right]' dz = \lim_{\epsilon\to 0}\int_{z_0-\epsilon}^{z_0+\epsilon} -\frac{\hat{p}}{(U-c)^2} \text{ at } z = z_0 \tag{1.31}$$

giving

$$\Delta\left[\frac{\phi}{U-c}\right] = 0 \text{ at } z = z_0, \tag{1.32}$$

Which is called the kinematic condition, and corresponds to the interface moving with the fluid on either side of the interface. Applying these matching conditions to a given basic flow $U(z)$ together with boundary conditions, a dispersion relation can be

determined for the given problem which will then be used in further analysis or for comparison of results from smooth velocity profiles.

The simple treatment of inhomogeneous flows requires modelling the flow as having piecewise-constant density with jumps in density. The problem with uniform density gradients can be solved, but requires special functions, and the properties of the resulting dispersion relation are difficult to interpret, and so numerical solutions may as well be used instead. In the case of piecewise-constant approximations of the density profile $\bar{\rho}(z)$ the matching conditions at junctions can be derived in the same way as in the case of homogeneous flow (see Appendix A). The matching conditions for stratified flow are

$$\Delta[\bar{\rho}(U-c)\phi' - \bar{\rho}U'\phi - \frac{\bar{\rho}g\phi}{U-c}] = 0 \quad \text{at} \quad z = z_0, \tag{1.33}$$

and, as in homogeneous case,

$$\Delta\left[\frac{\phi}{U-c}\right] = 0 \text{ at } z = z_0. \tag{1.34}$$

The first person to consider stability of a stratified shear layer was Kelvin 1871 [1]. Kelvin considered basic flow given by

$$U(z) = \begin{cases} U_1 & : z > 0 \\ U_2 & : z < 0 \end{cases} \tag{1.35}$$

and

$$\rho(z) = \begin{cases} \rho_1 & : z > 0 \\ \rho_2 & : z < 0 \end{cases} \tag{1.36}$$

as shown in figure 1.4. Note that in the problem considered by Kelvin there is no natural length scale so we can not nondimensionalize and hence this problem is considered in dimensional variables. Applying the matching conditions allows dispersion relations for general piecewise-linear velocity profiles and piecewise-constant density profiles to be

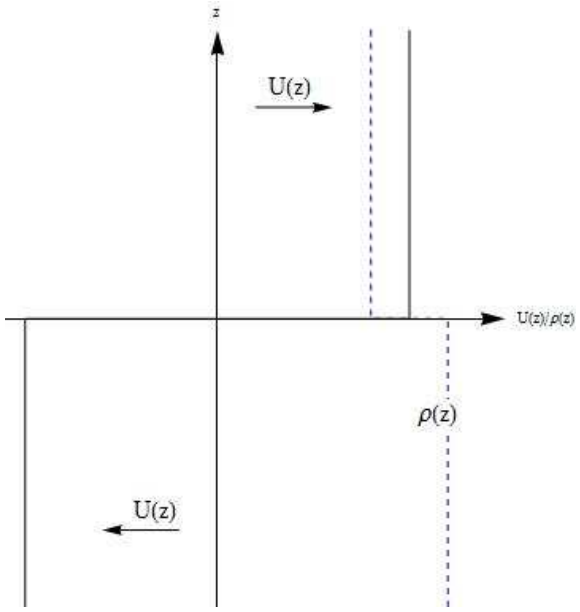

Figure 1.4: Set-up of the stratified shear flow using piecewise linear profiles considered by Kelvin in 1871 [1]). $U(z)$ (black solid line) is the velocity profile and $\rho(z)$ (black dashed line is the density profile.

conveniently obtained by substituting (1.26), (1.35) and (1.36) into the jump conditions and eliminating unknown constants. Kelvin derived the dispersion relation

$$c = \frac{-\rho_1 U_1 + \rho_2 U_2}{\rho_1 + \rho_2} \pm \sqrt{-\rho_1 \rho_2 \left(\frac{U_2 - U_1}{\rho_1 + \rho_2} \right)^2 + \frac{g}{\alpha} \frac{\rho_2 - \rho_1}{\rho_1 + \rho_2}}. \tag{1.37}$$

and concluded that a necessary and sufficient condition for instability is

$$g(\rho_2^2 - \rho_1^2) < \alpha \rho_1 \rho_2 (U_1 - U_2)^2 \tag{1.38}$$

where α is the wave number in the x direction and g is the acceleration due to gravity in the z direction. The condition (1.38) implies instability for all wavelengths for homogeneous flow, and for short enough waves for inhomogeneous flow. In the case of homogeneous flows, it can be shown that a finite thickness shear layer stabilizes short waves (see chapter 2 and Drazin [6]), which motivated later studies to include

finite thickness shear layers in stratified flows by Taylor, Holmboe, Lawrence, Caulfield, among others. The modelling of a finite thickness shear layer and a finite thickness density layer is difficult if we only use piecewise-constant density profiles. Taylor 1931 [14] and Holmboe 1962 [15] used two different models, and found that the effect of a finite thickness shear on stratified (inhomogeneous) flow is non-trivial, with different behaviour in each case.

Taylor in 1931 [14] considered the stability of a multi-layered stratified shear layer. He considered the piecewise linear velocity and density profiles shown in figure 1.5, where

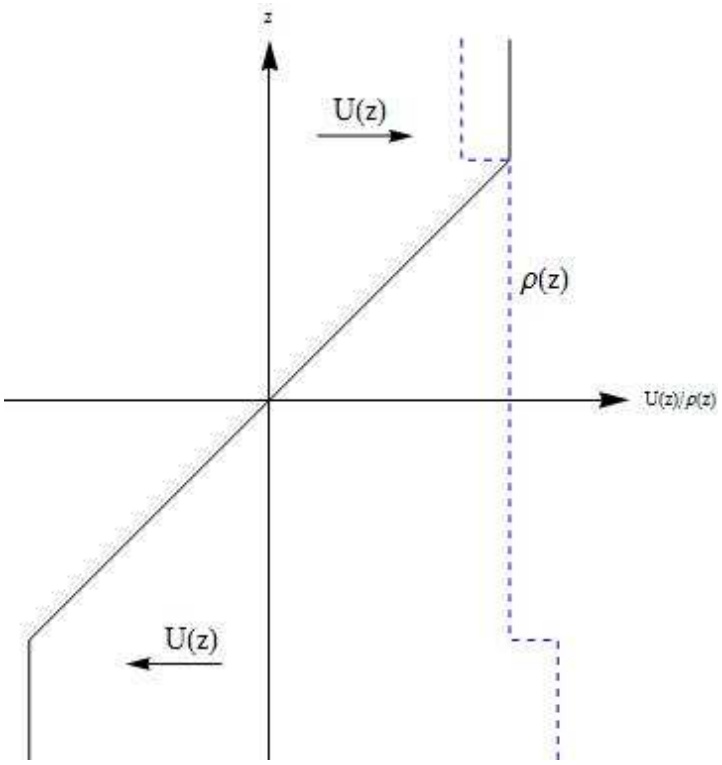

Figure 1.5: Set-up of the stratified shear flow using piecewise linear profiles considered by Taylor in 1931 [14]). $U(z)$ (black solid line) is the velocity profile and $\rho(z)$ (black dashed line is the density profile.

$$U(z) = \begin{cases} -\frac{1}{2}\Delta U & : z \leq -\frac{1}{2}d \\ \Delta U z/d & : -\frac{1}{2}d \leq z \leq \frac{1}{2}d \\ \frac{1}{2}\Delta U & : z \geq \frac{1}{2} \end{cases} \tag{1.39}$$

where d is the thickness of the shear, and

$$\rho(z) = \begin{cases} \rho + \Delta\rho & : z \leq -\frac{1}{2}d \\ \rho + \frac{1}{2}\Delta\rho & : -\frac{1}{2}d \leq z \leq \frac{1}{2}d \\ \rho & : z \geq \frac{1}{2} \end{cases} \tag{1.40}$$

Normal mode analysis (see for example Drazin and Reid 1981 [6] or Turner 1973 [11]) together with the use of piecewise linear profiles results in analytically derived dispersion relation (relation between the real and imaginary part of wave speed c_r, c_i and wave number α, where αc_i is the growth rate of the wave ω_i). The dispersion relation derived by Taylor for velocity profile $U(z)$ and $\rho(z)$ defined by (1.39) and (1.40) is

$$\begin{aligned} c^4 + \left(\frac{\mathrm{e}^{-4\alpha} - (2\alpha - 1)^2}{4\alpha^2} - 1 - \frac{Ri_0}{\alpha} \right) c^2 + \frac{Ri_0^2}{4\alpha^2}(1 - \mathrm{e}^{-4\alpha}) \\ - \frac{Ri_0}{\alpha} \left(\frac{(2\alpha - 1) + \mathrm{e}^{-4\alpha}}{2\alpha} \right) - \left(\frac{\mathrm{e}^{-4\alpha} - (2\alpha - 1)^2}{4\alpha^2} \right) = 0 \end{aligned} \tag{1.41}$$

which for $\mathrm{Im}(c) > 0$ implies

$$\frac{2\alpha}{1 + \mathrm{e}^{-2\alpha}} < 1 + Ri_0 < \frac{2\alpha}{1 - \mathrm{e}^{-2\alpha}}, \tag{1.42}$$

where $Ri_0 = (g\Delta\rho d)/(\rho\Delta U^2)$ is the global Richardson number as defined by Kelvin.

The dispersion relation (1.41) can be used to represent the stability boundary (i.e. the curve in (α, Ri_0) space dividing growing modes from stable modes as shown in figure 1.6, where α is the wave number and Ri_0 is the global Richardson number (also called the bulk Richardson number) characterising the stratified flow. We will refer to these modes as T modes after Taylor. The results of Taylor's analysis, shown in figure 1.6, predict that all unstable T modes have $c_r = 0$ and propagate at the mean speed of the shear layer. Taylor also observed that as $Ri_0 \to \infty$ the neutral curves asymptote to the line $Ri_0 = 2\alpha - 1$, which implies that there is a instability for

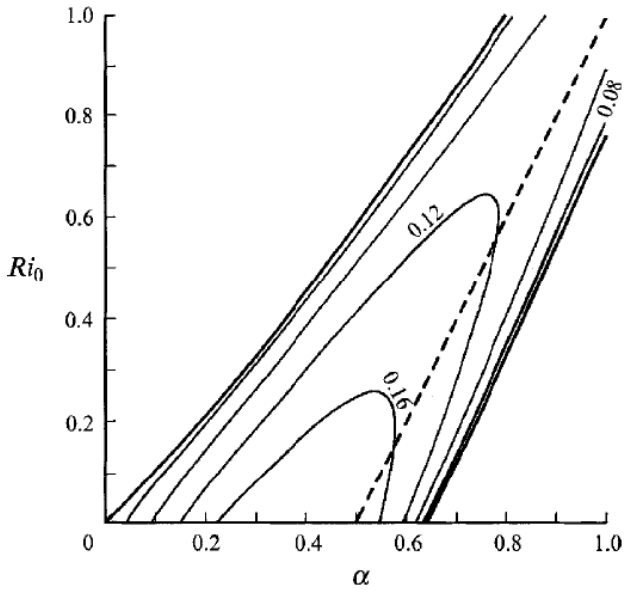

Figure 1.6: Temporal stability boundary for the velocity and density profiles given by equation (1.39) and (1.40). Unstable region is bounded by neutral curve (solid thick line with zero growth rate) with contours of growth rate (solid line) for the three-layer flow considered by Taylor [14]. The figure is taken from Caulfield 1993 [16]. The neutral curves asymptote towards the dashed line, defined in the text.

arbitrarily short waves, unlike in the homogeneous case which becomes stable for short waves. In comparison with Kelvin's result, where for instability the condition 1.38 needs to be satisfied, Taylor's results shows instability for all Richardson's numbers Ri_0. In this sense the stable stratification has a destabilizing effect. Destabilisation of the temporal instability by introducing stratification therefore goes back to Taylor, but we are not aware of a corresponding result for absolute instability being obtained before, and the possibility of such behaviour is explained in chapter 4.

Another important model of stratified shear layers was studied by Holmboe in 1962 [15]. Holmboe considered the piecewise linear velocity and density profiles shown in figure 1.7 with

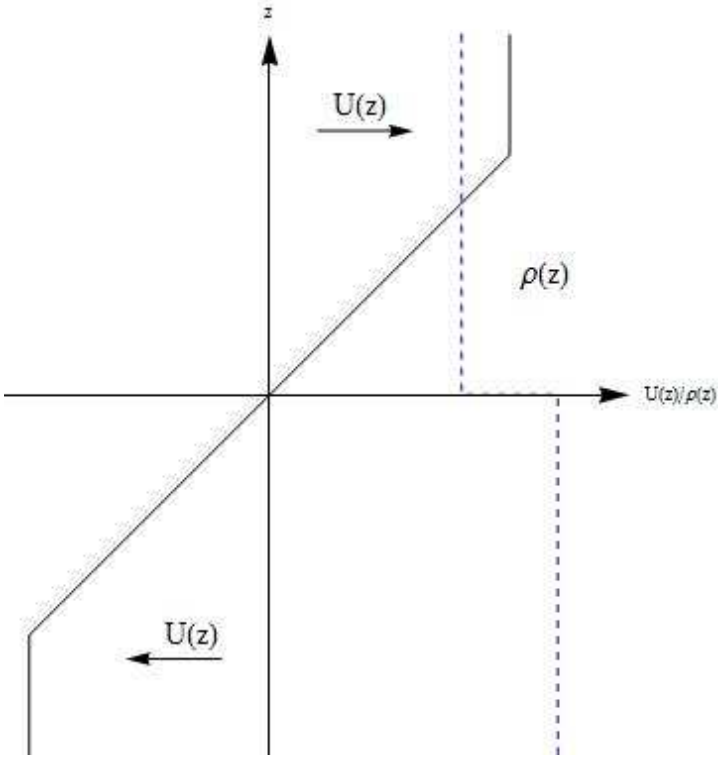

Figure 1.7: Set-up of the stratified shear flow using piecewise linear profiles considered by Holmboe in 1962 [15]. $U(z)$ (black solid line) is the velocity profile and $\rho(z)$ (black dashed line is the density profile.

$$U(z) = \begin{cases} -\frac{1}{2}\Delta U & : z \leq -\frac{1}{2}d \\ \Delta U z/d & : -\frac{1}{2}d \leq z \leq \frac{1}{2}d \\ \frac{1}{2}\Delta U & : z \geq \frac{1}{2} \end{cases} \tag{1.43}$$

where d is the thickness of the shear, and density given by

$$\rho(z) = \begin{cases} \rho + \Delta\rho & : z \leq 0 \\ \rho & : z > 0. \end{cases} \tag{1.44}$$

Following the normal mode analysis (as in the Taylor problem) a dispersion relation can be obtained and is found to be

$$c^4 + \left(\frac{\mathrm{e}^{-4\alpha} - (2\alpha - 1)^2}{4\alpha^2} - \frac{Ri_0}{\alpha} \right) c^2 + \frac{Ri_0^2}{\alpha^2} (\frac{\mathrm{e}^{-2\alpha} + (2\alpha - 1)^2}{2\alpha})^2 = 0. \tag{1.45}$$

The results for the neutral curves, which divide growing modes from stable modes in the parameter space, is shown in figure 1.8, where $Ri_0 = (g\Delta\rho d)/(\rho\Delta U^2)$ is the global Richardson number characterising the stratified flow. We will refer to these modes as H modes after Holmboe. In this flow the density interface does not coincide with a

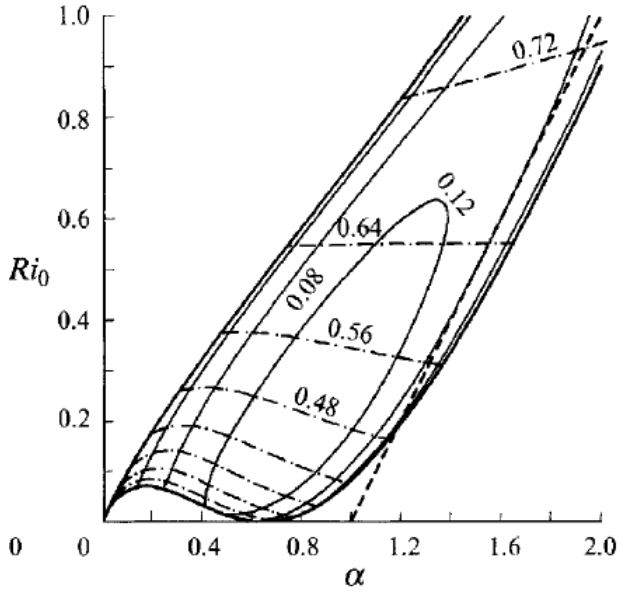

Figure 1.8: Stability boundary for the three-layer flow considered by Holmboe in 1962 [15]. The thin solid lines give contours of the growth rate, the dash-dotted lines give contours of phase velocity, and the region just above the $\alpha-$axis at small α has a unstable waves of zero phase velocity. Unstable region is bounded by neutral curves (solid thick lines with zero growth rate) and they asymptote towards the dashed line as $\alpha \to \infty$. The figure is taken from Caulfield 1993 [16].

velocity interface, and there are two Rayleigh waves (one at each vorticity interface) and two internal gravity waves on the density interface with opposite phase speed. As shown in figure 1.8 for small $Ri_0 < 0.07$ there are unstable modes with zero phase speed which can be interpreted as a stratified modification of Rayleigh homogeneous problem leading to Kelvin-Helmholtz instabilities. As stratification increases the unstable modes

start to have non-zero phase speed. These H modes propagate with the same speed but in opposite directions. It can also be deduced from figure 1.8 that for large Ri_0 and large α the neutral curves asymptote to the line $Ri_0 = \alpha - 1$, which implies that there is a instability for arbitrarily short waves, but it differs to the results of Taylor, where the asymptote is given by $Ri_0 = 2\alpha - 1$.

On comparison of the results of Taylor and Holmboe (as presented in figures 1.6 and 1.8 we can conclude that although T modes have a grater growth rates, the H modes are covering grater range of unstable wave numbers α for given global Richardson number Ri_0. Summarising the work of Taylor 1931 [14] and Holmboe 1962 [15] we can say that, when the thickness of the intermediate density layer coincides with that of the shear layer this results in unstable T modes. When the density changes over a much thinner layer than the velocity, this results in unstable H modes (see also Caulfield 1993 [16] for more detailed analysis of Taylor's 1931 and Holmboe's 1962 work).

1.3 Numerical solutions to Rayleigh and Taylor-Goldstein equation

The advantage of obtaining numerical solutions to the Taylor-Goldstein equation is that they can be applied to all profiles at all wavelengths and include critical layer effects (at critical point $U(z) = c$), which are neglected in the piecewise-linear theory, but play an important role in the more physically realistic curved profiles, and can produce qualitatively different behaviour. For example we do not obtain complex conjugate pairs of roots for smooth profiles, but we do for piecewise-linear profiles. There are many ways to solve the Rayleigh or Taylor-Goldstein equations numerically such as finite-difference method or initial-value method (also known as shooting method). The

initial values of the wave-number and the complex phase speed used in shooting methods, must be sufficiently close to the eigenvalues for the method to converge. Good initial guesses can be obtained from piecewise linear theory. In our investigation we will use numerical methods for solving the Rayleigh and Taylor-Goldstein equation for obtaining stability results at arbitrary wavelengths and use shooting methods to obtain eigenvalues. We will use the package Mathematica and its command NDSolve [9] which initially analyses the differential equation for the most suitable method and then uses it to obtain the solution to some given accuracy (see appendix C for the code). To verify the use of NDSolve we will compare the result with the analytical approach and on one occasion with a numerical code using Matlab [10] (see also Schmid [17]) and furthermore in chapter 3 with piecewise linear results. Numerical approaches overcome the limitations of analytical methods and allows many more problems to be studied. Numerical methods for temporal and absolute stability are discussed in chapter 2, and numerical methods for global stability are discussed in chapter 3.

1.4 Absolute instabilities in mixing layers

A parallel flow is absolutely unstable if growing disturbances propagate both upstream and downstream from the disturbance source, and is convectively unstable if they only grow as they propagate away from the source.

Absolute stability analysis is very useful since it allows us to fix our frame of reference and determine whether perturbations grow or decay in the chosen frame of reference. There are physical consequences for the flow depending on whether disturbances propagate away from their source or not. If the flow is exactly parallel the absolute/convective instability is only a consequence of our choice of frame of refer-

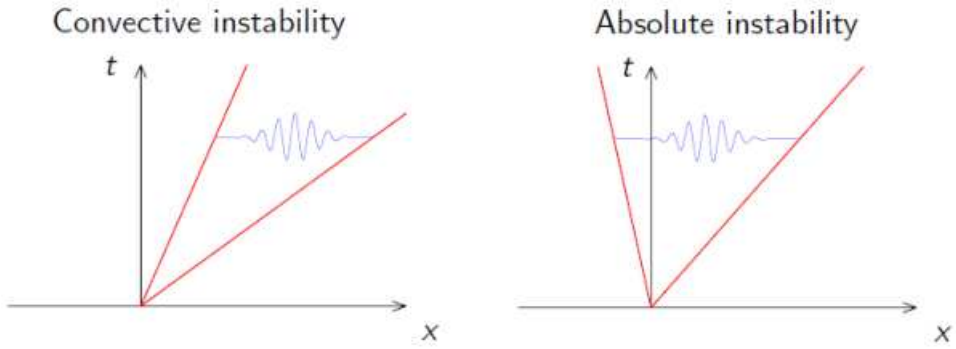

Figure 1.9: Results of local convective and local absolute instability in parallel shear layers. If the disturbance grows in time as it propagates away, eventually leaving the flow undisturbed in the frame of reference, the flow is locally convectively unstable (diagram on the left). If the disturbance grows in time everywhere, eventually destroying the velocity profile in the frame of reference, the flow is locally absolutely unstable (diagram on the right).

ence. But flows of practical interest nearly always have a weak spatial variation, and the relevant frame of reference is not arbitrary, but fixed by the flow. In this case parallel flow theory gives a good first approximation to the global instability properties of weakly non-parallel flow and it is the global stability properties that determine the dynamics that will be observed (see chapter 3 for global instabilities). The methods for calculating absolute instability will be described in chapter 2, but quantitative results of an absolute stability analysis are shown in figure 1.9. If the perturbations are growing and propagating away from our frame of reference leaving the initial flow unperturbed and laminar then this is convectively unstable flow. If on the other hand we find growing perturbations in the fixed frame of reference, then this is absolutely unstable flow. Absolute growth will mix the flow and destroy the initial density and velocity profiles in the fixed frame of reference. These properties are to determined using Briggs saddle point method which is discussed in chapter 2 (see also Briggs 1964

[18]).

Heurre and Monkewitz (1985) [19] applied Brigg's method to an unconfined inviscid plane mixing layer, and found that the flow only becomes absolutely unstable when the two layers flow in opposite directions and the reverse flow is sufficiently strong. Heurre and Monkewitz (1990) [20] introduced the concept of global instability for flows that vary slowly in the streamwise direction, and found in particular that absolute instability is necessary for global instability, but not sufficient. These concepts for global instability have not been used widely in geophysical fluid dynamics, perhaps because mixing layers with sufficiently strong reverse flow are not common.

However, Healey (2007) [21] showed that if the saddle point controlling absolute instability in an unconfined flow approaches, or crosses, the imaginary axis in the wavenumber plane then confinement by boundaries parallel to the flow will have a destabilising effect. Among the flows in which the saddle behaves in this way, is the mixing layer of Huerre and Monkevitz (1985) [19]. Effects of confinement on the absolute instability of mixing layers were investigated in Healey (2009) [22] (see also Arratia, Mowlavi and Gallaire 2017 [23] and Juniper 2006 [24], 2007 [25]), where it was found that the destabilising effect can be strong enough for even co-flow mixing layers, where both streams are in the same direction, to become absolutely unstable. In chapter 2 we investigate the destabilizing effect of adding boundaries for stably stratified flows, and find the maximum stable stratification for absolutely unstable co-flow.

1.5 Global instability in mixing layers

Global instability is closely associated with local absolute instability. Existence of a global instability depends sensitively on both the nature of the streamwise depen-

dence of the basic flow, and on the propagation properties predicted by local dispersion relation (local meaning applying at a particular location). Consider first a wavy disturbance added to an arbitrary basic flow where wavelengths are short compared to the streamwise distances over which the basic flow varies. The behaviour of disturbances at a given streamwise location can be found to a first approximation by ignoring the streamwise variation of the basic flow (the parallel flow approximation). This local dispersion relation is determined by the basic flow characteristics at the streamwise location of interest. Sometimes, the streamwise variation of the local properties is such that an unstable global mode is created, which has complex frequency selected by the requirement that the disturbance envelope decays both upstream and downstream. The methods for calculating global instability will be described in chapter 3.

In particular, for envelopes that decay to zero as $X \to \pm\infty$, it was shown by Soward and Jones (1983) [26] that the most unstable (or least damped) global mode corresponds to the double saddle condition

$$\frac{\partial \omega}{\partial \alpha} = 0, \frac{\partial \omega}{\partial X} = 0, \tag{1.46}$$

where a mode that decays in the upstream direction connects to a mode that decays in the downstream direction. See the reviews by Huerre and Monkewitz (1990) [19] and Huerre and Rossi (1998) [27] for further applications of these criteria in shear flows.

The streamwise location $X = X_s$, where the saddle condition (1.46) is satisfied, acts as the wave-maker region for the flow. The global frequency is equal (at leading order) to the absolute frequency at X_s, and this identification of the global frequency with the absolute frequency at X_s is seen through the same condition appearing in both (2.21) and (1.46). A key observation is that, in general, X_s lies in the complex X plane off the real axis. This means that it is possible for absolute instability to exist along some interval of the real X axis, i.e. there is a region of absolute instability in

the physical flow, and yet simultaneously the flow will be globally stable if $\mathrm{Im}(\omega) < 0$ at $X = X_s$. Therefore, the appearance of a region of absolute instability is necessary, but not sufficient, for the existence of global instability in a slowly varying basic flow. We find examples of bottom topography for which the local dispersion relations are absolutely unstable over a finite streamwise region, and yet the flow will remains globally stable. We also obtain neutral curves for global instability for other topographies. As well as these theoretical approaches Davies and co-workers have investigated global instabilities on rotating disk using direct numerical simulations DNS (see Davies and Carpenter 2003 [28], Davies and Thomas 2007 [29], 2010 [30], 2013 [31], 2016 [32]) and found examples of where the flow was absolutely unstable, but globally remained stable. In chapter 3 we show similar result, using linear stability analysis (as DNS is not in the scope of this thesis), for parallel flows, where the flow with linearly varying bottom boundary is absolutely unstable, but remains globally stable.

The stability of density-stratified shear flows confined between two horizontal boundaries has been intensively studied since the times of Helmholtz and Rayliegh, and much is known about the linear instability of these flows, see Turner (1973) [11], Drazin and Reid (1981)[6] or Chandrasekhar (1961) [33]. However in almost all physical contexts where stratified shear flow occurs, a boundary producing confinement, e.g. the sea bed in an oceanic flow, is not parallel to the shear layer, and this problem has received much less attention. Nonetheless, non-parallel confinement is hugely important for geophysical flows where issues of mixing and vertical transfer of heat and momentum are central, especially for physical oceanography, from where we choose our main examples. Non-parallel confinement of mixing layer also arises in many industrial contexts.

Consider a typical situation on the continental shelf with seasonal pycnocline

(a layer of strong density gradient) separating the mixed layer adjacent to the free surface from more dense fluid below. A light steady wind directed offshore creates a drift current decaying with depth with the maximal shear localised in the pycnocline. The total fluid depth is slowly increasing with the distance from the shore. Under such conditions one can often see a quite distinct strip parallel to the coast. Such a strip is visualized due to the sharp contrast in surface, similar to the visualisation of a ship wake. Often such turbulent streaks are caused by breaking of shoaling internal waves, but sometimes the origin remains a mystery, see Soloviev & Lukas (2014) [34]. We show here that under realistic conditions these flows can become absolutely unstable at certain distances from the shore, and we investigate the sea-bed topographies that lead to global instabilities. These instabilities enhance the mixing and promote subsurface turbulence and so could provide the mechanism responsible for the observations of turbulent strips parallel to the coast. This motivates the present investigation of generic global instability of stratified shear flow confined between the two nearly parallel boundaries.

The significance of the distinction between absolute and global stability lies in the fact that even if a basic flow is unstable, it can persist essentially unchanged in a region of interest if unstable waves convect away from downstream fast enough. Such flow is globally stable, despite the presence of unstable waves. Most boundary layers show this behaviour, where the transition Reynolds number, which depends sensitively on the background disturbance environment, can be much larger than the critical Reynolds number for instability. On the other hand, if flow is globally unstable, then arbitrarily small disturbances grow in the region of interest and the basic flow is eventually destroyed. Mixing is greatly enhanced by the presence of a global instability.

Matas, Marty and Cartellier (2011) carried out a set of mixing layer experiments

and compared the results with frequency selection and growth rates from linear stability theory, but found discrepancies between theory and experiments. They did not, however, include confinement effects (which are usually expected to be weak or stabilising). Matas (2015) [35] then included confinements effects in the analysis for these flows, and found some dramatic improvements in the agreement between experiment and the modified theory. For example, a flow, when treated as unconfined, was found to be convectively unstable, with a most unstable wave frequency $66Hz$. When the confinement that was present in the experiment was included in the analysis, the same flow was found to be absolutely unstable with an absolute frequency $28Hz$, agreeing much better with the frequency observed in the experiment, which was $28.8Hz$. This illustrates the important effect of confinement on the stability of mixing layers.

Mixing layers where one layer is stationary arise in geophysical flows, and so if they are suitably confined they can become absolutely unstable. If these basic flows evolve slowly in the streamwise direction then there is the possibility of global instability, which could significantly increase the rate of mixing. In this thesis, models for flows produced when wind blows over a shallow sea are considered in which wind stress at the sea surface generates a mixed layer of approximately uniform velocity and density of certain depth, and below this depth the water is essentially stationary. There is then a mixing layer between the mixed layer and the stationary layer, and the sea surface (modelled as flat and undisturbed), together with the sea bed, create the confinement that can lead to global instability for some sea-bed topographies.

The simplest model exhibiting the main features is presented in chapter 3, in which the structure of the mixing layer is ignored, and replaced by a vortex sheet, and in which density stratification is also ignored. In this idealised context we explore non-parallel effects on local convective instabilities, and then focus on the ranges of

confinement that produce local absolute instability, and investigate the topographies that do, and do not, generate global instabilities. The effects of stable stratification are also included. As expected, stable stratification tends to stabilize the global instability, and we identify the strongest stratifications for which global instability persists. We show that smooth profiles not only stabilize short waves, but can simultaneously destabilize the global instability and extend the parameter regimes susceptible to global instability.

Often in nature the stratified flows are such that the strong velocity shear is displaced from the strongest density gradient which motivates our investigation into such problems, and which is presented in chapter 4. Previous research on this topic considered unbounded flows and the analysis was only temporal or spatial. Lawrence, Browand and Redekopp in 1991 [36] investigated the stability of stratified shear flow when the region of strongest velocity shear is of greater thickness then the region of strongest density gradient, corresponding to the situation studied in Holmboe 1962 [15], see figure 1.7. Lawrence et al allowed the density interface to be displaced with respect to the centre of velocity shear by an amount ϵ. They used piecewise-linear theory to derive a quartic dispersion relation with coefficients depending on the profile asymmetry parameter ϵ , the bulk Richardson number Ri_0, and wave number α. In the limit when $\epsilon = 0$ they reproduced the result of Holmboe 1962 [15] that there are two unstable modes which propagate with the same phase speed but in opposite directions. When the symmetry of the Holmboe problem is broken (i.e. $\epsilon \neq 0$) then there are still two propagating waves in opposite directions but this time they differ in phase speed. A series of experiments were conducted, but the H-modes were not observed. For detailed analytical and experimental results see Lawrence, Browand and Redekopp 1991 [36].

However, we have found that when confinement is included so as to produce absolute instability, the effect of displacing vertically the velocity and density gradients can be destabilizing. In fact, the absolute instability of a suitably placed stable stratification can be grater than the absolute instability of the corresponding homogeneous flow. Conclusions are presented in chapter 4.

2 Absolute stability analysis for stratified parallel flows

2.0.1 Initial value problems

Consider a parallel flow problem where the flow is taken to be initially undisturbed, and then an impulsive disturbance is introduced. Its progress can be followed upstream/downstream and at any subsequent finite time the disturbance only extends over a finite part of the flow, so its energy remains finite. The impulse problem is solved using integral transforms, and the principle of causality must be applied.

The key ideas can be illustrated by giving a pendulum that is hanging at rest (see Healey 2017 [37]), a sharp knock

$$\frac{d^2y}{dt^2} + \Omega^2 y = v_0\delta(t) \tag{2.1}$$

where $\delta(t)$ is the Dirac delta function, v_0 is a constant, and the constant Ω is the natural frequency. The impulse (sharp knock) transfers finite momentum to the pendulum, and causes it to start swinging.

Solution by elementary methods

The impulse response can be obtained by considering

$$\frac{d^2y}{dt^2} + \Omega^2 y = v_0 f(t), \qquad f(t) = \begin{cases} 0 & \text{for } t \leq 0 \\ 1/\epsilon & \text{for } 0 \leq t \leq \epsilon \\ 0 & \text{for } t \geq \epsilon \end{cases} \tag{2.2}$$

as $\epsilon \to 0$. For $t \leq 0$, $y = 0$ (pendulum undisturbed before the impulse). For $0 \leq t \leq \epsilon$ we get

$$\frac{d^2y}{dt^2} + \Omega^2 y = \frac{v_0}{\epsilon}, \qquad y(0) = y'(0) = 0, \tag{2.3}$$

with solution

$$y = \frac{v_0}{\epsilon\Omega^2}\left(1 - \cos\Omega t\right). \tag{2.4}$$

For $t \geq \epsilon$

$$\frac{d^2y}{dt^2} + \Omega^2 y = 0, \quad y(\epsilon) = \frac{v_0}{\epsilon\Omega^2}\left(1 - \cos\Omega t\right), \quad y'(\epsilon) = \frac{v_0}{\epsilon\Omega}\sin\Omega\epsilon, \tag{2.5}$$

where the initial conditions are obtained from (2.4) evaluated at $t = \epsilon$. The solution to (2.5) is

$$y = -\frac{v_0}{\epsilon\Omega^2}\left(1 - \cos\Omega\epsilon\right)\cos\Omega t + \frac{v_0}{\epsilon\Omega^2}\sin\Omega\epsilon\sin\Omega t \tag{2.6}$$

and in the limit $\epsilon \to 0$:

$$y \sim \frac{v_0}{\Omega}\sin\Omega t. \tag{2.7}$$

Solution by transform methods

Now solve the knocked pendulum problem (2.1) by taking the Fourier transform of the equation

$$\int_{-\infty}^{\infty}\left(\frac{d^2y}{dt^2}\,e^{i\omega t} + \Omega^2 y e^{i\omega t}\right)dt = \int_{-\infty}^{\infty} v_0\delta(t)e^{i\omega t}\,dt. \tag{2.8}$$

Let

$$\tilde{y}(\omega) = \int_{-\infty}^{\infty} y(t)e^{i\omega t}\,dt \tag{2.9}$$

be the Fourier transform of y. We need (2.9) to converge when $y = 0$ and $y' = 0$ for all $t < 0$. If y remains bounded for all $t > 0$, then (2.9) converges when $\omega_i > 0$. Integrate the derivative term twice by parts

$$\begin{aligned}\int_{-\infty}^{\infty} y''e^{i\omega t}\,dt &= \left[y'e^{i\omega t}\right]_{-\infty}^{\infty} - \int_{-\infty}^{\infty} i\omega y'e^{i\omega t}\,dt \\ &= -i\omega\left[ye^{i\omega t}\right]_{-\infty}^{\infty} + \int_{-\infty}^{\infty}(i\omega)^2 ye^{i\omega t}\,dt \\ &= -\omega^2\tilde{y}\end{aligned} \tag{2.10}$$

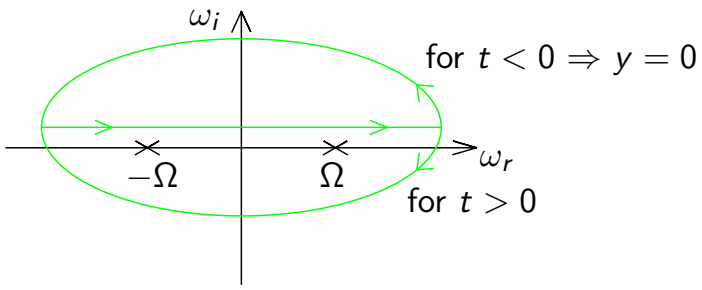

Figure 2.1: Integration contour (green line) in the complex $\omega-$plane. Poles produced by roots of dispersion relation in equation (2.13) are shown, when $\Omega = \pm\omega$. The placement of integration contour above the pole in complex ω-plane ensures causalities (i.e. there is no response to impulsive disturbance for $t < 0$).

using $y, y' = 0$ for $t < 0$, $\omega_i > 0$ and (2.9). Substituting (2.9) and (2.10) into (2.8), and evaluating the integral on the RHS gives

$$-\omega^2\tilde{y} + \Omega^2\tilde{y} = v_0 \quad \Rightarrow \quad \tilde{y} = \frac{v_0}{\Omega^2 - \omega^2}. \tag{2.11}$$

The solution for $y(t)$ is obtained from the inverse Fourier transform of $\tilde{y}(\omega)$

$$y(t) = \frac{1}{2\pi}\int_{-\infty}^{\infty} \tilde{y}(\omega)e^{-i\omega t}\, d\omega \tag{2.12}$$

integrated along a path in the complex ω plane with $\omega_i > 0$. Substituting (2.11) into (2.12) gives

$$y(t) = \frac{1}{2\pi}\int_{-\infty}^{\infty} \frac{v_0 e^{-i\omega t}}{\Omega^2 - \omega^2}\, d\omega = \frac{v_0}{4\pi\Omega}\int_{-\infty}^{\infty}\left(\frac{e^{-i\omega t}}{\omega + \Omega} - \frac{e^{-i\omega t}}{\omega - \Omega}\right) d\omega \tag{2.13}$$

using partial fractions. By closing the integration path as shown in figure 2.1 we can use the residue theorem. The solution for $t > 0$ is

$$y = \frac{v_0}{4\pi\Omega}\left(-2\pi i e^{i\Omega t} + 2\pi i e^{-i\Omega t}\right) = \frac{v_0}{\Omega}\sin\Omega t. \tag{2.14}$$

Summary of the transform method for initial value problem:

- The impulsive disturbance excites an oscillation at the neutral (unforced) frequency.

- There are poles in the complex $\omega-$plane lying at the natural frequencies.
- The principle of causality is respected by placing the integration contour above all the poles in the complex $\omega-$plane.
- The application of this approach to shear layer instabilities involves Fourier transforms and inverse Fourier transforms in both space and time.
- In this spatio-temporal theory both wavenumber and frequency may be complex.

2.1 Absolute instability theory

The criterion for absolute instability is obtained by considering the response of a previously undisturbed flow to an impulsive, spatially localised disturbance. Consider localized unsteady forcing to undisturbed flow

$$\hat{v}(x,0,t) = \delta(x)\hat{f}(t), \tag{2.15}$$

which is switched on at $t = 0$, where $\hat{f} = 0$ for $t < 0$. The response can be expressed in terms of double integral of normal modes over all wavenumbers and frequencies, which is obtained, in the same manner as in the preliminary example (see section 2.0.1), from inverse Fourier transforms as

$$\hat{v}(x,y,t) = \frac{1}{4\pi^2}\int_F\int_A \frac{f(\omega)}{\Delta(\alpha,\omega)} v(y) e^{i(\alpha x-\omega t)} d\alpha d\omega, \tag{2.16}$$

where $\Delta = 0$ is the dispersion relation. Δ appears in the denominator and roots of $\Delta = 0$ give non-trivial solutions when the forcing is switched off. Integration contours F and A run from $-\infty$ to $+\infty$, but not necessarily along the real axes. Roots of the dispersion

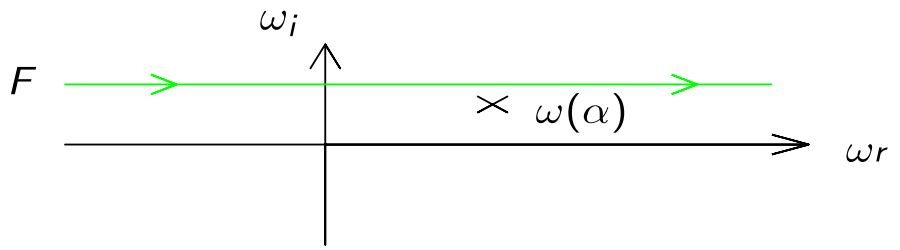

Figure 2.2: Pole $\omega(\alpha)$ produced by root of dispersion relation $\Delta = 0$ in equation (2.16) and placement of integration contour F (green line) above the pole in complex ω-plane, which ensures the causality, so there is no response before the forcing is switched on.

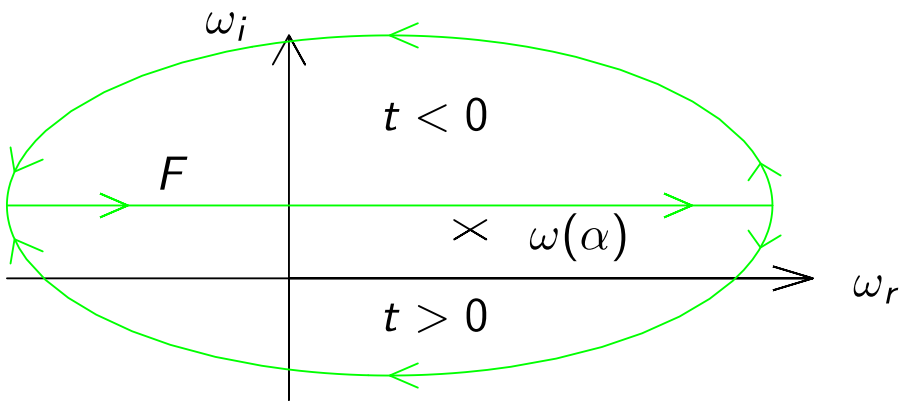

Figure 2.3: Closed integration contour F (green line) in upper or lower half of complex $\omega-$plane depending on time $t < 0$ or $t > 0$.

relation $\Delta = 0$ produce poles in (2.16) as shown for example in figure 2.2. Depending on time $t < 0$ or $t > 0$ we close the contour F either in the upper or lower half-plane as shown in figure 2.3. Placing the F contour above all poles ensures causality, so there is no response before the forcing is switched on. The frequency integral in (2.16) is obtained from residues. Similar considerations apply to the Integration contour A in (2.16). Consider for example results as shown in figure 2.4. In this case the integration contour can be placed on the real α-axis because the disturbance is spatially localised and hence inverse transforms are convergent. With α real and ω complex this is in

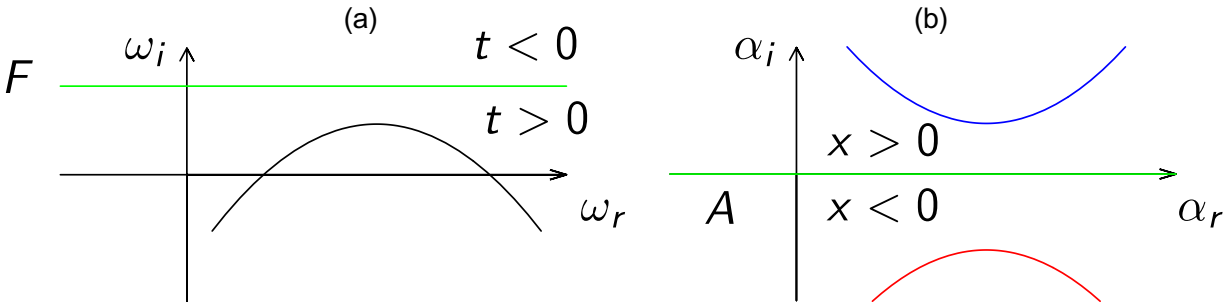

Figure 2.4: Resultant dispersion relation, black line, in complex ω-plane shown in part (a) with the placement of integration contour F (green line). In part (b) is the dispersion relation in the complex α-plane, blue and red lines (which corresponds to downstream and upstream propagating waves), with A contour (green line) placed on real α-axis. The black line in part (a) corresponds to a root of $\Delta = 0$ for the contour A in part (b). The blue and red lines in part (b) corresponds to roots of $\Delta = 0$ for the contour F in part (a).

effect a temporal stability theory. The A contour in 2.4 part (b) can be closed in upper half-plane when $x > 0$, or in lower half-plane when $x < 0$, so that $e^{-\alpha_i x}$ is small in each case. Therefore any poles in the upper half of the α-plane (blue line in figure 2.4(b)) produced by F give downstream propagating waves and any poles in the lower half of the α-plane (red line in figure 2.4(b)) produced by F give upstream propagating waves. Similarly the black line in the ω-plane in the figure 2.4(a) is the locus of poles produced by A. The integration contours F and A are placed in their complex planes in accordance with the principle of causality, as described in figure 2.3. They can then be moved in their complex planes provided they do not cross any singularities. Any movement of the F contour causes the spatial branches (blue and red lines in figure 2.4(b)) to move. Any movement of the A contour causes the temporal branches (black line in figure 2.4(a)) to move. This simultaneous deformation of contours maintains causality provided no singularities are crossed. It may be possible to lower F onto the real axis, as for example shown in figure 2.5(a). If the lowering of the F contour

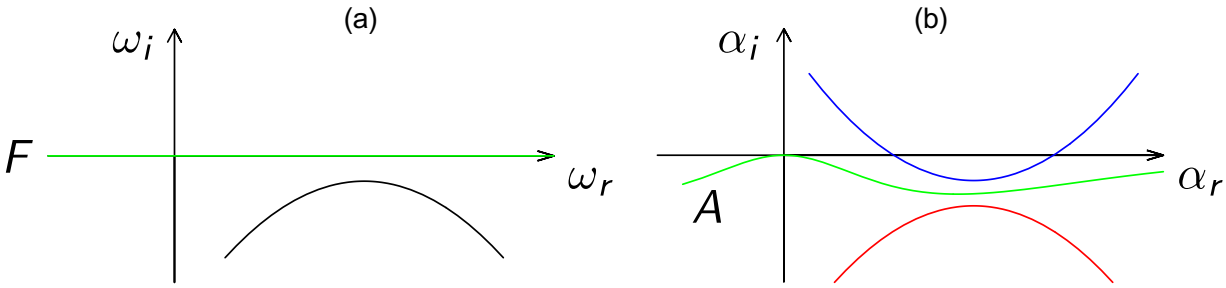

Figure 2.5: Resultant dispersion relation, black line, in complex ω-plane shown in part (a) with the placement of integration contour F (green line). In part (b) is dispersion relation in complex α-plane, blue and red line (which corresponds to downstream and upstream propagating waves), with A contour deformed into the complex α-plane

onto the real axis (as described in figure 2.5(a)) causes a spatial branch of downstream propagating waves to cross the real axis, as shown in figure 2.5(b), then the A contour must be moved below the real axis so that A does not cross any singularities. This corresponds to converting a temporal instability description of disturbances into spatial theory, where ω is real and α is complex. This is called convective instability and the example considered here establishes that there are waves travelling downstream that grow with downstream distance. A spatial branch of upstream travelling waves crossing the real axis would imply unstable upstream travelling waves. Sometimes F can not be lowered to the real ω-axis as considered in the example shown in figure 2.6. The A contour is then said to be pinched by spatial branches as shown in figure 2.6 (d), Im(ω) at the pinch point gives the growth rate in time of the absolute instability. This is Briggs method for finding absolute instability (see Briggs [18] or Healey [37]).

The difference in physical behaviour of convectively unstable flow and absolutely unstable flow can be found from considering the response to an impulsive disturbance. Therefore we consider an impulsive disturbance, $f(\omega) = 1$, and use the residue theorem

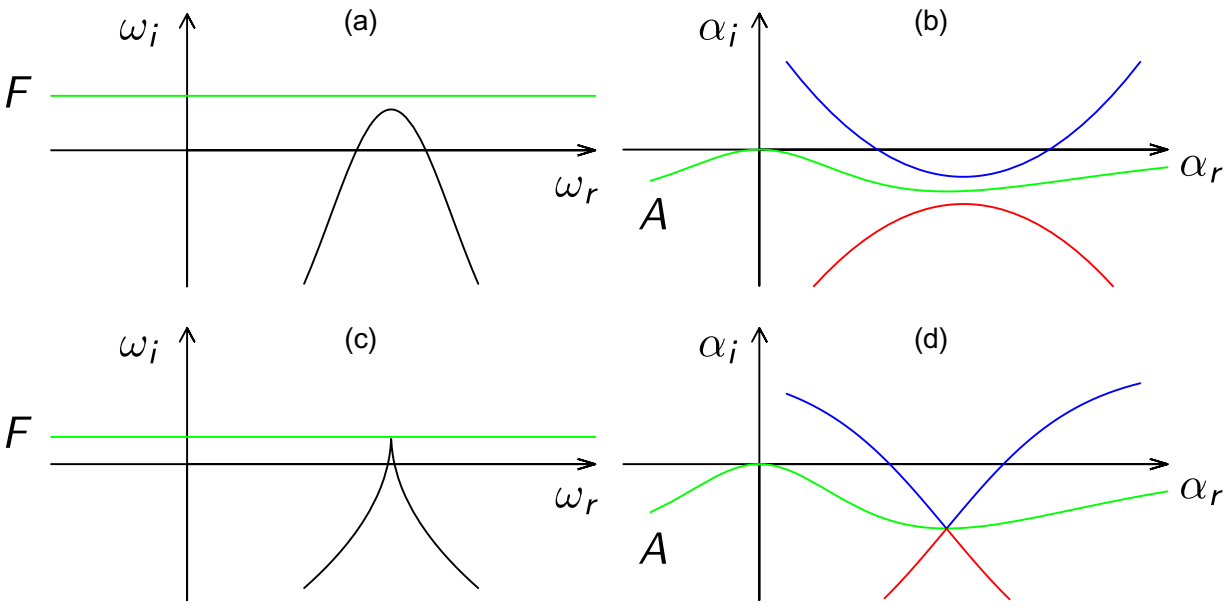

Figure 2.6: Resultant dispersion relation, black line, in complex ω-plane shown in part (a) and (c) with the placement of integration contour F (green line). In part (b) and (d)is the dispersion relation in the complex α-plane, blue and red lines (which corresponds to downstream and upstream propagating waves), and deformation of integration contour A (green line) in the complex $\alpha-$plane.

to evaluate the ω-integral in (2.16) first. This leaves the α-integral in the form

$$\hat{v} = \int_A -\frac{2\pi i}{\Delta_\omega} v(y) e^{i(\alpha x - \omega(\alpha) t)} d\alpha = \int_A -\frac{2\pi i}{\Delta_\omega} v(y) e^{\phi t} d\alpha, \tag{2.17}$$

where

$$\phi(\alpha) = i(\alpha \frac{x}{t} - \omega(\alpha)). \tag{2.18}$$

$\omega(\alpha)$ in (2.18) is a root of $\Delta = 0$ since the roots of $\Delta = 0$ gives poles captured by the residue theorem. This is a superposition of normal modes satisfying the dispersion relation, where the factor Δ_ω represents the receptivity to disturbances of different frequencies. In the limit $t \to \infty$ the integral (2.18) is dominated by the contribution from the saddle-point at which

$$\frac{d\phi}{d\alpha} = 0 \implies \frac{d\omega}{d\alpha} = \frac{x}{t}. \tag{2.19}$$

This is because away from the saddles the integrand in (2.18) is highly oscillatory, leading to substantial cancellation. At the saddle the phase of ϕ is stationary and hence the integrand is non-oscillatory near the saddle. We locate the saddle points of ϕ by plotting contours of constant $\mathrm{Re}(\phi)$ in the complex-α plane, as shown in example figure 2.7. The saddles that contribute to the solution are those that have valleys along the real wavenumber axis. The A integration contour through such a saddle then follows a steepest descent path from the saddle point. The large-t behaviour in different frames of reference is found by choosing different values of x/t in (2.19). In the rest frame the large-t behaviour is given by

$$\frac{x}{t} = 0. \tag{2.20}$$

and hence

$$\frac{\partial \omega}{\partial \alpha} = 0, \tag{2.21}$$

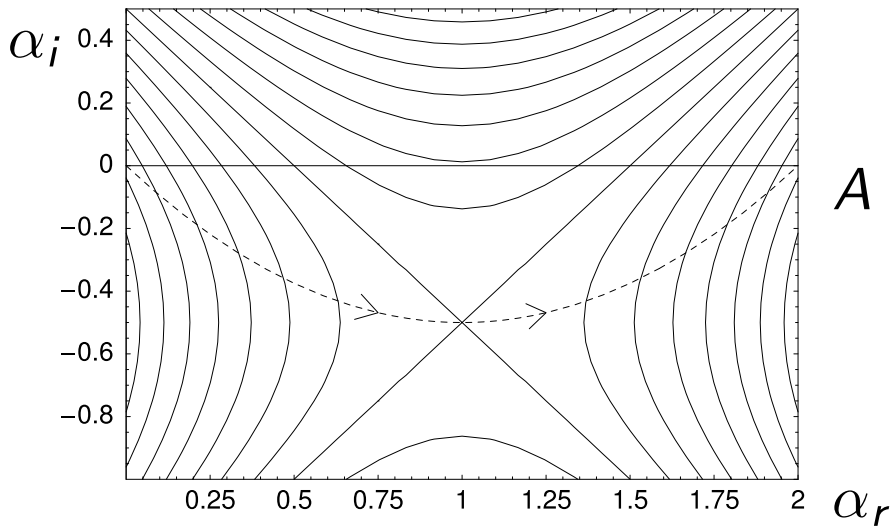

Figure 2.7: Deformation of integration contour A (dashed line), following the steepest decent path, in the complex α-plane passing through the saddle point.

which corresponds to zero group velocity. When $x/t = 0, \phi = -\mathrm{i}\omega$, so contours of $\mathrm{Re}(\phi)$ are equal to contours of $\mathrm{Im}(\omega)$, which corresponds to roots of the dispersion relation $\Delta = 0$ for horizontal F-integration contours, i.e. spatial branches in the complex α-plane. Therefore, locating saddles and steepest-descent valleys corresponds to finding the spatial branches that pinch the integration contours in Brigg's method (see Briggs [18] or Healey [37]).

The condition for absolute instability, i.e. for growth in the rest frame, is therefore

$$\frac{\partial \omega}{\partial \alpha} = 0, \mathrm{Im}(\omega) > 0, \tag{2.22}$$

where α and ω are the wavenumber and angular frequency respectively of a wave satisfying the dispersion relation. This result was first obtained by Briggs (1964) [18] in a plasma physics context, and independently by Gaster (1962) [38] in a hydrodynamic stability problem. Note that in general both α and ω will be complex at the saddle point (2.21), and only the saddles for which the integration contour in the complex

wavenumber plane can be deformed to lie in the valleys of the saddle point are relevant (the 'pinch-point' criterion as described above).

In effect we are extending the temporal stability result, where ω is complex and α is real, into the complex $\alpha-$plane by letting both α and ω be complex. It is therefore useful to have the temporal results prior to absolute instability calculations.

2.2 Temporal stability results

We consider the model problem with velocity profile

$$U(z) = (1 + \tanh(5z))/2 \tag{2.23}$$

and density profile

$$\bar{\rho}(z) = 1 - d\tanh(5z) \tag{2.24}$$

where

$$d = \frac{\rho_b - \rho_u}{\rho_b + \rho_u} \tag{2.25}$$

shown in figure 2.8.

There is not a good reason for including the factor 5 in the velocity and density profiles. It arose because in our early numerical solutions of the Taylor-Goldstein equation we were investigating the effect of different relative thicknesses of the velocity and density profiles and we experimented with range of different numerical coefficients in the profiles. Results relating to different relative thicknesses of velocity and density profiles are presented in chapter 4. When it was discovered that the factor of 5 was still in the profiles it was decided to leave it, as re-doing all the computations would have taken too long. Note that in previous work velocity profiles were often chosen to be $U(z) = (1 + \tanh(z))/2$ (for example in Huerre & Monkewitz 1985 [19]), and hence

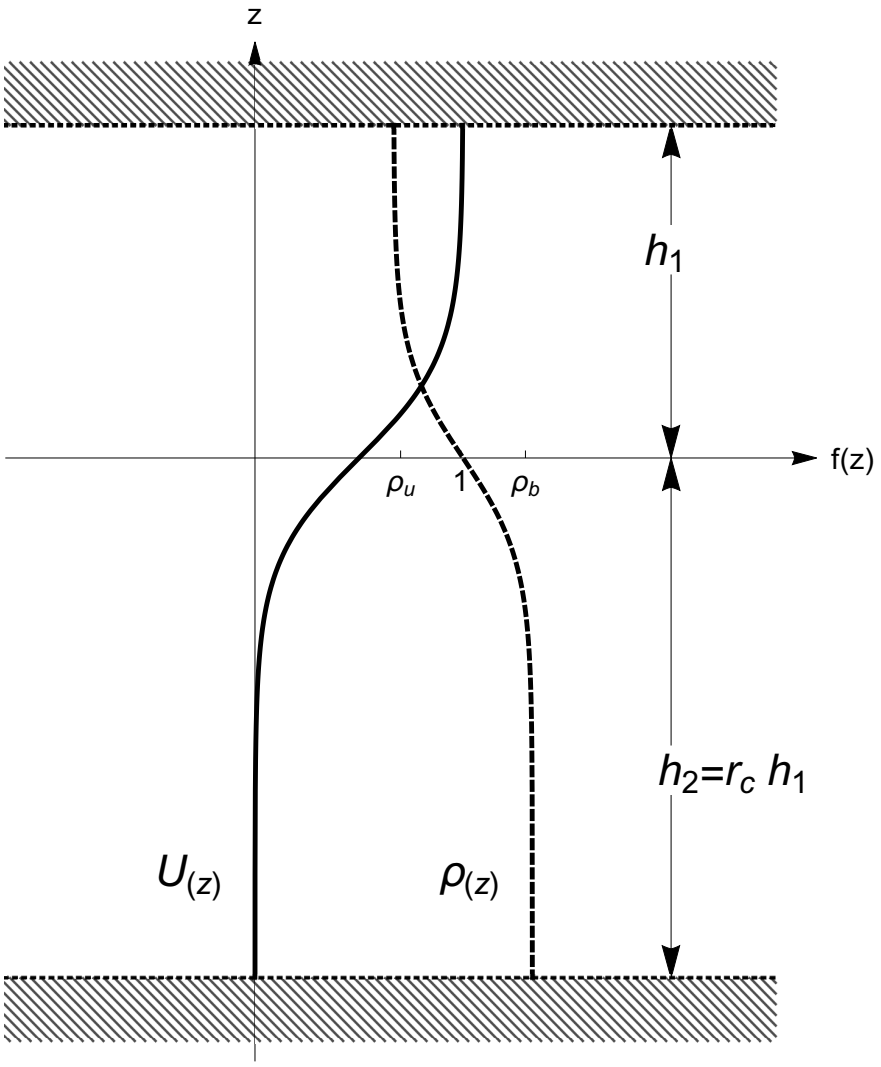

Figure 2.8: Layout of the problem considered for temporal and absolute stability analysis with model velocity profile (2.23) and model density profile (2.24). h_1 and h_2 are the distances of the upper boundary and bottom boundary respectively from the center of the velocity shear. r_c is the parameter used in the description of our models and results and it is the ratio of the upper and bottom boundary.

if our results are to be compared with those of Huerre, a factor of 5 has to be used for the values of wavelength $1/\alpha$ and for the phase speed c.

We seek solutions to Taylor-Goldstein equation (1.18) giving the dispersion relation $c(\alpha)$ or $\omega(\alpha)$. If we let the wave number α be real and allow the phase speed c or frequency ω to be complex, which corresponds to temporal stability analysis, then it follows from normal mode analysis, where the perturbations are in the form $\exp[\mathrm{i}(\alpha \mathrm{x} - \omega \mathrm{t})]$ with $\omega = c\alpha$, that all modes with imaginary part of the phase speed $c_i > 0$ or $\omega_i > 0$ will be growing in time resulting in temporally unstable flow.

In the temporal stability analysis an analytical solutions can be derived with the use of piecewise linear theory as described in chapter 1. Results of piecewise linear theory are used for initial guesses for numerical solution to the Taylor-Goldstein equation (1.17).

2.2.1 Piecewise linear approximation for initial guesses of c or ω for numerical calculations

For initial guesses of c (or ω) for the shooting method used in numerical calculations, it is sufficient to consider homogeneous problem. Consider homogeneous bounded flow with the basic velocity profile for the $U(z)$ defined as follows

$$U(z) = \begin{cases} 1 & : l < z < h_1 \\ z/l & : |z| < l \\ -1 & : -h_2 < z < -l \end{cases} \tag{2.26}$$

Hence there are two jumps at $z = \pm l$, which divides the problem into three layers. Since $U'' = 0$ in each layer, Rayleigh's equation (1.22) simplifies into

$$\phi'' - \alpha^2 \phi = 0 \tag{2.27}$$

Using $U(z)$, (2.27) is solved in each layer as

$$\phi(z) = \begin{cases} A\sinh\alpha(h_1 - z) & : l < z < h_1 \\ B\sinh\alpha z + C\cosh\alpha z & : |z| < l \\ D\sinh\alpha(h_2 + z) & : -h_2 < z < -l, \end{cases} \tag{2.28}$$

and applying matching conditions (1.29) and (1.32) at $z = -l$ and $z = l$ yields to dispersion relation

$$\frac{c(\alpha l + XY_1\alpha l) + (Y_1 - \alpha l - XY_1\alpha l)}{c(-Y_1\alpha l - X\alpha l) + (Y_1\alpha l + X\alpha l - XY_1)} + \frac{c(-\alpha l - XY_2\alpha l) + (Y_2 - \alpha l - XY_2\alpha l)}{-c(-Y_2\alpha l - X\alpha l) + (Y_2\alpha l + X\alpha l - XY_2)} = 0 \tag{2.29}$$

where $Y_1 = \tanh(\alpha(h_1 - l))$, $Y_2 = \tanh(\alpha(h_2 - l))$ and $X = \tanh(\alpha l)$. See appendix B for derivation of (2.29).

2.2.2 Numerical solutions for temporal instability

The Taylor-Goldstein equation (1.17) is solved numerically and a shooting method is used to find eigenvalues. Homogeneous boundary conditions, $w = 0$, are applied at the boundaries placed at $z = z_1, z_2$, or $w \to 0$ as $z \to \pm\infty$ in the unconfined case. We fix the parameters and guess an initial value of the normal mode phase speed c for a given value of the wave number α, and apply the boundary condition at one of the boundaries, then integrate the equation to the other boundary. Unless the initial guess happens to be exactly on the eigenvalue, the second boundary condition will not be satisfied, and an iterative procedure is used to successively modify the value of the eigenvalue until the boundary conditions are satisfied to within some tolerance. Newton iteration is used with a pair of c-values close to each other to get the first correction and than the result of previous integration is used to get the next correction. This process is then repeated to the desired accuracy with relative tolerance $\Delta\omega/\omega = 10^{-4}$,

which in our case is for the frequency $\Delta\omega \approx 10^{-6}$. Note that the initial guesses for the pair of c-values close to each other can be obtained from piecewise linear analysis. This process is then repeated for $\alpha + \Delta\alpha$, where we fix $\Delta\alpha = 1/1000$. These numerical calculations result in a table of frequencies ω on a grid of points of α for which the interpolation function (see Mathematica [9]) is used to get smooth $\omega(\alpha)$ curves for presenting on graphs.

There is a potential difficulty solving the Taylor-Goldstein equation (1.17) due to the singularity where $U(z) = c$, called the critical point. We must take the integration below this singularity in the complex plane. However the integration path can be taken along the real axis when the waves are unstable with $c_i > 0$ and hence $\mathrm{Im}(z_c) > 0$ when $\mathrm{Re}(U'(z_c)) > 0$. For convenience, we only calculate unstable waves. Taking the path below z_c is called Lin's rule, who derived it using asymptotic theories for large Reynolds number, and which he used to show that the inviscid solution obtained using this path corresponds to viscous solutions as the viscosity tends to zero (see Lin 1955 [39]). Since we are integrating along the real $z-$axis we can only do so for $c_i > 0$ and hence the range of numerical solution (or range of the real wavenumbers) is given by this condition. The coding algorithm in Mathematica, and use of NDSolve, for calculating temporal stability results is shown in appendix C.

An example of temporal stability results is shown in figure 2.9, which was obtained for $\bar{\rho} = \text{const.}, \mathrm{U(z)}$ given by $(2.23), h_1 = 5, r_c = 2.5$. NDSolve is Mathematica's built-in function for numerical solution of ordinary differential equations, and the result of the above example have been verified against Matlab code (Matlab [10]), which gives exactly same result as presented in figure 2.9. In addition we also compare the above temporal stability result with piecewise linear result (see appendix C) as providing another independent verification of our numerical result. Note that the maximum

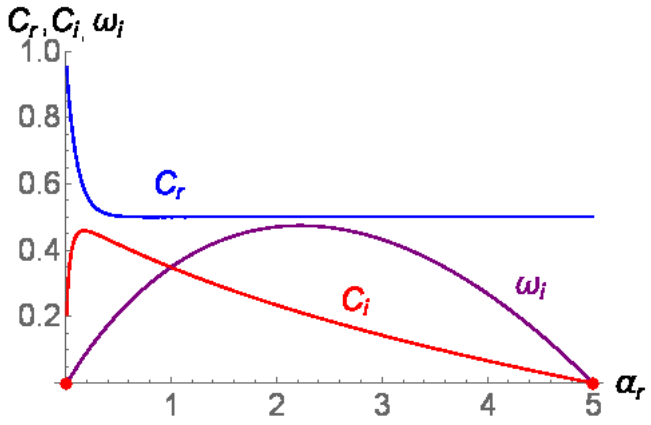

Figure 2.9: Example of temporal stability result with the use of numerical solution. Dispersion relation ω_i (purple line), c_i (red line), and c_r (blue line) as a function of wave number α with fixed parameters $\bar{\rho} = const., U(z)$ given by (2.23), $h_1 = 5$, and $r_c = 2.5$

$\omega_i = 0.47$ is for $\alpha_r = 2.22$ with $c_i = 0.21$ and $c_r = 0.5$. This means that the most unstable mode has wavelength $2\pi/\alpha = 2.83$ and phase speed $c_r = 0.5$ which would be expected to dominate the growing perturbations in time. The range of temporally unstable wave numbers for this particular parameter combination is bounded by neutral points denoted in figure 2.9 by red dots at $\alpha = 0$ and $\alpha = 5$. This can be repeated for a wide range of parameters and results can be represented as neutral curves which are interpolations of the neutral points. The results of temporal stability analysis are used in absolute stability analysis which from a methodological point of view is the extension of the temporal results into the complex α plane. Temporal results tell us about growing perturbations in time but we don't know if they will grow or decay upstream or downstream of the disturbance source. For this purpose an absolute stability analysis is needed for which both α and ω can become complex.

2.3 Absolute instability of unconfined flow

In the original problems concerned with mixing layers people usually ignored the boundaries where possible and found that for absolute instability reverse flow is necessary as described by Huerre & Monkewitz 1985 [19]. A flow which has two layers of fluid moving in opposite directions is called counter-flow and a flow which has two layers of fluid moving in same direction (or where one of the layers is stationary) is called co-flow. Two layer flows where one of the layers is stationary often arise in oceanography.

In this section we first illustrate the important qualitative changes to absolute instability analysis produced by introducing boundaries to the flow. We then include the effects of stable stratification, since they are often important in geophysical flows. Results for unbounded homogeneous counter-flow and co-flow are shown in figures 2.10 and figure 2.11. The dominant saddle is denoted by the black dot and the red lines are the neutral curves where $\omega_i = 0$. This unbounded homogeneous counterflow is absolutely unstable with $\omega_i > 0$ at the dominant saddle and the unbounded homogeneous co-flow is only convectively unstable since $\omega_i < 0$ at the dominant saddle. The amount of counterflow needed for homogeneous unbounded flow to become absolutely unstable depends on the velocity profile, and the tanh profile was studied in Huerre & Monkewitz 1985 [19]. We also focus on tanh profiles and for the case of counter-flow we consider

$$U(z) = \tanh(5z)/2, \tag{2.30}$$

and for the co-flow we use (2.23).

The neutral curves in figures 2.10 and 2.11 intersect the real α-axis at the points where the growth rate is zero in figure 2.9 and the neutral curves in figures 2.10 and 2.11 are the continuation of those points from figure 2.9 into the complex α-plane.

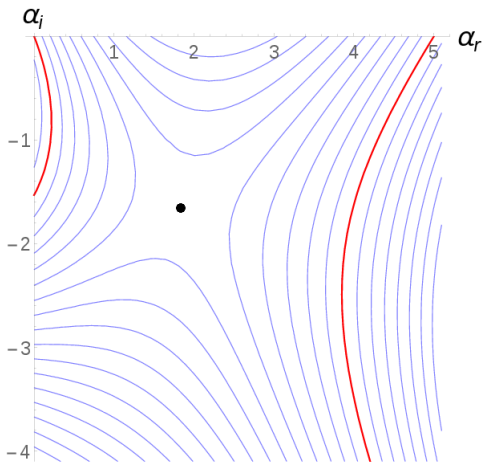

Figure 2.10: Absolute stability result. Contours of constant $\mathrm{Im}(\omega)$ (blue lines) in the complex $\alpha-$plane for the counter-flow with parameters given by (2.30). The contours of $\mathrm{Im}(\omega) = 0$ (red lines) are the neutral contours, and the dominant saddle (black dot) with $\mathrm{Im}(\omega) > 0$ resulting in absolutely unstable flow.

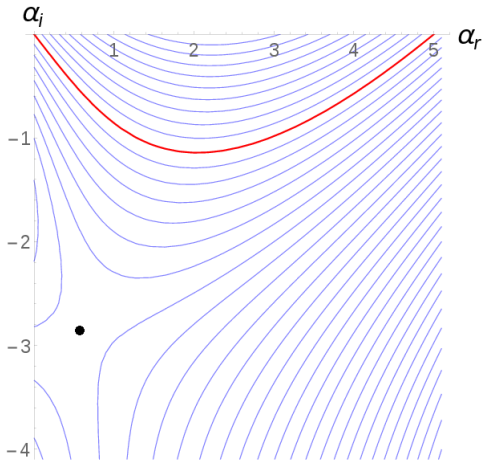

Figure 2.11: Absolute stability result. Contours of constant $\mathrm{Im}(\omega)$ (blue lines) in the complex $\alpha-$plane for the co-flow with parameters given by (2.23). The contours of $\mathrm{Im}(\omega) = 0$ (red lines) are the neutral contours, and the dominant saddle (black dot) with $\mathrm{Im}(\omega) < 0$ resulting in absolutely stable flow.

Healey 2009 [22] showed that suitably placed boundaries will produce absolute instability for mixing layers even without reverse flow. Adding the top boundary at $h_1 = 5$ and the bottom boundary at $h_2 = r_c\ h_1$, with $r_c = 2.5$ results in absolutely unstable flow. These parameters are an example of confinement producing absolute instability.

Adding boundaries to the problem results in poles (see Healey 2009 [22]) along the imaginary α_i axis where $c \to \infty$, and associated with each pole are new saddles, one of which which may be the dominant saddle for the problem. The appearance of saddles is due to the fact that the boundary conditions $w = 0$ at the boundaries placed at $z = z_1, z_2$ in (1.17) results in non-trivial solutions for purely complex wave numbers with zero real part.

2.3.1 Numerical solutions for absolute instability

From the methodological point of view, as already mentioned in chapter 1, the absolute instability results are essentially an extension of temporal instability results into the complex $\alpha-$plane. In the case of unbounded problems this is numerically not difficult as variation of complex ω in the complex $\alpha-$plane is not extremely fast and hence the use of previous results of complex ω at given wavenumber α is sufficient everywhere for the shooting method required to obtain the next result for $\alpha + \Delta\alpha$. The steps between the last solution and the next solution $\Delta\alpha$ has to be sufficiently small for the code to converge. This process is continued over a rectangular grid in the complex $\alpha-$plane, storing the eigenvalue for ω for each complex value of α. The grid spacing was $1/1000$ parallel to both the real axis and the imaginary axis.

In the case of bounded problems the numerics gets more complicated since, as mentioned in the previous section, there are infinitely many poles along the imaginary

$\alpha-$axis and hence infinitely many solutions for ω, and hence close to the poles along the imaginary $\alpha-$axis the variation of ω does becomes enormous and is very difficult to follow the solution even with extremely small steps in $\Delta\alpha$. Often our codes diverges or converges to a different Riemann surface as we approach the poles along the imaginary $\alpha-$axis and this difficulty gets greater the further we are from the origin along the imaginary $\alpha-$axis. Nevertheless the numerical solutions close to the saddles created by those poles and further away from the imaginary $\alpha-$axis are well behaved and the variation of ω is possible to follow with steps in the wavenumber $\Delta\alpha = 1/1000$. In the results we present for absolute stability we include the regions where these difficulties described above happen because although there are errors due to missing data or data from different Remain surface close to the imaginary $\alpha-$axis, we are capturing and showing the appearance of as many saddles as possible. Hence in the results presented for $\omega = \omega(\alpha)$ we focus at the values around the saddles. These numerical calculations result in a table of frequencies ω on a grid of points in the complex wavenumber plane for which interpolation functions are used to get smooth surfaces of results in the complex $\alpha-$plane. In cases where there are no data in parts of the grid, extrapolation is used which is embedded in the interpolating software of Mathematica [9]. The coding algorithm in Mathematica for calculating absolute stability results is shown in appendix C.

2.4 Absolute instability of confined flows

In our problem the boundaries are not symmetrical and location of the poles will not be analytically analysed. One boundary placed for homogeneous co-flow will however not result in absolutely unstable flow and a second suitably placed boundary is necessary

(see Healey 2009 [22]).

The result of adding one upper boundary at various values of h_1 to homogeneous flow and second boundary placed at $h_2 = 2.5h_1$ is shown in figures 2.12,2.13,2.14,2.15 and 2.16 which can also be compared with the unbounded homogeneous case shown in figure 2.11. These figures clearly show the appearance of new saddles due to the addition of one or two boundaries. These figures also show that the appearance of absolute instability is possible only with two boundaries with the second boundary placed within a certain range of distances, and $h_2 = 2.5h_1$ lies in this range (see Healey 2009 [22]). Note that the disc in figure 2.12 at $\omega_i = -0.3186$ is the saddle in the unconfined problem, and at this large h_1 is distinct from the confinement saddles that appear near the imaginary axis. As h_1 is reduced this saddle gets caught up in amongst the confinement saddles. From these results we can see how confinement modifies the complex α-plane and an important point to make is that there is a neighbourhood of the imaginary α-axis that is always modified by the confinement, which can lead to a qualitative difference to the absolute instability compared with the unconfined case even when h_1 is very large as seen in figure 2.12, where $h_1 = 10$. In fact we observe that the saddles approach the imaginary α-axis as h_1 increases and move further out into the complex α-plane as h_1 decreases, which is the mechanism by which one of the saddles becomes the dominant saddle. The parameter regime of model problems considered for this chapter is given in the table 2.1, which summarize the confinement effects discussed above.

In all examples shown in figures 2.12,2.13,2.14,2.15 and 2.16, the closest saddle to the origin is now the dominant saddle of the system with $\omega_i < 0$ in those with upper boundary only (part (a) in the figures), and hence absolutely stable, and with $\omega_i > 0$ at the closest saddle to the origin in those with two boundaries (part (b) in the figure)

Parameters h_1 and r_c	Dominant mode of the problem	
	Frequency	Wavenumber
Case i)a) $h_1 = 10$ $r_c = \infty$	$\omega = 0.0879 - \text{i } 0.0059$	$\alpha = 0.0400 - \text{i } 0.1120$
Case i)b) $h_1 = 10$ $r_c = 2.5$	$\omega = 0.0910 + \text{i } 0.0011$	$\alpha = 0.0570 - \text{i } 0.1010$
Case ii)a) $h_1 = 5$ $r_c = \infty$	$\omega = 0.1734 - \text{i } 0.0092$	$\alpha = 0.0850 - \text{i } 0.2240$
Case ii)b) $h_1 = 5$ $r_c = 2.5$	$\omega = 0.1770 + \text{i } 0.0038$	$\alpha = 0.1170 - \text{i } 0.2020$
Case iii)a) $h_1 = 3$ $r_c = \infty$	$\omega = 0.2795 - \text{i } 0.0104$	$\alpha = 0.1503 - \text{i } 0.3743$
Case iii)b) $h_1 = 3$ $r_c = 2.5$	$\omega = 0.2848 + \text{i } 0.0090$	$\alpha = 0.2023 - \text{i } 0.3356$
Case iv)a) $h_1 = 2$ $r_c = \infty$	$\omega = 0.4025 - \text{i } 0.0084$	$\alpha = 0.2432 - \text{i } 0.5608$
Case iv)b) $h_1 = 2$ $r_c = 2.5$	$\omega = 0.4098 + \text{i } 0.0165$	$\alpha = 0.3159 - \text{i } 0.5033$
Case v)a) $h_1 = 1$ $r_c = \infty$	$\omega = 0.7001 - \text{i } 0.0030$	$\alpha = 0.5855 - \text{i } 1.0752$
Case v)b) $h_1 = 1$ $r_c = 2.5$	$\omega = 0.7137 + \text{i } 0.0275$	$\alpha = 0.7120 - \text{i } 0.9650$

Table 2.1: Parameter regimes of model problems (as shown in figure 2.8) considered for absolute stability analysis. Velocity and density profiles are given by (2.23) and (2.24) respectively. The variation is given by considering different distance of upper boundary h_1 and distance of lower boundary given by parameter r_c, where $h_2 = r_c h_1$. Problems without bottom boundary are considered for each value of h_1 to demonstrate the effect of adding only one boundary to the problem, which remains absolutely stable.

(a)

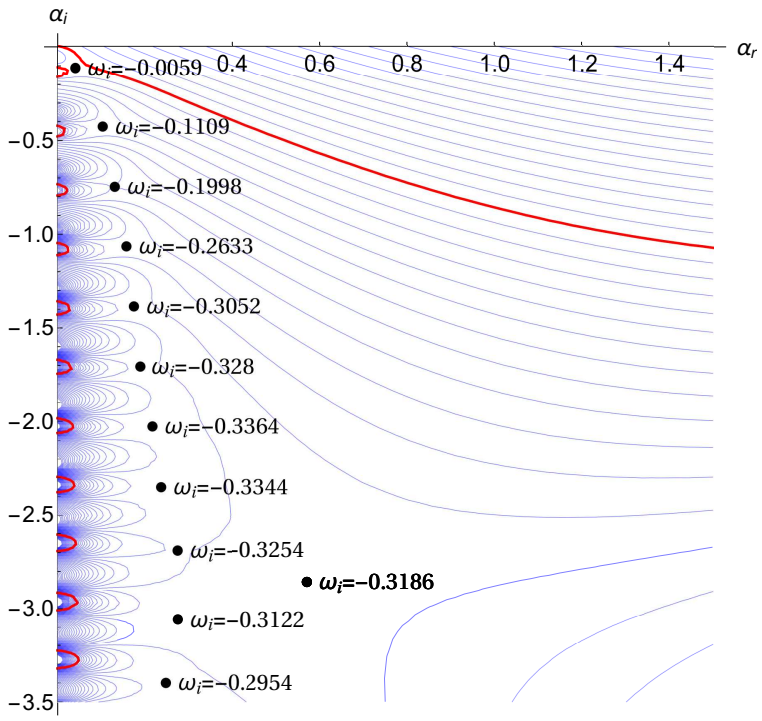

(b)

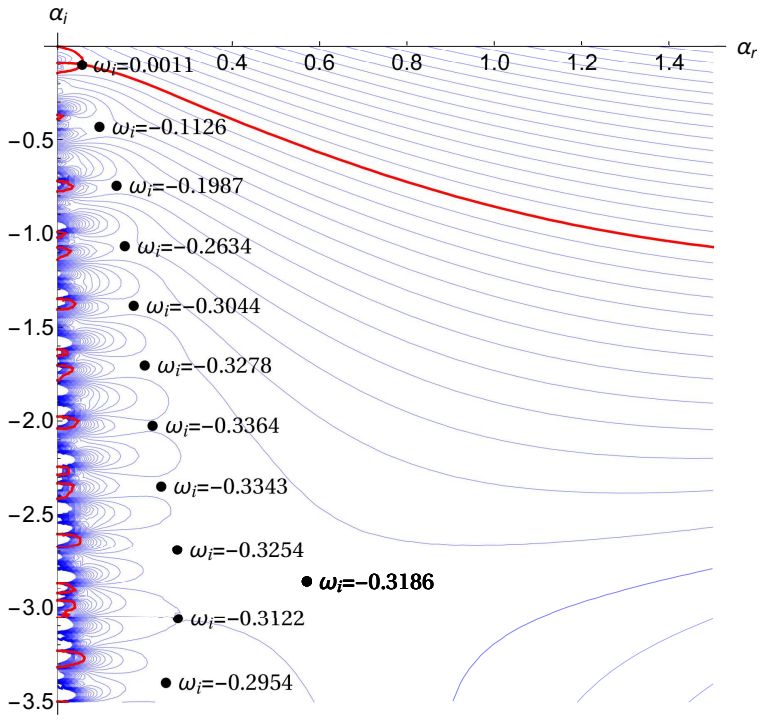

Figure 2.12: Absolute stability analysis results, case i) in table 2.1. Contours of constant $\mathrm{Im}(\omega)$ (blue lines) in the complex α plane for solutions to (1.17). Saddles, where $\frac{\partial \omega}{\partial \alpha} = 0$, are marked as black discs with the dominant saddle being the one closest to the origin. The contours $\mathrm{Im}(\omega) = 0$ are indicated with a red line. (a) with upper boundary only at $h_1 = 10$. (b) with upper boundary at $h_1 = 10$ and bottom boundary at $h_2 = 2.5h_1$.

(a)

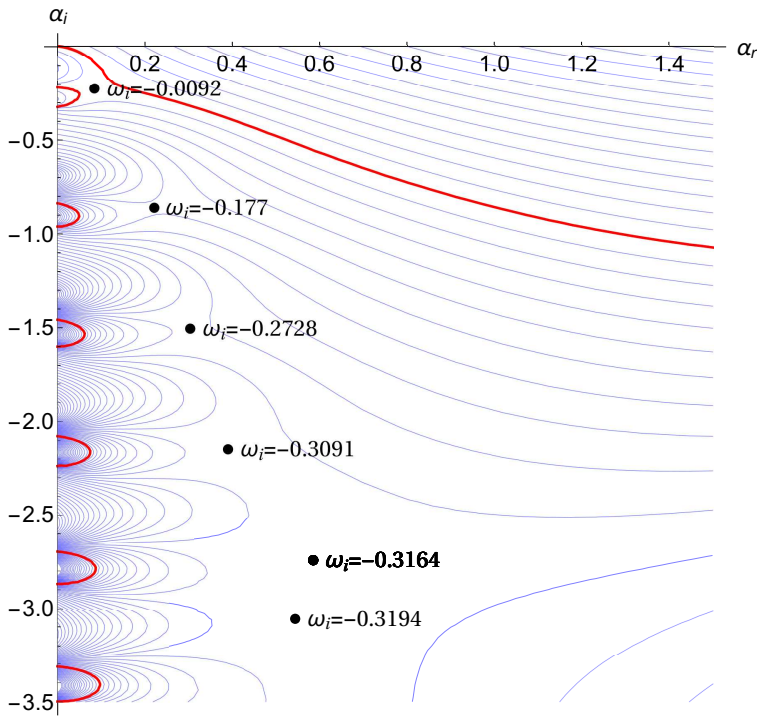

(b)

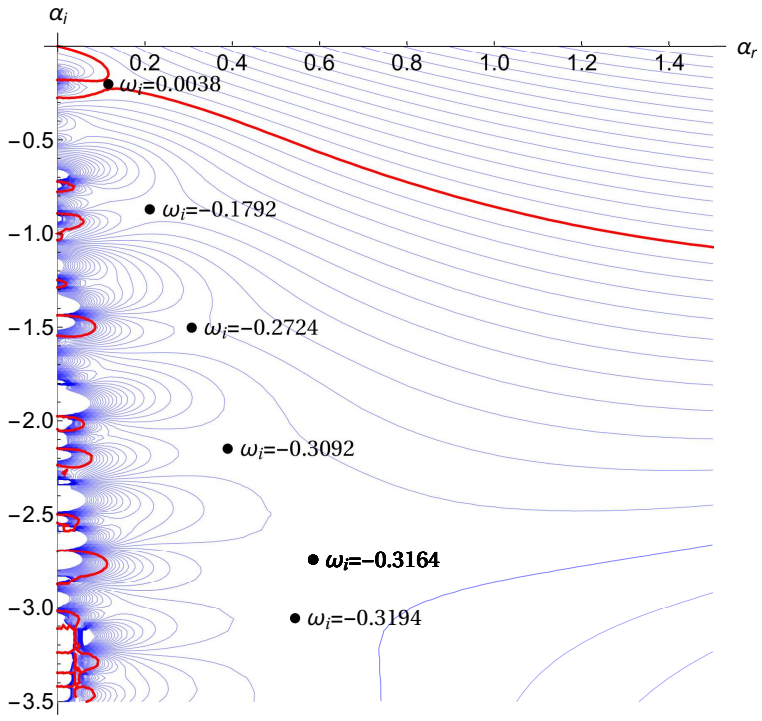

Figure 2.13: Absolute stability analysis results, case ii) in table 2.1. Contours of constant $\mathrm{Im}(\omega)$ (blue lines) in the complex α plane for solutions to (1.17). Saddles, where $\frac{\partial \omega}{\partial \alpha} = 0$, are marked as black discs with the dominant saddle being the one closest to the origin. The contours $\mathrm{Im}(\omega) = 0$ are indicated with a red line. (a) with upper boundary only at $h_1 = 5$. (b) with upper boundary at $h_1 = 5$ and bottom boundary at $h_2 = 2.5h_1$.

(a)

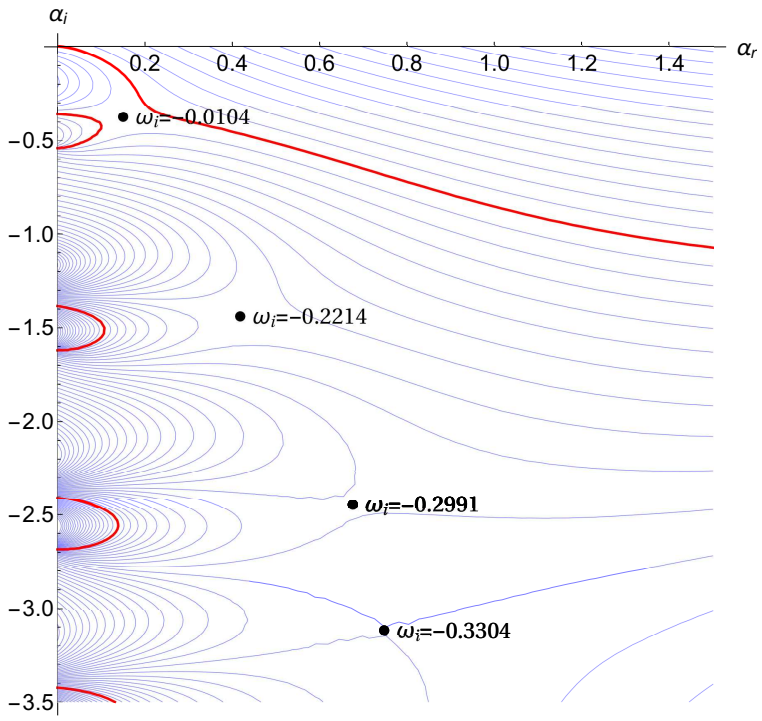

(b)

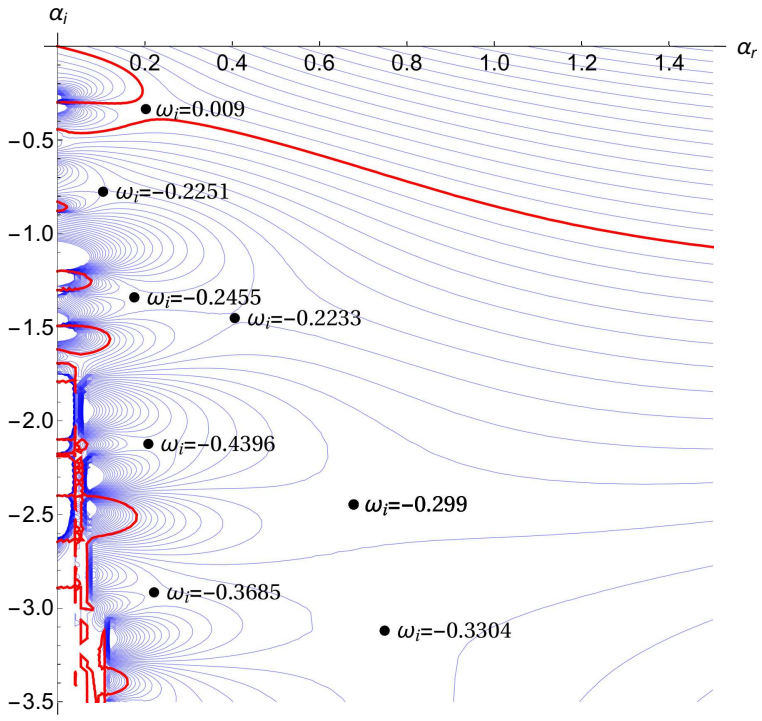

Figure 2.14: Absolute stability analysis results, case iii) in table 2.1. Contours of constant $\mathrm{Im}(\omega)$ (blue lines) in the complex α plane for solutions to (1.17). Saddles, where $\frac{\partial \omega}{\partial \alpha} = 0$, are marked as black discs with dominant saddle being the one closest to the origin. The contours $\mathrm{Im}(\omega) = 0$ are indicated with a red line. (a) with upper boundary only at $h_1 = 3$. (b) with upper boundary at $h_1 = 3$ and bottom boundary at $h_2 = 2.5h_1$.

(a)

(b)

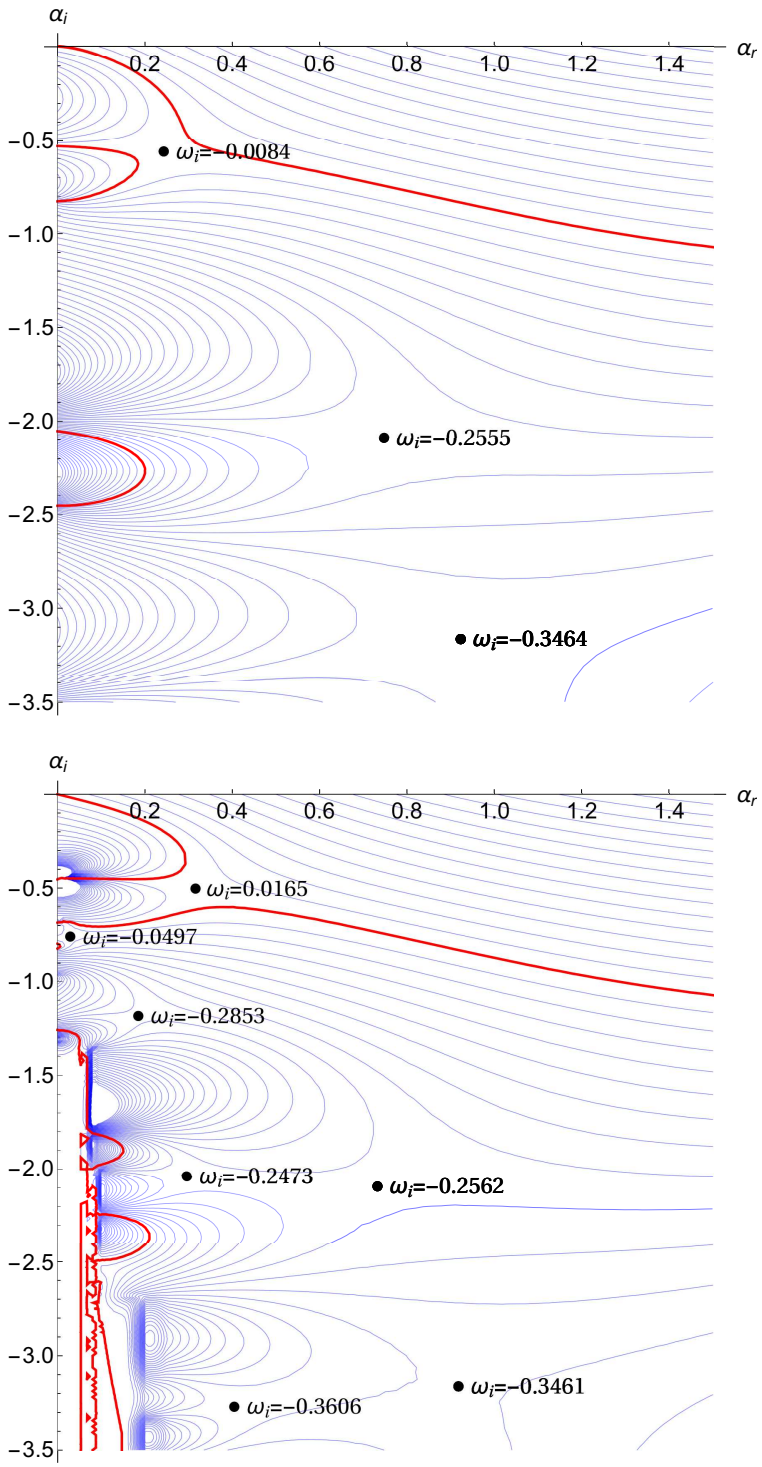

Figure 2.15: Absolute stability analysis results, case iv) in table 2.1. Contours of constant $\mathrm{Im}(\omega)$ (blue lines) in the complex α plane for solutions to (1.17). Saddles, where $\frac{\partial \omega}{\partial \alpha} = 0$, are marked as black discs with dominant saddle being the one closest to the origin. The contours $\mathrm{Im}(\omega) = 0$ are indicated with a red line. (a) with upper boundary only at $h_1 = 2$. (b) with upper boundary at $h_1 = 2$ and bottom boundary at $h_2 = 2.5h_1$.

(a)

(b)

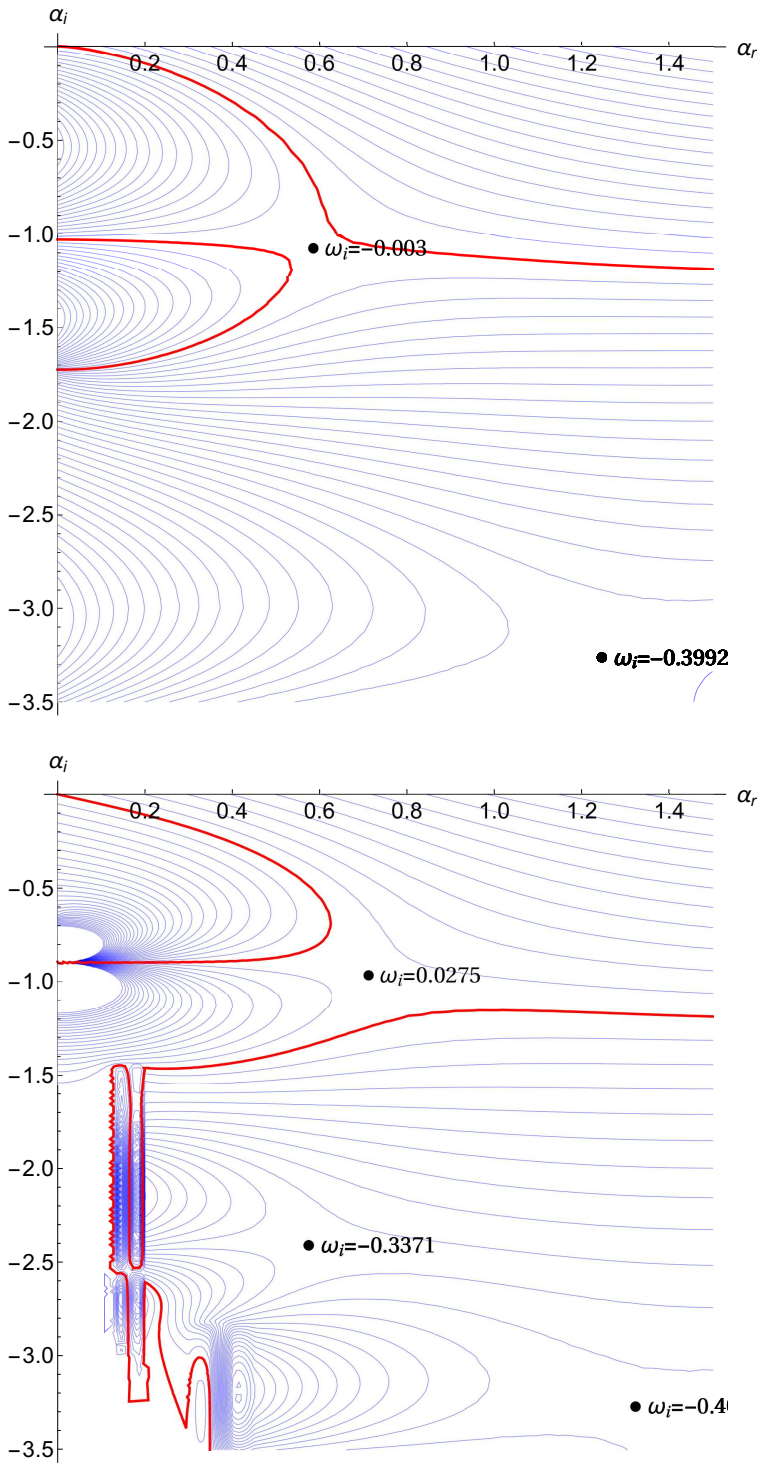

Figure 2.16: Absolute stability analysis results, case v) in table 2.1. Contours of constant $\mathrm{Im}(\omega)$ (blue lines) in the complex α plane for solutions to (1.17). Saddles, where $\frac{\partial\omega}{\partial\alpha} = 0$, are marked as black discs with dominant saddle being the one closest to the origin. The contours $\mathrm{Im}(\omega) = 0$ are indicated with a red line. (a) with upper boundary only at $h_1 = 1$. (b) with upper boundary at $h_1 = 1$ and bottom boundary at $h_2 = 2.5h_1$.

when the second boundary is at $h_2 = 2.5h_1$. The thick red lines represent neutral curves where $\omega_i = 0$ and the intersection of the neutral curve with the α_r axis leads to neutral points from temporal stability analysis as described in figure 2.9.

We now investigate the parameter space for upper boundary h_1 and value of the coefficient r_c where $h_2 = r_c h_1$ is the location of the bottom boundary to find where absolute instability is present. Results for the homogeneous case are shown in figure 2.17 which has maximum $\omega_i \approx 0.025$ with boundaries placed at $h_1 \approx 1, r_c \approx 2.5$. A second local maximum is found with $\omega_i \approx 0.005$ with boundaries placed at particular position $h_1 \approx 6, r_c \approx 2.5$. The thick line represents the neutral curve where $\omega_i = 0$ and inside which the flow is absolutely unstable. Note that the parameter space for the boundaries h_1 and $h_2 = r_c h_1$ considered in the absolute stability analysis for smooth tanh profiles was such that the results captured the absolutely unstable region for maximum of $h_1 = 10$ after which the growth rates are at least ten times smaller than for $h_1 = 6$ (as seen from later results). Since there is no absolute instability for $h_1 < 0.75$ the range of h_1 for which the absolute stability analysis was considered is $0.75 < h_1 < 10$. The parameter range for the bottom boundary was $1.7 < r_c < 4.1$ which captured all absolutely unstable regions for variations of the h_1 considered.

2.5 Stably stratified flows

Stable stratification is present in many oceanic flows, and we study the effect of stable stratification on the absolute instability of confined mixing layers. Define a global Richardson number $J_0 = dgL_0/U_0^2$, where d is defined by (2.25) and density profile (2.24). For fixed $J_0 = 0.01$ the result is shown in figure 2.18. The position of the maximum ω_i remains approximately the same as for the homogeneous problem but the

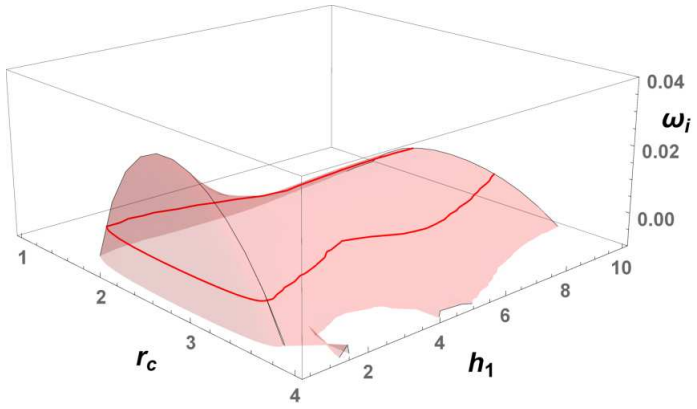

Figure 2.17: Absolute stability analysis results. Surface of $\mathrm{Im}(\omega)$ in parameter space of upper boundary h_1 and coefficient r_c for bottom boundary h_2, with $h_2 = r_c h_1$. The thick red line represents $\mathrm{Im}(\omega) = 0$ (neutral curve) and above which the flow is absolutely unstable.

value of ω_i is now smaller. The thick line again represents the neutral curve where $\omega_i = 0$ and inside this curve the flow is absolutely unstable. We vary the parameter J_0 and combine the resultant neutral curves from each investigation to obtain the neutral surface which maps out the parameter space for the positions of the two boundaries h_1, r_c and density stratification under which stratified co-flow is absolutely unstable. The result is shown in figure 2.19 with maximum for $J_0 \approx 0.025$, which supports absolute instability, with boundaries placed at $h_1 \approx 1, r_c \approx 2.5$.

2.6 Conclusions

In this chapter we revised the methodology for calculating absolute instability using Briggs' saddle point method (see Briggs 1964 [18]) and applied it to stratified co-flows typical in geophysical fluid dynamics. Following the work of Healey 2009 [22], where it was shown that boundaries added to an unbounded parallel flow can have (under

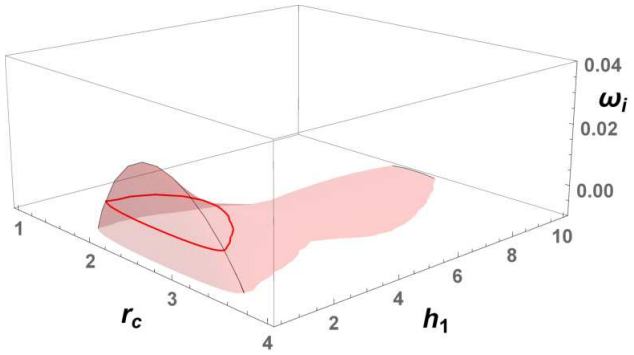

Figure 2.18: Absolute stability analysis results. Surface of $\mathrm{Im}(\omega)$ in parameter space of upper boundary h_1 and coefficient r_c for bottom boundary h_2, with $h_2 = r_c h_1$ with $J_0 = 0.01$. The thick red line represents $\mathrm{Im}(\omega) = 0$ (neutral curve) and above which the flow is absolutely unstable.

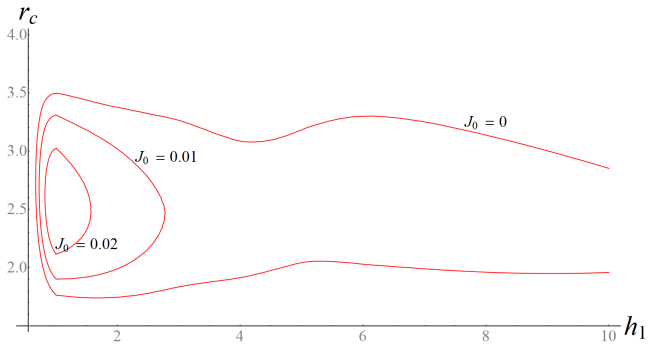

Figure 2.19: Absolute stability analysis results. Contours of neutral surface where $\mathrm{Im}(\omega) = 0$ in parameter space of upper boundary h_1, coefficient r_c for bottom boundary h_2, with $h_2 = r_c h_1$, with various values of J_0.

certain parameter regime) destabilizing effect, we use the rigid lid boundary approximation for the ocean surface. Note that in previous research on instabilities in mixing layers, the boundaries were usually neglected and the flow treated as unbounded. However, Healey 2009 [22] showed how boundaries can create absolute instability, and here we have extended this analysis to include the effects of stable stratification. Hence, we derive the parameter space for which the bounded co-flow with stable stratification is absolutely unstable. Under typical Mediterranean summer conditions the global Richardson number in the upper ocean is usually less than $J_0 = 0.025$ (see Shrira 2015 [5]). Hence in regions parallel to the shore, where the offshore (or inshore) wind creates a layer of fluid moving above essentially stationary fluid, sea bed topographies may result in regions where absolute instability is present. Nevertheless absolute instability analysis is a local analysis and we want to investigate the effect of non-parallel boundaries with the use of global instability analysis, which motivates the next chapter.

3 Global stability analysis

From the results of chapter 2 we see that under certain parameters absolute instability is present in confined co-flow. This means that there is the possibility of absolute instability in the near shore sea region where the offshore or inshore wind will generate the required co-flow velocity profile, the temperature difference or salinity may produce stratification, and the sea surface and sea bed provide the necessary boundaries. Mixed regions are observed in near shore sea and absolute instability has the potential to be the mechanism producing the mixing.

The topography of the sea bed may result in a region of finite streamwise extend where absolute instability is present as shown in figure 3.1, creating a zone of absolute instability parallel to the shore. The region of absolute instability could produce a global instability of the spatially varying flow, but this is only a necessary condition, not a sufficient condition for global instability. Examples will be presented here where there is an absolute instability, but the flow remains globally stable, and also examples where absolute instability does produce global instability. If the flow is globally unstable, than arbitrarily small disturbances grow in the region of interest and eventually the basic flow is strongly modified. Mixing is greatly enhanced by the presence of global instability. The existence of a global instability depends sensitively on both the nature of the streamwise dependence of the basic flow, and on the propagation properties predicted by local dispersion relation ('local' meaning applying at particular location). The absolute instability calculations presented in chapter 2 for parallel flows can be interpreted here as examples of local profiles when the depth of the sea bed varies slowly in the streamwise direction. The approach in the present chapter is to investigate how the absolute instability properties vary in the streamwise direction for models for the

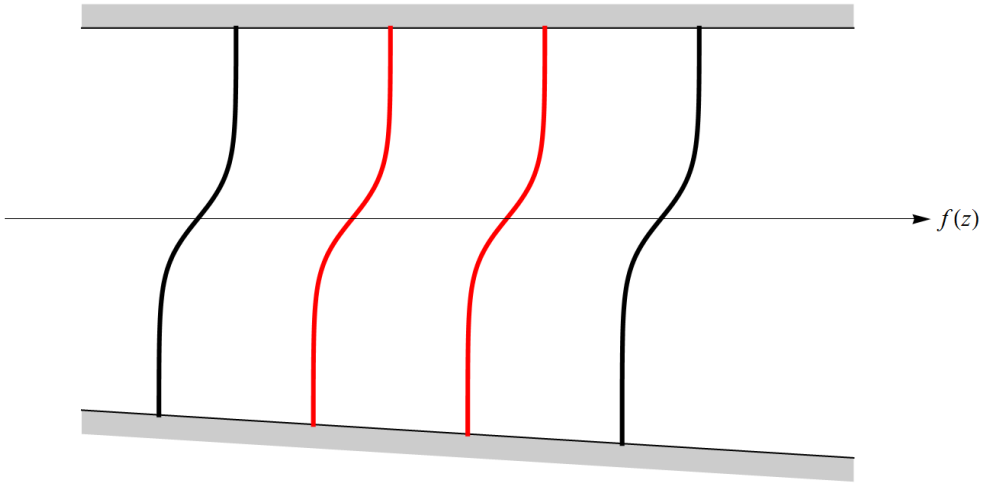

Figure 3.1: Model of near shore sea region with sloping bottom boundary. Red lines corresponds to locally absolutely stable regions and black lines to locally convectively unstable regions. This will result in a finite range of absolutely unstable flow in the streamwise direction.

depth dependence on the streamwise coordinate. We will see that it is necessary to obtain absolute instability results for complex value of this coordinate.

The variation of the bottom boundary in the region where absolute instability is present can be considered as a spatial variation of the whole flow, as shown in the model layout of the problem in figure 3.2. WKB theory provides the framework for studying waves in slowly varying flows, and local dispersion relations appear at leading order. The normal mode form for disturbances appropriate to parallel flow is replaced by a product of an envelope function that varies in the streamwise direction on the slow scale of the basic flow, and an exponential term that varies on the fast scale of

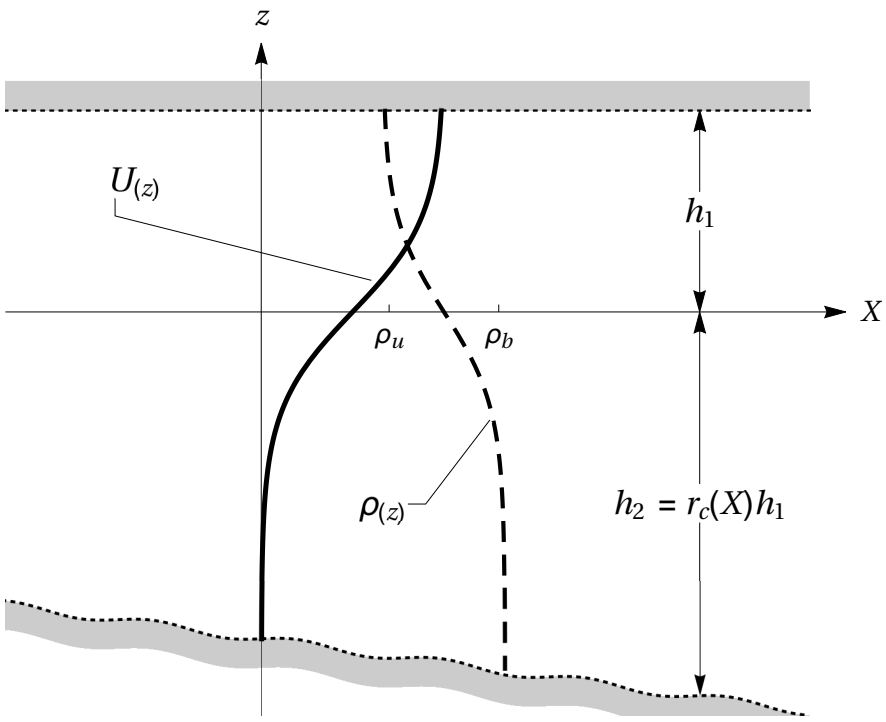

Figure 3.2: Model layout of the problem considered for global stability analysis with model velocity profile (2.23) and model density profile (2.24). h_1 and h_2 are the distances of the upper boundary and bottom boundary respectively from the center of the velocity shear. r_c is the parameter used in the description of our models and results and it is the ratio of the upper and bottom boundary. X describes the slow spatial variation (as defined in text) of the problem, slow in the sense that the depth varies slowly over the length scale of the wavelengths of interest, and hence the spatial variation of bottom boundary which is now X-dependent and $h_2 = r_c(X)h_1$.

the disturbance wavelength:

$$A(X)v(X,y)\exp i\left(\int \alpha(X)dX - \omega t\right). \tag{3.1}$$

The envelope function usually satisfies a first order differential equation of the form

$$\frac{\partial\omega_0}{\partial\alpha}A' + \{...\}A = 0, \tag{3.2}$$

whose solution describes the slow variation in the amplitude $A(X)$ of the wave in the streamwise direction due to non-parallel effects (there is also a faster amplitude dependence associated with the exponential term, which is determined by local dispersion relations). Note that $\{...\}$ in (3.2) indicates a coefficient that depends in a nontrivial way on X. The equation (3.1) has been used to calculate nonparallel corrections to convective instabilities (see Gaster 1974 [40], Smith 1979 [41] or Bertolotti, Herbert and Spalart 1992 [42]).

Global modes exist for frequencies ω_G such that $A \to 0$ as $X \to \pm\infty$, where ω_G is an eigenvalue. But in WKB theory, A satisfies a 1st order ODE (3.2), so only a single boundary condition can be satisfied except at a turning point, $X = X_t$, where $\partial\omega_0/\partial\alpha = 0$, and WKB theory fails because $A' \to \infty$. In such case the slow scale of the envelope speeds up, an inner turning point region is encountered, where A satisfies a second order ODE (3.3) instead of (3.2), and where two modes can interact. The generic form for the amplitude equation in the turning point region is

$$A'' - (X - X_t)A = 0, \tag{3.3}$$

which is essentially the Airy equation. When $X > X_t$ it has exponential type solutions, one growing and one decaying, and for $X < X_t$ it has oscillatory solutions. As shown in figure 3.3(a), near a local maximum in $\omega_{0i} = \omega_{0i}(X)$ a global mode can be constructed if an exponential solution that decays as $X \to -\infty$ can be connected to an oscillatory

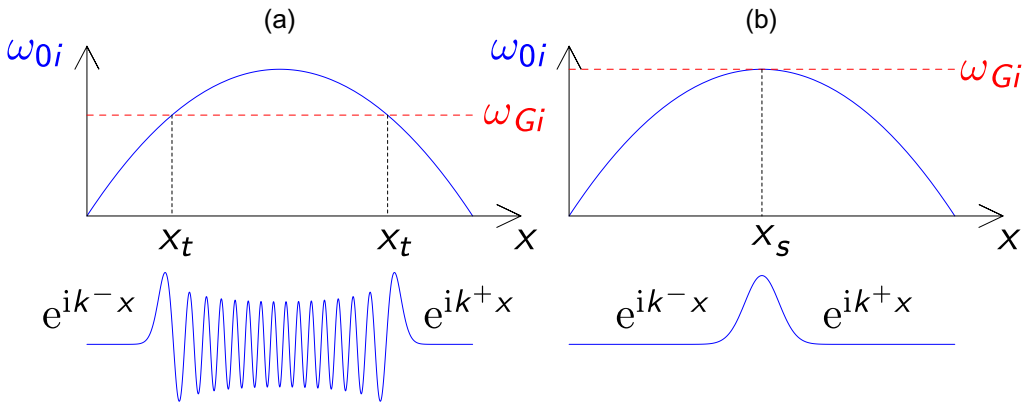

Figure 3.3: Behaviour of global mode solutions near a local maximum of ω_{0i} as a function of downstream coordinate X, showing a pair of global mode eigenfunctions where (a) is a generic global mode satisfying decay conditions as $X \to \pm\infty$ with turning points connecting oscillatory WKB solutions to exponential WKB solutions, and (b) is the most unstable global mode satisfying the double saddle condition (3.4).

solution at the turning point, X_t, and then this oscillatory solution connected to an exponential solution that decays as $X \to +\infty$ at second turning point X_t. At each of these turning points, an Airy equation like (3.3) arises but the linear coefficients near each X_t have opposite signs, so that near the left hand X_t, increasing X causes the exponential solution to convert to an oscillatory solution and near the right hand X_t, increasing X causes the oscillatory solution to convert to an exponential solution. The decaying exponential solutions on either side of the turning points can only be connected in this way at certain discrete frequencies, thus posing an eigenvalue problem, and these eigenvalues give the global mode frequencies. This is because in turning point regions, rather like in boundary layer regions , the order of the differential equations increases, and new boundary conditions can be satisfied. Equation (3.3) is allowing both upstream and downstream boundary conditions to be satisfied. However, the case of greatest interest is the global mode with the highest ω_{0i}, and this occurs in

the case shown in figure 3.3(b), at which two turning points coalesce to produce the saddle condition $\partial\omega_0/\partial X$ and then a solution decaying as $X \to -\infty$ connects directly to a solution decaying as $X \to +\infty$. Saddles of this type can be located in the complex $X-$plane by plotting contours of constant $\mathrm{Im}(\omega_0)$, in much the same way as the pinch-point saddle in Briggs' method for absolute instability can be found by plotting contours of constant $\mathrm{Im}(\omega)$ in the complex wavenumber plane. Hence the global mode has a turning point at X_t, where $\omega_G = \omega_0(X_t)$ and ω_0 is the local absolute frequency satisfying $\partial\omega_0/\partial\alpha = 0$. The most unstable global mode satisfies the saddle condition

$$\frac{\partial\omega_0}{\partial X} = 0, \quad \omega_G = \omega_0(X_s). \tag{3.4}$$

In general, X_s lies at complex X and since

$$\frac{\partial\omega_0}{\partial X} = \frac{\partial\omega_{0r}}{\partial X_r} + \mathrm{i}\,\frac{\partial\omega_{0i}}{\partial X_i} = 0, \tag{3.5}$$

both real and imaginary parts of (3.5) must be set to zero. However, in the special case, when ω_{0r} = constant and $\partial\omega_{0r}/\partial X_r = 0$, X_s lies on real X axis, and $\omega_{Gi} = \max(\omega_{0i})$ along real X axis. The global frequency is then given by the strongest absolute instability in the flow. If $\omega_{0r} \neq$ constant and $\partial\omega_{0r}/\partial X_r \neq 0$, which is referred to as detuning in the work of Davies (2007 [29], 2010 [30], 2013 [31] and 2016 [32]), then X_s is complex and we must integrate through the saddle as shown in figure 3.4. For such a saddle to contribute a global mode there is a further condition that must be satisfied: the integration path must lie within anti-Stokes lines, along which there is an exchange between dominant and sub-dominant WKB solutions. It is necessary for sub-dominant solutions to be continued back to real X axis to ensure that the principal of causality is respected. This is analogous to the pinch-point criterion for the saddle point in absolute instability calculations. These are highly technical issues, and a full

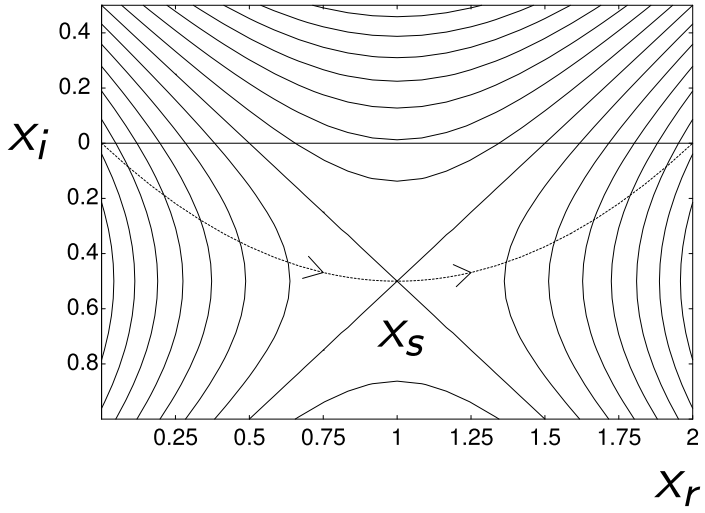

Figure 3.4: Deformation of integration contour (dashed line), following the steepest decent path, in the complex X-plane passing through the saddle point.

discussion can be found in Huerre 2000 [12] and in the references contained therein. Huerre and Monkewitz 1990 [20] implicitly assumed that anti-Stokes lines coincide with the contours of ω_{0i}, i.e. the integration path follows a steepest descent path through the saddle. Although this is not necessarily true if the saddle is far from the real X axis, we shall make the same assumption in this thesis.

At leading order the global mode frequency at the saddle point where

$$\frac{\partial \omega}{\partial \alpha} = 0 \text{ and } \frac{\partial \omega}{\partial X} = 0 \tag{3.6}$$

is given by

$$\omega_G = \omega_0(X_s) \tag{3.7}$$

where X is the new complex spatial variable, $X = X_s$ at the saddle satisfying (3.6) and $\omega_0(X_s)$ is the absolute instability frequency at the saddle (see Huerre & Monkewitz 1990 [20]). X is the slow spatial variable compared to x (which appears in the complex exponential wavy term), where X varies slowly compared to the scale of the

wavelengths of the disturbances that we are interested in. In problems or regions where the boundary remains parallel along the spatial axis and where as a result $\frac{\partial \omega}{\partial X} = 0$ is satisfied, the value of the resultant global mode frequency is the value of the absolute frequency which can be find using the analysis presented in chapter 2 for given parameters J_0, h_1 and r_c. Hence bounded parallel flows in nature or experiments which are in such a regime, where J_0, h_1 and r_c result in absolute instability, will be also globally unstable. This suggests, as discussed earlier in the work of Matas (see chapter 1), that some previous results of stability analysis in nature or experiments should have been considered with boundaries and not as unbounded flows for better results. For example, Strang and Fernando 2001 [43] conducted a series of experiments on mixing in parallel stratified shear flows and they found discrepancies when compared with the linear stability results of Lawrence and Haigh 1999 [44]. However the work of Lawrence and Haigh assumed the flow to be unbounded and they considered only a temporal stability analysis, where in the experiment of Strang and Fernando the flow is clearly bounded by the bottom of their experimental tank and by the surface of the flow. This suggests that this work should be revisited in the light of absolute/global instability analysis for bounded flows. Unfortunately we were not able to retrieve the parameters for the boundaries from their published paper, nor from them via email, and hence we were not able to consider this scenario in our investigation. On the other hand if the parameter regime is known the results are essentially presented in our work and need only to be identified using Strang's parameters from their experiment.

In addition if the bottom boundary has minima, maxima or an inflection point, where $\frac{dr_c}{dX} = 0$ and the stationary point is in the absolutely unstable parameter regime, then there will be a globally unstable mode since $\omega = \omega(r_c)$ and hence $\frac{dr_c}{dX} = 0 \implies \frac{\partial \omega}{\partial X} = 0$ by the chain rule. In addition, we show that there are globally unstable modes

for monotonic decreasing (or increasing) boundaries where $\frac{\partial \omega}{\partial X} = 0$, but not along the real X-axis, which is an unexpected result, where the $\frac{\partial \omega}{\partial X} = 0$ saddles are in the complex plane away from the real $X-$axis. Our model also includes monotonically increasing/decreasing boundaries, as well as minima, maxima or inflection point, for values of $h_1 = 10, 5, 1$ and 0.8. Values of $h_1 \leq 0.75$ are shown to be stable from absolute stability results in figure 2.19 and therefore do not need to be considered. Furthermore values of $h_1 \geq 6$ have stabilizing effect on absolute stability results and in addition the resultant growth rates of absolutely unstable modes for $h_1 = 10$ are ten times smaller that those for $h_1 = 1$ (see again figure 2.17), hence the largest considered $h_1 = 10$ is sufficient for our analysis.

Next we define a function describing the variation of sea bed to be the cubic function

$$r_c(X) = X^3 + r_1 X + r_0, \tag{3.8}$$

which is the ratio coefficient for the bottom boundary $h_2 = r_c(X)h_1$ dependent on the slow spatial variable X. (3.8) is a convenient example that generates both monotonically and non-monotonically varying boundaries depending on the sign of r_1 and the stationary values of r_c can be moved into, or out of, the range for absolute instability by adjusting r_0. The r_c in (3.8) has stationary points $dr_c/dX = 0$ at $X = \pm(-r_1/3)^{1/2}$. Both local minima and local maxima of r_c (and therefore of h_2) will produce global instability if the depth at the stationary value of X lies in the parameter space where AI is present shown in figure 2.17.

Note that since in the absolute stability analysis result, as shown in figure 2.19, we have shown that the maximum growth rates are associated with the ratio of boundaries $r_c \approx 2.5$ for all considered parameters of h_1 and J_0, we will fix the r_0 coefficient in (3.8) to $r_0 = 2.5$, which means that there will always be a neighbourhood of the origin with

absolute instability.

3.1 Preliminary investigation of global instability of homogeneous vortex sheet with non-parallel confinement

First we consider the same situation as in figure 3.2 with $h_1 = 1$, $h_2 = r_c(X)h_1$ and constant density $\rho(z)$, but we change the velocity profile to be defined as

$$U(z) = \begin{cases} 1, & \text{for } 0 < z \leq 1. \\ 0, & \text{for } -h_2 \leq z < 0. \end{cases} \tag{3.9}$$

for which the local dispersion relation is

$$\Delta_0 = -\frac{(\omega - \alpha)^2}{\alpha} \coth \alpha - \frac{\omega^2}{\alpha} \coth[\alpha h_2] = 0 \tag{3.10}$$

The dependence on h_2 of the absolute growth rate $\mathrm{Im}(\omega)$ is shown in figure 3.5. This shows that there is an absolutely unstable region when $2.3467 < h_2 < 2.7245$ this is already dramatically smaller than in the case of smooth tanh profiles considerer with far away placed boundaries (see next section for $h_1 = 10$ and $h_2 = 25$). Despite the fact that this absolute instability is weaker, than for the tanh profile, it has the same qualitative behaviour, and allows preliminary investigation to be carried out much more quickly and easily than for the full problem. We can use this to identify interesting behaviour and parameter regimes that can then be used in the full problem. We can now consider the spatial variation of the absolute instability with the same variation of bottom boundary as in the previous case using the $r_c(X)$ equation (3.8). For this demonstration of the piecewise linear approximation we consider only few examples because the piecewise linear approximation will only apply for far away enough placed

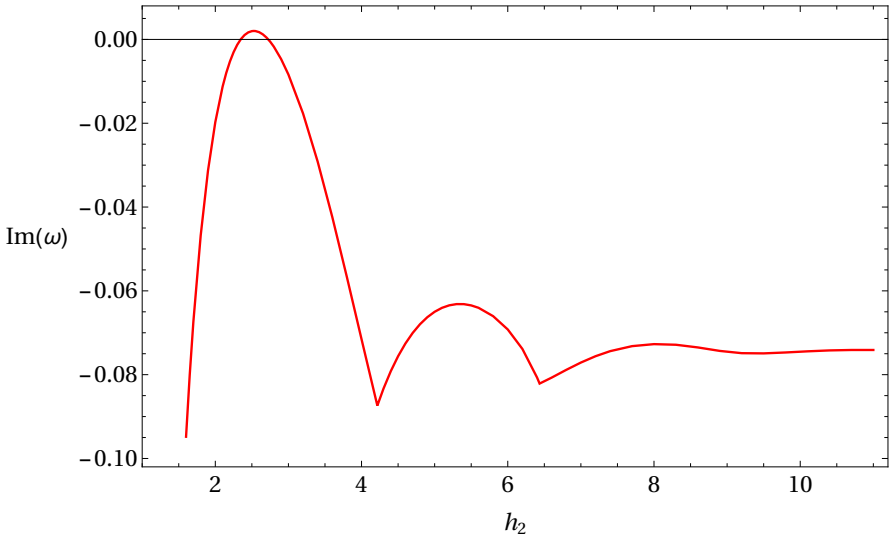

Figure 3.5: Absolute stability results. Dependence on h_2 of the absolute frequency $\mathrm{Im}(\omega)$ (red line) for the local dispersion relation (3.10) for the vortex sheet velocity profile (3.9).

boundaries for which the flow is independent of the velocity profile curvature around the shear layer.

First we look at a sea bed with both maxima and minima which can be described by

$$r_c(X) = X^3 - 0.5X + 2.5, \tag{3.11}$$

for which the results are shown in figure 3.6. Note that a saddle in these diagrams only produces a global mode if the solution can be followed from the saddle point back to the real axis in the valleys of the saddle point rather like the pinch point criterion, but now in the complex $X-$plane instead of the complex $\alpha-$plane (see Huerre and Monkewitz 1990 [20] for details). This is important because although in figure 3.6 both saddles contribute global modes, in the monotonic case only one of the saddles contribute a global mode.

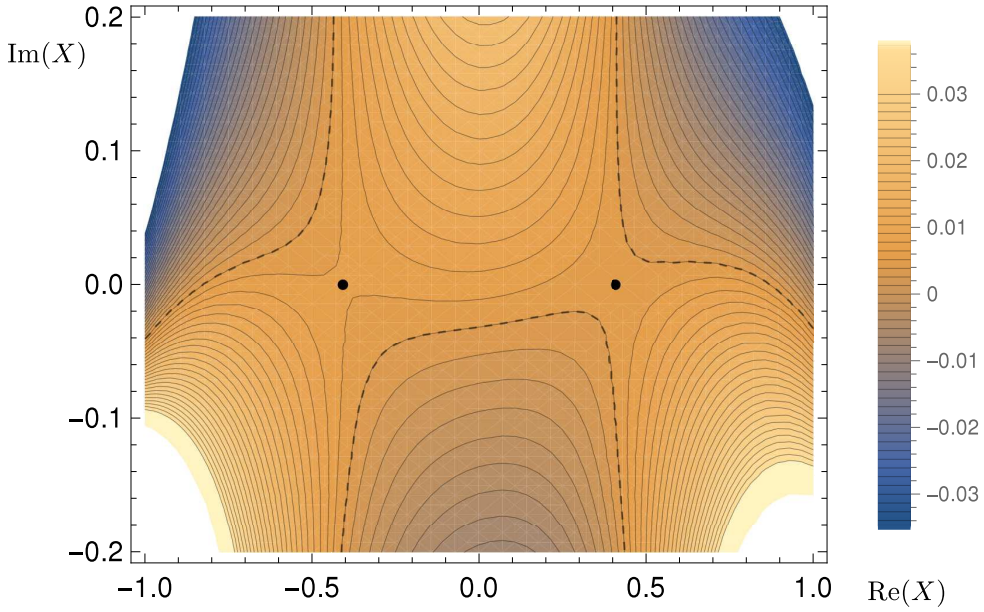

Figure 3.6: Global stability results. Contours of constant $\mathrm{Im}(\omega)$ at pinch points in the complex X plane for varying bottom boundary with $r_c(X)$ given by (3.11) and with vortex sheet velocity profile. Dashed lines are $\mathrm{Im}(\omega) = 0$ contours and the solid discs are the double saddle points satisfying (3.6), which occur at the stationary values $dr_c/dX = 0$ when $X = \pm(-r_1/3)^{1/2}$ in (3.11).

As seen from the results for the sea bed with maxima and minima for vortex sheet velocity profile in figure 3.6 and for the smooth tanh velocity profile shown in figure 3.10, the piecewise linear approximation to smooth tanh velocity profiles is appropriate if the distance to the boundaries are great enough, as in our example, where $h_1 = 10$ and $h_2 = 25$.

In the second example with the vortex sheet approximation, we consider a sea bed with an inflection point as follows

$$r_c(X) = X^3 + 2.5. \tag{3.12}$$

The complex X plane for the sea bed with the inflection point is shown in figure 3.7.

As seen from the results for the sea bed with the inflection point for the vortex

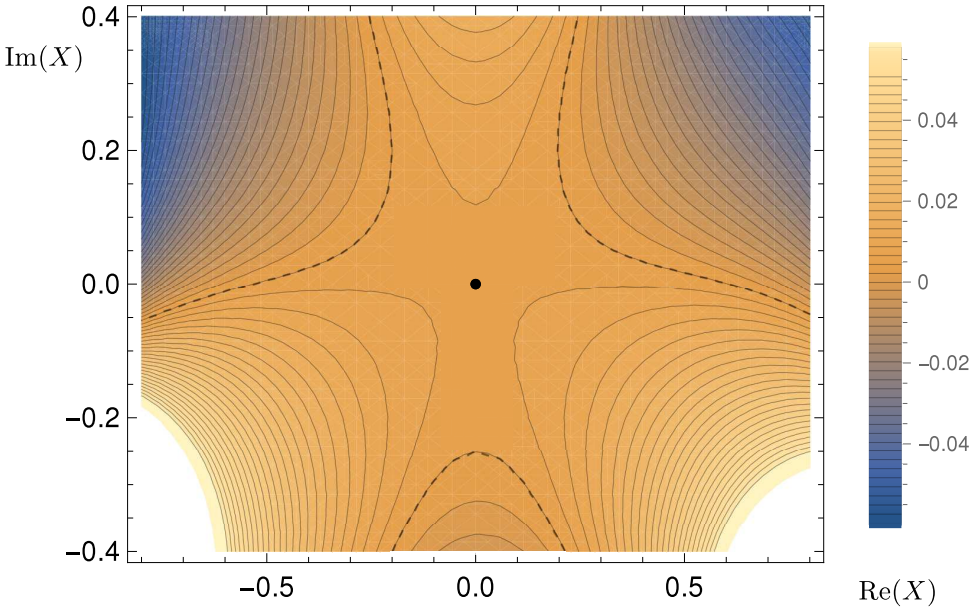

Figure 3.7: Global stability results. Contour of constant $\mathrm{Im}(\omega)$ at pinch points in the complex X plane for varying bottom boundary with r_c given by (3.12) with vortex sheet velocity profile. Dashed lines are $\mathrm{Im}(\omega) = 0$ contours and the solid discs are the double saddle points satisfying (3.6), which occurs at the stationary values $dr_c/dX = 0$ when $X = 0$ in (3.12).

sheet velocity profile in figure 3.7 and the smooth tanh velocity profile in figure 3.11 in the next section, the piecewise linear approximation to smooth tanh velocity profiles is in good agreement if the distance to the boundaries is large enough.

In the last example with the vortex sheet approximation, we consider a monotonically varying sea bed without any maxima, minima or inflection point as follows

$$r_c(X) = X^3 + 0.123X + 2.5. \tag{3.13}$$

The complex X plane for the sea bed with the inflection point is shown in figure 3.7.

As seen from the results for the sea bed with the inflection point for the vortex sheet velocity profile in figure 3.8 and the smooth tanh velocity profile in figure 3.12 in the next section, the piecewise linear approximation to smooth tanh velocity profiles

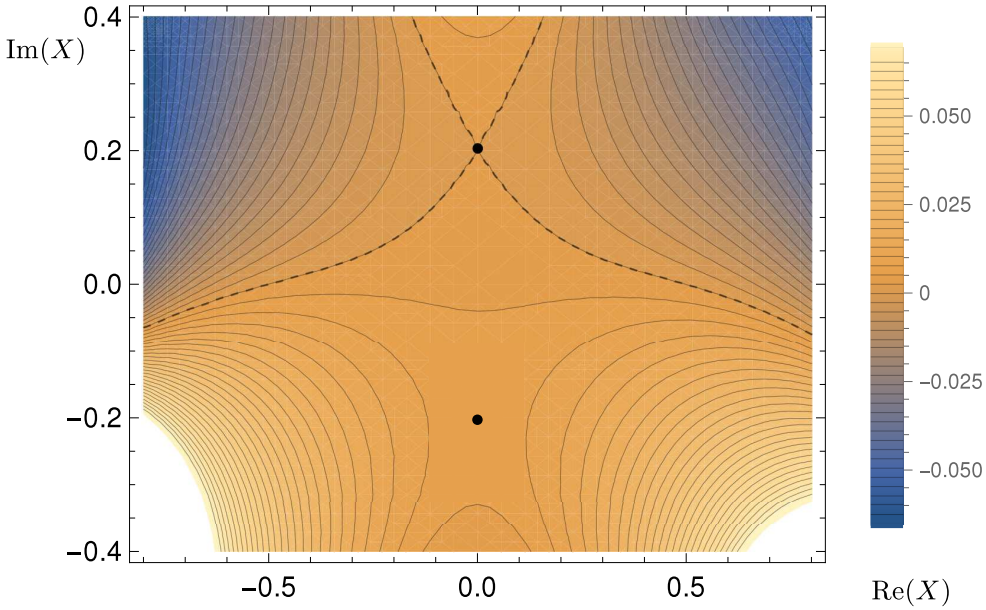

Figure 3.8: Global stability results. Contour of constant $\mathrm{Im}(\omega)$ at pinch points in the complex X plane for varying bottom boundary with r_c given by (3.13) with vortex sheet velocity profile. Dashed lines are $\mathrm{Im}(\omega) = 0$ contours and the solid discs are the double saddle points satisfying (3.6).

is in good agreement if the distance to the boundaries is large enough.

Therefore, in our next example, we fix $h_1 = 10$ and $h_2 = 25$, which can be considered as a limiting case satisfying the use of preliminary investigation of a bounded vortex sheet problem. A key feature of the global mode theory discussed by Huerre and Monkewitz 1990 [20] is that the wave envelope of the global modes must decay to zero as $X \to \pm\infty$. This is expected when the absolutely unstable region is of finite spatial extend, and is surrounded by only convectively unstable flow. It can be seen that this is the case in figures 3.6, 3.7 and 3.8 for the vortex sheet model.

3.2 Homogeneous problem of smooth velocity profile with $h_1 = 10$

First we consider upper boundary which is relatively far from the middle of the shear layer, which has a stabilizing effect from absolute stability analysis if $h_1 \geq 6$ as shown in absolute stability analysis result figure 2.17. For example we consider $h_1 = 10$ and look at the cases of a linear sea bed (where the coefficient of cubic term in 3.8 is zero), a sea bed with maxima and minima, a sea bed with an inflection point and a monotonically decreasing sea bed, for which the results are presented in figures 3.9,3.10, 3.11 and 3.12 respectively. The considered model problems and results are given in table 3.1, which summarize the effect of model spatial variation of bottom boundary as discussed above.

For the linearly varying sea bed boundary we consider (3.8) with the coefficient of the cubic term set to zero and we chose coefficient $r_1 = 1$. Coefficient $r_0 = 2.5$ which results in the maximum absolutely unstable growth rate been positioned at the origin of the results plots, which gives

$$r_c(X) = X + 2.5. \tag{3.14}$$

Any saddles satisfying (3.6) can be found by plotting contours of constant $\mathrm{Im}(\omega)$ for pinch points calculated for complex values of X, essentially continuing the results presented in figure 2.19 for real X into the complex X plane. The results for (3.14) are shown in figure 3.9. In the linear sloping sea bed result for $h_1 = 10$, as shown in figure 3.9, the end points of the locally absolutely unstable region, $-0.540 < X < 0.352$ (or $1.960 < r_c(X) < 2.853$) , appear now as intersection of the $\mathrm{Im}(\omega) = 0$ contour with the real X axis. As seen in figure 3.9, there is no appearance of a double saddle satisfying (3.6) and therefore the problem with linearly varying sloping bottom boundary will

Parameters h_1 and r_c	Dominant mode of the problem	
	Frequency	Wavenumber
Case i) $r_c = X + 2.5$	globally stable	
Case ii) $r_c = X^3 - 0.5X + 2.5$	$\omega = 0.0928 + \text{i } 0.002$	$\alpha = 0.0587 - \text{i } 0.1067$
Case iii) $r_c = X^3 + 2.5$	$\omega = 0.0907 + \text{i } 0.0011$	$\alpha = 0.0544 - \text{i } 0.1042$
Case iv) $r_c = X^3 + 2.27X + 2.5$	$\omega = 0.0901 + \text{i } 0$	$\alpha = 0.0503 - \text{i } 0.1066$

Table 3.1: Parameter regimes of model problems (as shown in figure 3.2) considered for global stability analysis. Velocity is given by (2.23) and density is constant. The variation is given by considering different functions for spatial variation of lower boundary $h_2 = r_c(X)h_1$, given by the function $r_c(X)$, where X is the slowly varying spatial variable. Upper boundary is placed at $h_1 = 10$.

not be globally unstable despite the fact that in the region where $-0.540 < X < 0.352$ (or $1.960 < r_c(X) < 2.853$) it is still absolutely unstable. Nevertheless the region of absolute instability is comparable with the vortex sheet approximation in this region is $2.3467 < h_2 < 2.7245$ as shown in figure 3.5.

The major difficulty in obtaining results in the complex $X-$plane (such as in figure 3.9) is the fact that at every point in the complex $X-$plane we have to find the pinch-point in the complex $\alpha-$plane, which can be problematic because confined flows produce lots of saddle points (as discussed in chapter 2), for which the interpolating functions need to be carefully constructed. The parameters for the boundaries h_1 and $h_2 = r_c h_1$ considered in the absolute stability analysis for smooth tanh profiles were such that the results captured the absolutely unstable region for maximum of

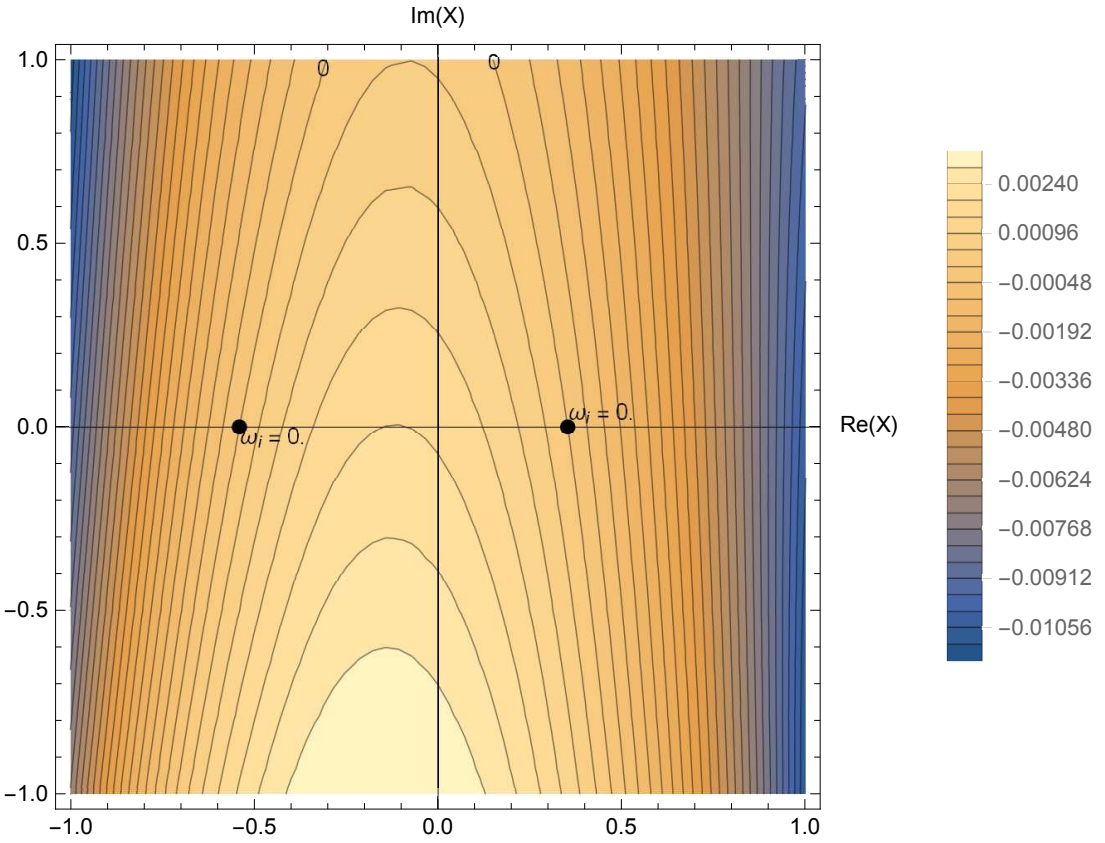

Figure 3.9: Global stability results, case i) in table 3.1. Contour of constant $\mathrm{Im}(\omega)$ at pinch points in the complex X plane for linearly varying bottom boundary with r_c given by (3.14) with upper boundary placed at $h_1 = 10$. $\mathrm{Im}(\omega) = 0$ contour is labelled and the solid discs are the intersections of the zero contour with the real X-axis at -0.540 and 0.352 respectively.

$h_1 = 10$, after which the growth rates are at least ten times smaller than for $h_1 = 6$ (see chapter 2). In chapter 2 we have also shown that there is no absolute instability for $h_1 < 0.75$ and therefore the range of h_1 for which the absolute stability analysis is considered is $0.75 < h_1 < 10$. The parameter range for the bottom boundary where $1.7 < r_c < 4.1$ captures all absolutely unstable regions for variations of r_c. Hence prior to global stability analysis, where we are methodologically following the most absolutely unstable saddle as the bottom boundary h_2 varies, we only have the data for which

$0.75 < h_1 < 10$ and $1.7 < r_c < 4.1$ (inside which the absolute instability occurs). For easier comparison of global stability results for smooth tanh profiles we fixed the range of parameters of our results to be $-1 < Re[X] < 1$ and $-1 < Im[X] < 1$, which means that there are regions in results far from the origin where the data are missing and the automatic extrapolation in Mathematica [9] was used, and hence those parts of the diagrams should not be considered. However the most important parts of the results which are around the saddles have all the data in neighbouring region and are correct. In addition to this restriction sometimes, the results, do not clearly show the requirement of absolute growth rate to become negative as $X \to \pm\infty$ (see later results 3.10, 3.12, 3.14, 3.18 and 3.22). This analysis required lots of computing power and time. The reason is that the calculations often had to be restarted because our pinch point algorithm could easily fail to locate the pinch point.

For a sea bed with both maxima and minima, we consider (3.8) with coefficients fixed as follows

$$r_c(X) = X^3 - 0.5X + 2.5, \tag{3.15}$$

for which the results are shown in figure 3.10 In the results for this sea bed for $h_1 = 10$ as shown in figure 3.10 we have two double saddles which are associated with the stationary values of $dr_c/dX = 0$ along the real X-axis, where $X = \pm(-r_1/3)^{1/2}$ in (3.8). So for $r_1 = -0.5$ the position of the double saddles is at $X = \pm 0.408$. The global mode frequency is determined by the absolute frequency at a saddle point, and in figure 3.10 there are two such saddles where there is a absolute instability, and therefore this flow is globally unstable. In fact both a minimum and a maximum in $r_c(X)$ can produce global instability if they are at the right height. The general solution will be a superposition of the growing global modes associated with each saddle, and will eventually be dominated by the most amplified mode, which will be the one with

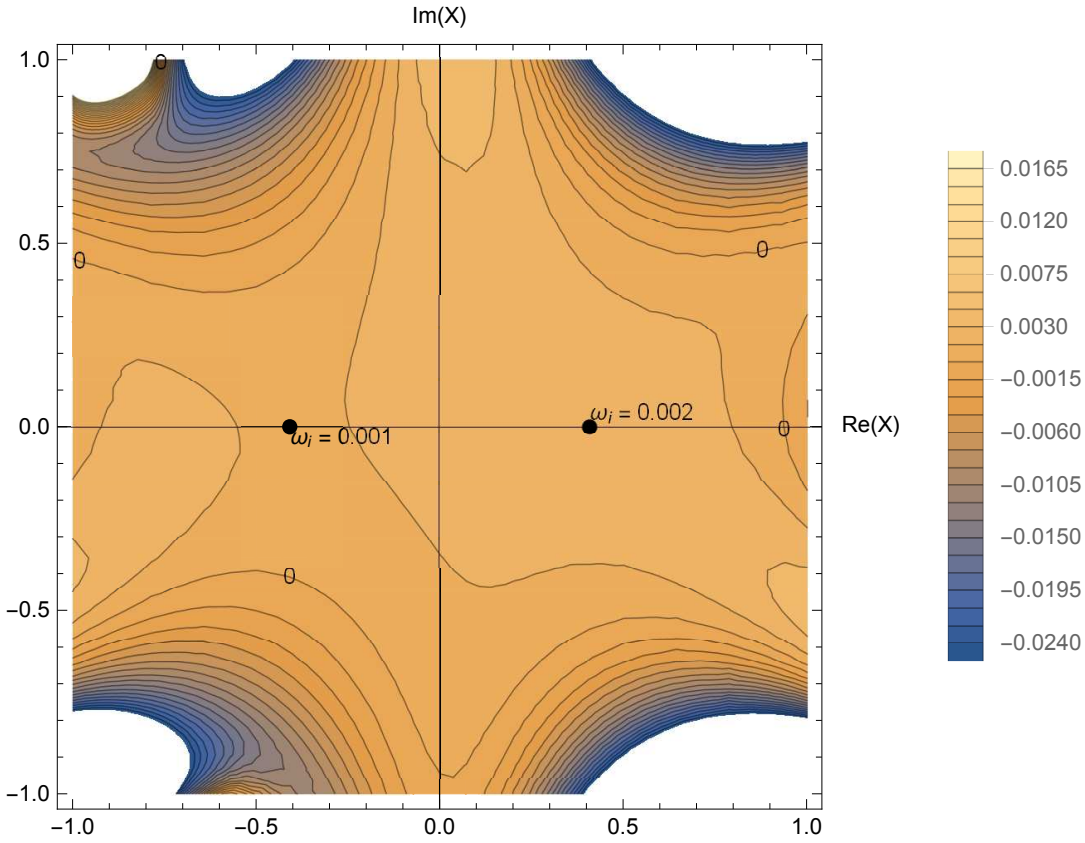

Figure 3.10: Global stability results, case ii) in table 3.1. Contour of constant $\mathrm{Im}(\omega)$ at pinch points in the complex X plane for varying bottom boundary with r_c given by (3.15), and with upper boundary placed at $h_1 = 10$. $\mathrm{Im}(\omega) = 0$ contour is labelled and the solid discs are the double saddle points satisfying (3.6), which occurs at the stationary values $dr_c/dX = 0$ when $X = \pm(-r_1/3)^{1/2}$ in (3.8).

larger $\mathrm{Im}(\omega)$, the right hand one in this example in figure 3.10. Note that in the figure 3.10 as $Re(X) \to -\infty$ the requirement that the dispersion relation decays as $Re(X) \to \pm\infty-$ is no evident, and this is due to the missing data, but it is clear in the case of vortex sheet approximation shown in figure 3.6.

If there is more than one stationary value of X, and they lie outside the depth range for absolute instability, then although the flow will be globally stable, the su-

perposition of the global modes associated with each stationary point may display a transient growth. This would be a non-modal global transient growth mechanism, which might produce sufficient growth to produce a non-linear response. Non-linear hydrodynamics is however not considered in this work, but might be considered in future work.

There is a special case where a pair of double saddles, each satisfying (3.6), coalesce, which occurs at $r_1 = 0$. Therefore for a sea bed with an inflection point we consider (3.8) with coefficients fixed as follows

$$r_c(X) = X^3 + 2.5, \tag{3.16}$$

for which the results are shown in figure 3.11. The complex X plane for the sea bed with an inflection point is shown in figure 3.11. So far we have been able to satisfy the double saddle condition (3.6) along the real X-axis by considering sea bed profiles with maxima, minima or inflection point.

The stationary points of r_c in (3.6) move off the real X-axis and into the complex X plane when $r_1 \geq 0$, which corresponds to a monotonically increasing depth of the sea bed. As r_1 increases, and the stationary point $dr_c/dX = 0$ moves further from the real X axis, $\mathrm{Im}(\omega)$ reduces. The largest positive value r_1 that supports global instability is found to be $r_1 = 2.27$, which leads to an equation for r_c as follows,

$$r_c(X) = X^3 + 2.27X + 2.5. \tag{3.17}$$

Figure 3.12 shows the results for the largest positive value $r_1 = 2.27$ that supports global instability. There are two double saddles satisfying (3.6) in the results shown in figure 3.12, but only the one in upper half plane is considered, since we can not deform the integration path through the saddle point in the lower half plane. The deformation of the integration path must be done so that we follow the steepest descent path (i.e.

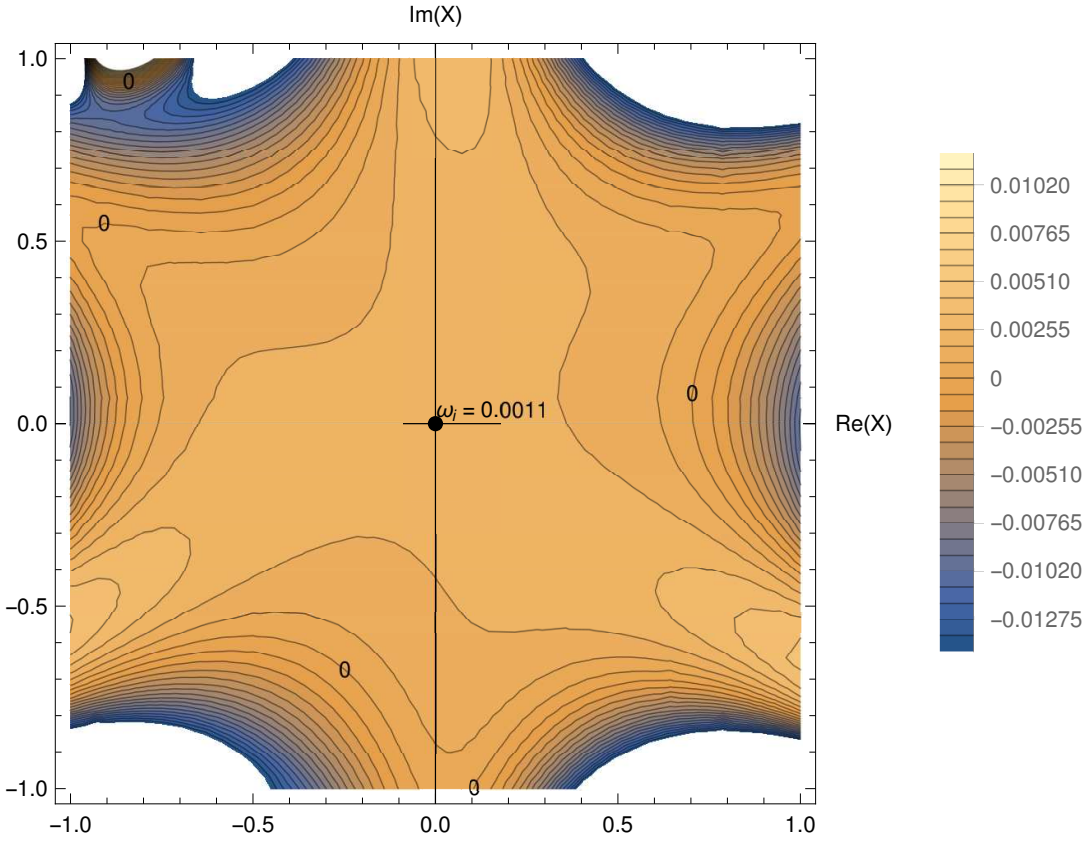

Figure 3.11: Global stability results, case iii) in table 3.1. Contour of constant $\mathrm{Im}(\omega)$ at pinch points in the complex X plane for varying bottom boundary with r_c given by (3.16), and with upper boundary placed at $h_1 = 10$. $\mathrm{Im}(\omega) = 0$ contour is labelled and the solid disc is the double saddle points satisfying (3.6), which occurs at the stationary value $dr_c/dX = 0$ when $X = 0$ in (3.8).

stay in the valleys of the results).

When h_1 is reduced there is a stronger absolute instability, which motivates the following sections.

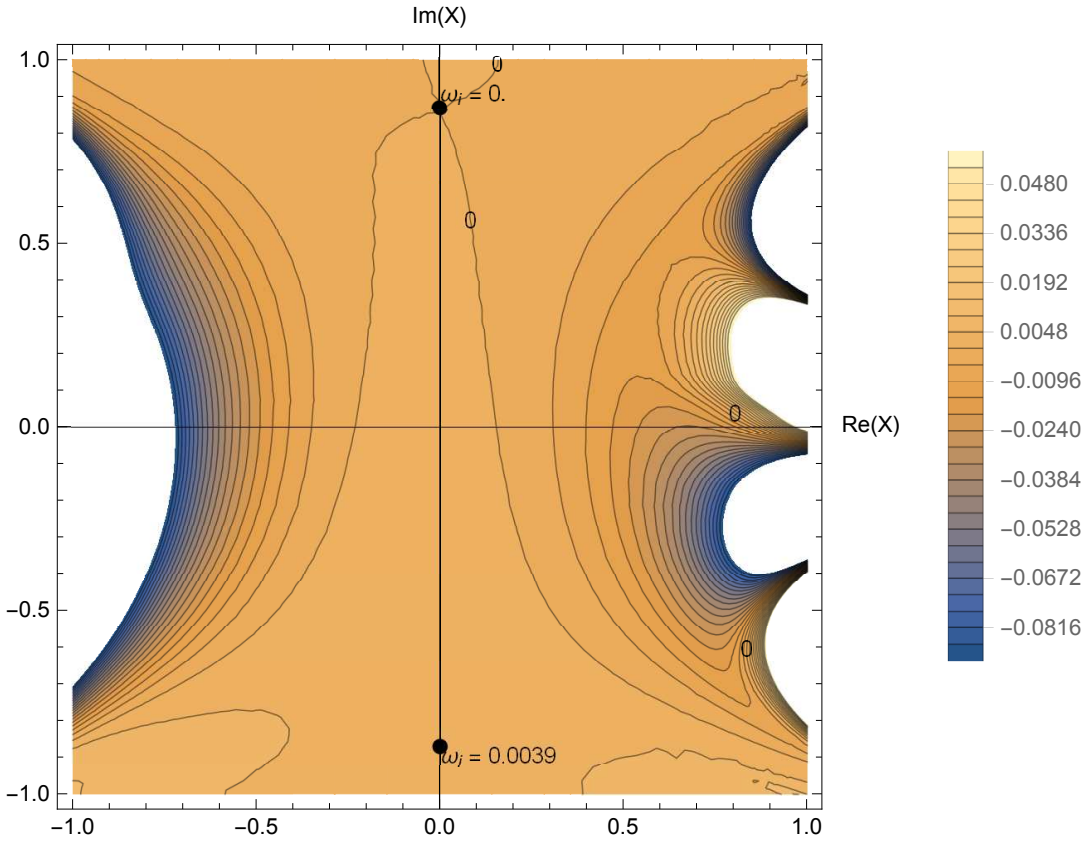

Figure 3.12: Global stability results, case iv) in table 3.1. Contour of constant Im(ω) at pinch points in the complex X plane for varying bottom boundary with r_c given by (3.17), and with upper boundary placed at $h_1 = 10$. Im(ω) = 0 contour is labelled and the solid discs are the double saddle points satisfying (3.6).

3.3 Homogeneous problem of smooth velocity profile with $h_1 = 5$

The next examples we consider have upper boundary fixed at $h_1 = 5$ and we look at the linear sea bed, sea bed with maxima and minima, sea bed with inflection point and monotonically decreasing sea bed for which the results are presented in figures 3.13,3.14, 3.15 and 3.16 respectively. The considered model problems and results are

Parameters h_1 and r_c	Dominant mode of the problem	
	Frequency	Wavenumber
Case i) $r_c = X + 2.5$	globally stable	
Case ii) $r_c = X^3 - 0.5X + 2.5$	$\omega = 0.1785 + \text{i } 0.0020$	$\alpha = 0.1190 - \text{i } 0.2045$
Case iii) $r_c = X^3 + 2.5$	$\omega = 0.1756 + \text{i } 0.0038$	$\alpha = 0.1162 - \text{i } 0.1983$
Case iv) $r_c = X^3 + 1.595X + 2.5$	$\omega = 0.1760 + \text{i } 0$	$\alpha = 0.1123 - \text{i } 0.2036$

Table 3.2: Parameter regimes of model problems (as shown in figure 3.2) considered for global stability analysis. Velocity is given by (2.23) and density is constant. The variation is given by considering different functions for spatial variation of lower boundary $h_2 = r_c(X)h_1$, given by the function $r_c(X)$, where X is the slowly varying spatial variable. Upper boundary is placed at $h_1 = 5$.

given in table 3.2, which summarize the effect of model spatial variation of bottom boundary as discussed above.

For linearly varying sea bed boundary we consider (3.14), for which the results are shown in figure 3.13. In the linear sloping sea bed result for $h_1 = 5$ shown in figure 3.13 the endpoints of the locally absolutely unstable region, $-0.454 < X < 0.688$ (or $2.046 < r_c(X) < 3.188$) , appear now at the intersections of the $\text{Im}(\omega) = 0$ contour with the real X axis. As in previous linearly sloping sea bed, there is no appearance of a double saddle satisfying (3.6) and therefore the problem with linearly varying sloping bottom boundary will not be globally unstable despite the fact that in the region where $-0.454 < X < 0.688$ (or $2.046 < r_c(X) < 3.188$) it is absolutely unstable. On the other hand in comparison with the results for $h_1 = 10$ in figure 3.9 we can see the increase

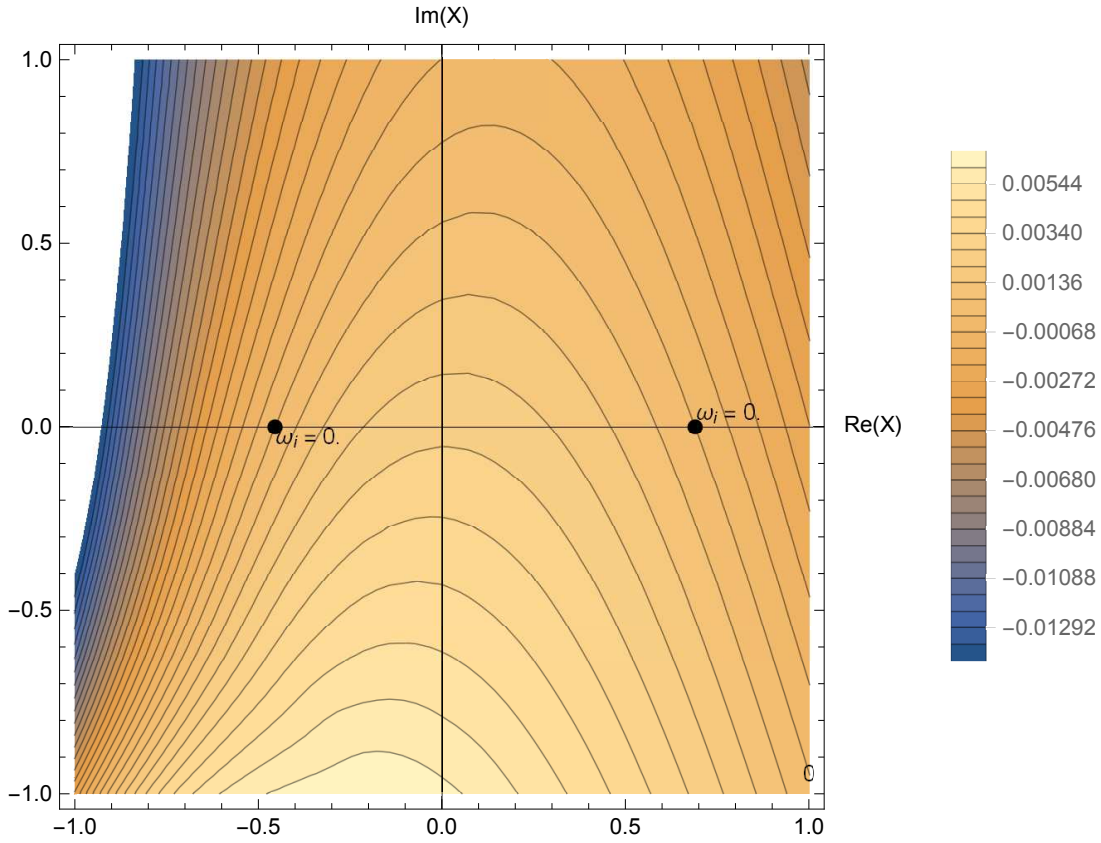

Figure 3.13: Global stability results, case i) in table 3.2. Contours of constant $\mathrm{Im}(\omega)$ at pinch points in the complex X plane for linearly varying bottom boundary with r_c given by (3.14), and with upper boundary placed at $h_1 = 5$. $\mathrm{Im}(\omega) = 0$ contour is labelled and the solid discs are the intersections of the zero contour with the real X-axis at $X = -0.454$ and $X = 0.688$ respectively.

of the range of parameter space where absolute instability is present, which also agrees with the results of absolute stability analysis in figure 2.19. For sea bed with both, maxima and minima, we consider (3.15), and for which the results are shown in figure 3.14. As shown in figure 3.13 there are two double saddles which are associated with the stationary values of $dr_c/dX = 0$ along the real X-axis, where $X = \pm(-r_1/3)^{1/2}$ in (3.8). So for $r_1 = -0.5$ the position at which global instability will be present is at $X = \pm 0.408$.

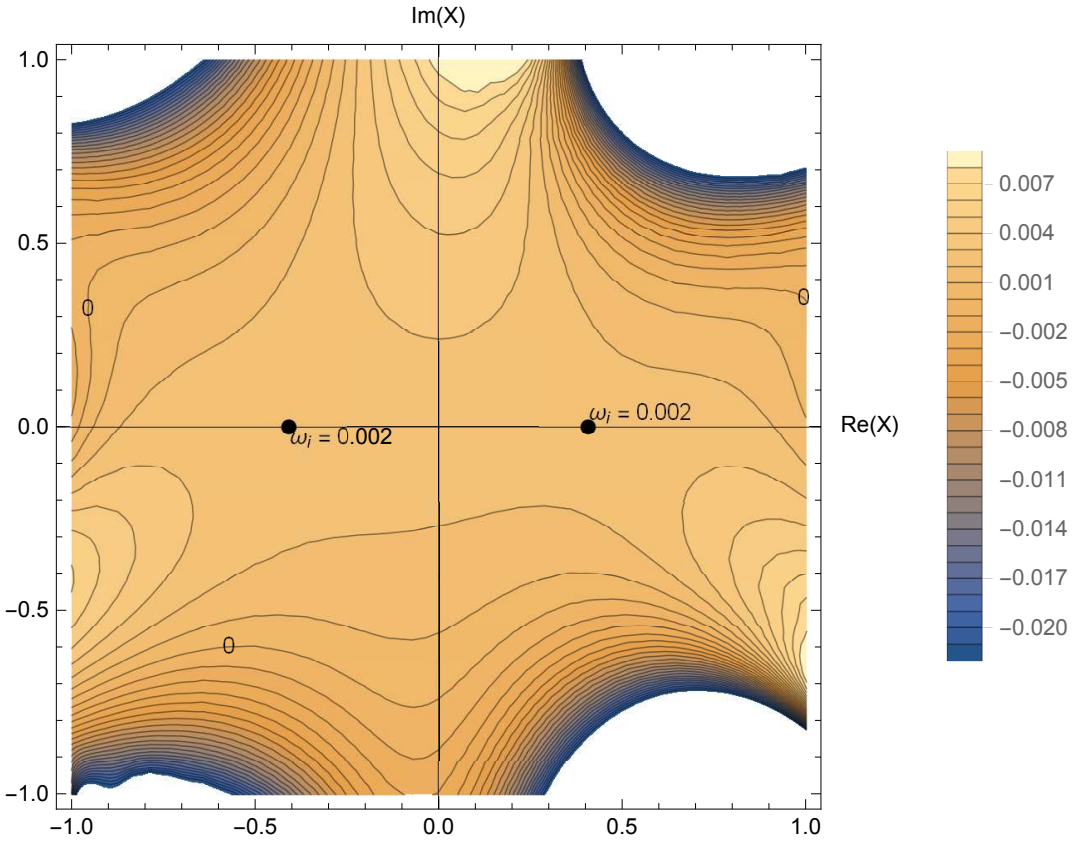

Figure 3.14: Global stability results, case ii) in table 3.2. Contour of constant $\mathrm{Im}(\omega)$ at pinch points in the complex X plane for varying bottom boundary with r_c given by (3.15), and with upper boundary placed at $h_1 = 5$. $\mathrm{Im}(\omega) = 0$ contours are labelled and the solid discs are the double saddle points satisfying (3.6), which occurs at the stationary values $dr_c/dX = 0$ when $X = \pm(-r_1/3)^{1/2}$ in (3.8).

For a sea bed with an inflection point we consider (3.16), and for which the results are shown in figure 3.15. The complex X plane for this sea bed is shown in figure 3.15. Again we are able to satisfy the double saddle condition (3.6) along the real X-axis by considering sea bed profiles with maxima, minima or inflection point.

When $r_1 > 0$ the stationary points lie in away from the real $X-$axis in the complex $X-$plane, and as r_1 increases, they move further from the real X axis, and

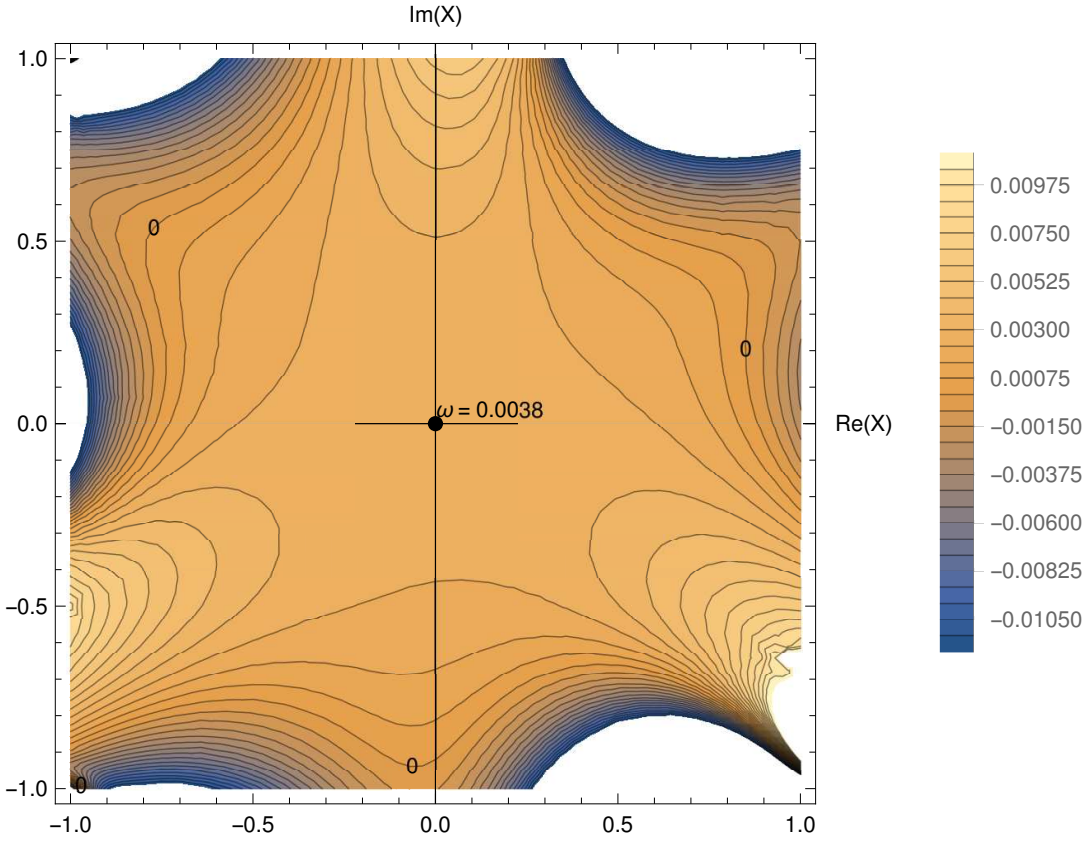

Figure 3.15: Global stability results, case iii) in table 3.2. Contours of constant Im(ω) at pinch points in the complex X plane for varying bottom boundary with r_c given by (3.16), and with upper boundary placed at $h_1 = 5$. Im(ω) = 0 contours are labelled and the solid disc is the double saddle points satisfying (3.6), which occurs at the stationary value $dr_c/dX = 0$ when $X = 0$ in (3.8).

then Im(ω) reduces. The largest positive value r_1 that supports global instability (for $h_1 = 5$) is found to be $r_1 = 1.595$, which leads to equation for r_c as follows,

$$r_c(X) = X^3 + 1.595X + 2.5. \tag{3.18}$$

Figure 3.16 shows the results for the largest positive value $r_1 = 1.595$ that supports global instability with upper boundary fixed at $h_1 = 5$. There are two double saddles satisfying (3.6) in the results shown in figure 3.16, but only the one in the

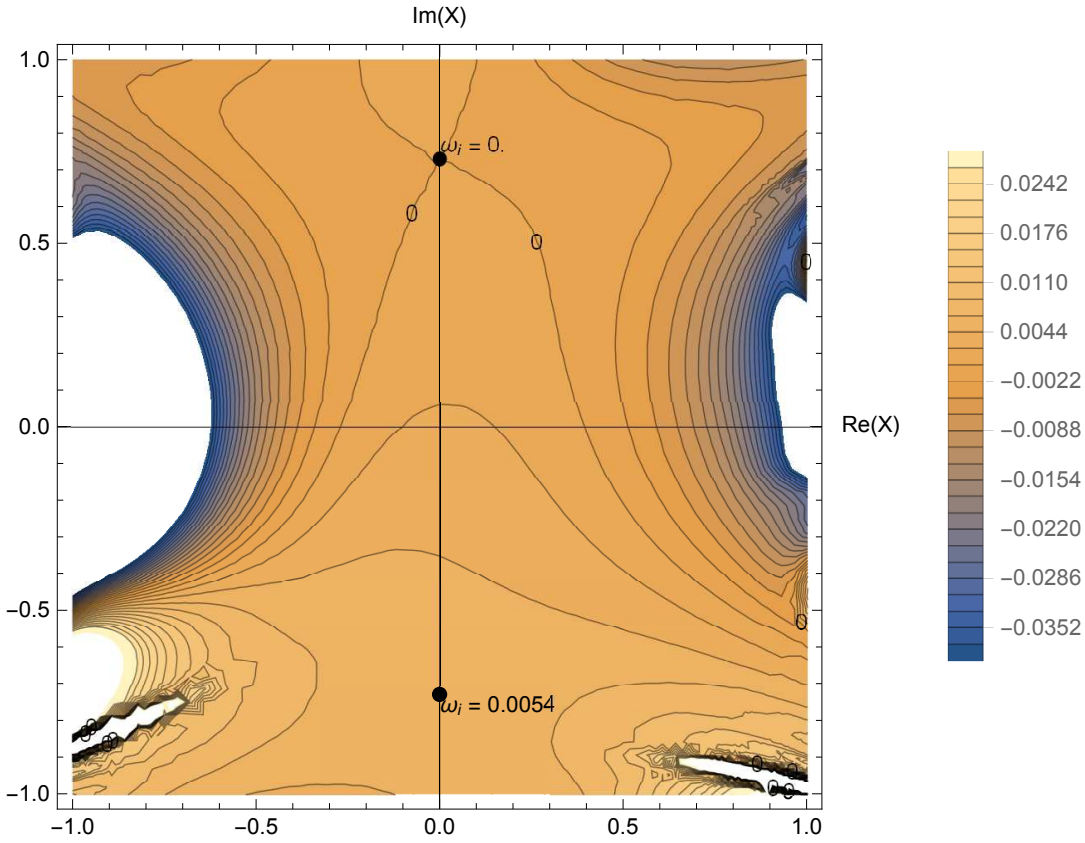

Figure 3.16: Global stability results, case iv) in table 3.2. Contour of constant Im(ω) at pinch points in the complex X plane for linearly varying bottom boundary with r_c given by (3.18), and with upper boundary placed at $h_1 = 5$. Im(ω) = 0 contours are labelled and the solid discs are the double saddle points satisfying (3.6).

upper half plane is considered, since we can not deform the integration path through the saddle point in the lower half plane as discussed previously.

In comparison of the results of the sea bed with both maxima and minima, and with the inflection point, for $h_1 = 10$ and $h_1 = 5$ we can see that the value of the globally unstable growth rate at the dominant double saddle is in each case increased by approximately 50% when $h_1 = 5$. Again this agrees well with the results of the absolute stability analysis shown in figure 2.17.

The most absolutely unstable parameter space occurs when $h_1 = 1$ and $h_2 = 2.5$, which was shown in figure 2.17. In our next section we will investigate the sloping sea bed around this parameter space.

3.4 Homogeneous problem of smooth velocity profile with $h_1 = 1$

The next examples we consider have upper boundary fixed at $h_1 = 1$ and we look at the linear sea bed, sea bed with maxima and minima, sea bed with inflection point and monotonically decreasing sea bed for which the results are presented in figures 3.17,3.18, 3.19 and 3.20 respectively. The considered model problems and results are given in table 3.3, which summarize the effect of model spatial variation of bottom boundary as discussed above.

Consider the uniformly sloping bed described by (3.14) with $h_1 = 1$, whose complex $X-$plane is shown in figure 3.17. The endpoints of the locally absolutely unstable region, $-0.735 < X < 0.998$ (or $1.765 < r_c(X) < 3.500$) , appear at the intersection of the $\mathrm{Im}(\omega) = 0$ contour with the real X axis. As discussed for the previous linearly sloping sea bed, there is no appearance of a double saddle satisfying (3.6) and therefore the problem with linearly varying sloping bottom boundary is not globally unstable despite the fact that in the region where $-0.735 < X < 0.998$ (or $1.765 < r_c(X) < 3.500$) it is absolutely unstable. On the other hand in comparison with the results for $h_1 = 10$ in figure 3.9 and for $h_1 = 5$ in figure 3.13 we can see the increase of the range of parameter space where absolute instability is present, which also agrees with the results of absolute stability analysis in figure 2.19. In fact $h_1 = 1$ has the largest range of parameters where absolute stability is present. For a sea bed

Parameters h_1 and r_c	Dominant mode of the problem	
	Frequency	Wavenumber
Case i) $r_c = X + 2.5$	globally stable	
Case ii) $r_c = X^3 - 0.5X + 2.5$	$\omega = 0.7222 + \text{i } 0.027$	$\alpha = 0.7381 - \text{i } 0.9867$
Case iii) $r_c = X^3 + 2.5$	$\omega = 0.7138 + \text{i } 0.028$	$\alpha = 0.7119 - \text{i } 0.9657$
Case iv) $r_c = X^3 + 1.595X + 2.5$	$\omega = 0.7069 + \text{i } 0$	$\alpha = 0.6255 - \text{i } 1.0607$

Table 3.3: Parameter regimes of model problems (as shown in figure 3.2) considered for global stability analysis. Velocity is given by (2.23) and density is constant. The variation is given by considering different functions for spatial variation of lower boundary $h_2 = r_c(X)h_1$, given by the function $r_c(X)$, where X is the slowly varying spatial variable. Upper boundary is placed at $h_1 = 1$.

with a maxima and minima, we consider (3.15) with $h_1 = 1$. The results are shown in figure 3.18 with two double saddles associated with the stationary values of $dr_c/dX = 0$ along the real X-axis, when $X = \pm(-r_1/3)^{1/2}$ in (3.8), i.e. at $X = \pm 0.408$.

For a sea bed with an inflection point we consider (3.16) with $h_1 = 1$ and the results for the complex X plane are shown in figure 3.19. Again, the double saddle condition (3.6) lies along the real X-axis. The results of absolute stability analysis shows that the over all maximum growth rate is when $h_1 = 1$ and $h_2 = 2.5$ which coincides with the inflection point of result in figure 3.19. Hence the maximum globally unstable growth rate we can create is presented in this result and the value of $\text{Im}(\omega) = 0.028$.

As r_1 becomes increasingly positive, the stationary point $dr_c/dX = 0$ moves

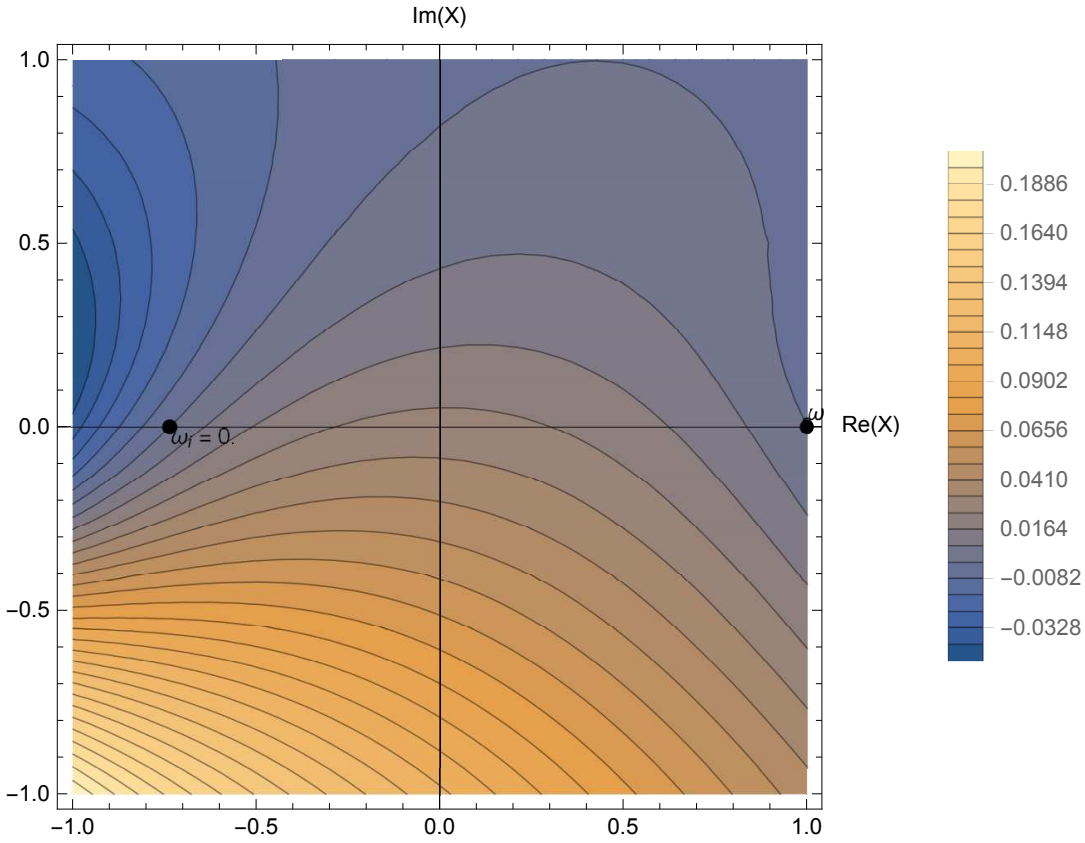

Figure 3.17: Global stability results, case i) in table 3.3. Contours of constant $\mathrm{Im}(\omega)$ at pinch points in the complex X plane for varying bottom boundary with r_c given by (3.14), and with upper boundary placed at $h_1 = 1$. $\mathrm{Im}(\omega) = 0$ contours are labelled and the solid discs are the intersections of the zero contour with the real X-axis at -0.735 and 0.998 respectively.

further from the real X axis, and $\mathrm{Im}(\omega)$ reduces. The largest positive value r_1 that supports global instability (for $h_1 = 1$) is found to be $r_1 = 1.655$, which leads to the following equation for r_c as follows,

$$r_c(X) = X^3 + 1.655X + 2.5. \tag{3.19}$$

Figure 3.20 shows the results for the largest positive value $r_1 = 1.655$ that supports global instability when the upper boundary is fixed at $h_1 = 1$. In the comparison

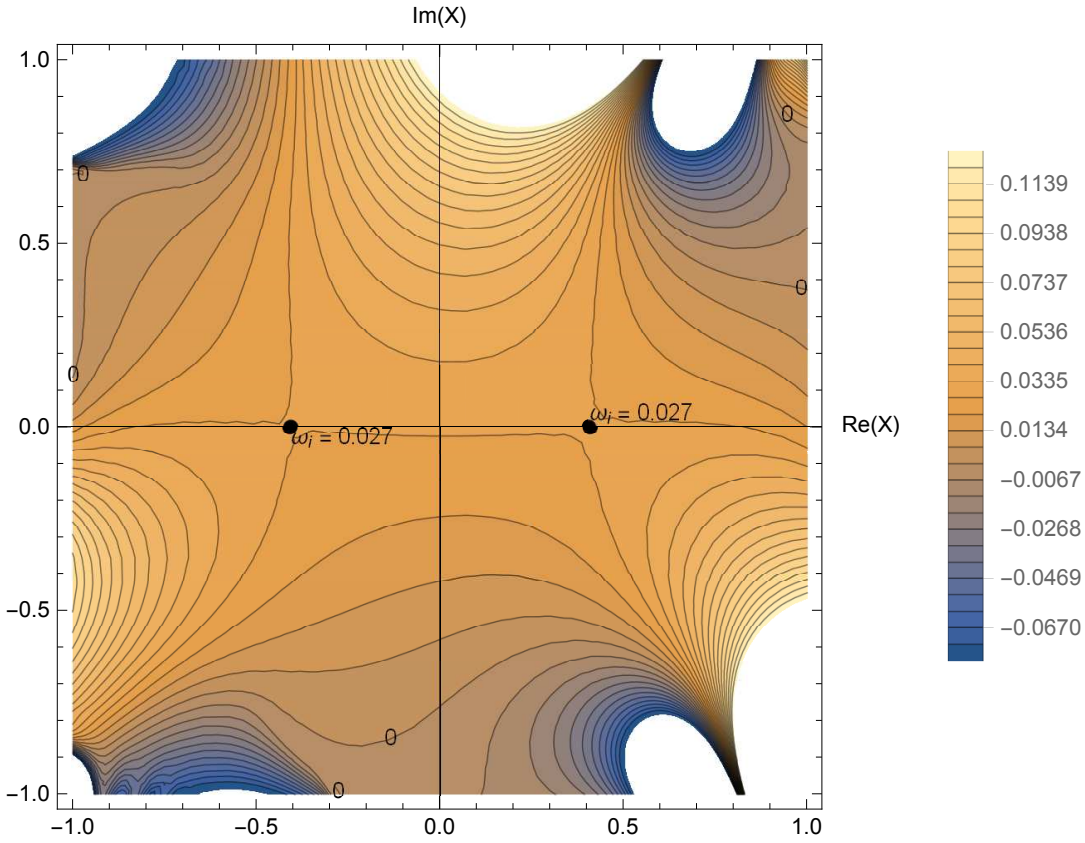

Figure 3.18: Global stability results, case ii) in table 3.3. Contours of constant $\mathrm{Im}(\omega)$ at pinch points in the complex X plane for varying bottom boundary with r_c given by (3.15), and with upper boundary placed at $h_1 = 1$. $\mathrm{Im}(\omega) = 0$ contours are labelled and the solid discs are the double saddle points satisfying (3.6), which occur at the stationary values $dr_c/dX = 0$ when $X = \pm(-r_1/3)^{1/2}$ in (3.8).

with the results of sea bed with both maxima and minima, and inflection point, for $h_1 = 10$ and $h_1 = 1$ we can see that the value of the globally unstable growth rate at the dominant double saddle is in each case increased approximately 14 times. Again this agrees well with the results of absolute stability analysis in figure 2.19.

Placing the boundaries closer to the velocity shear with $h_1 \leq 1$ has a stabilising effect and in fact when $h_1 \leq 0.75$ the flow is absolutely stable as shown in figure 2.17.

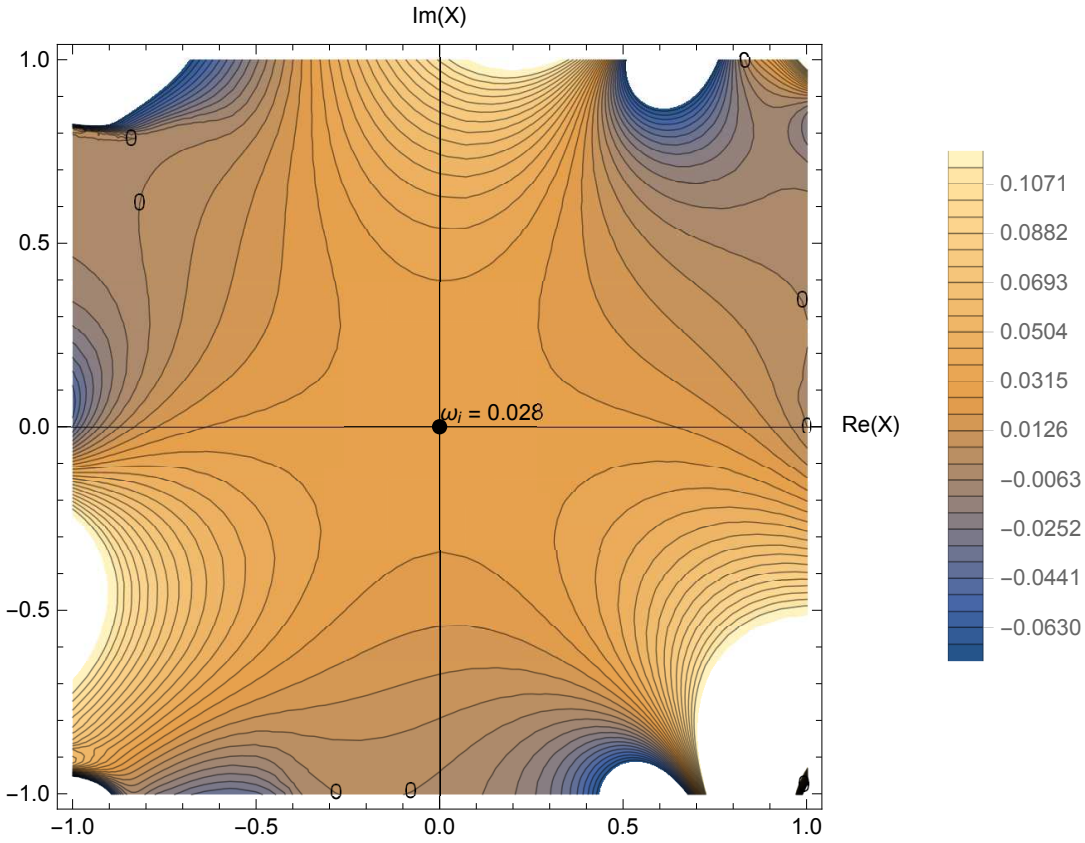

Figure 3.19: Global stability results, case iii) in table 3.3. Contours of constant $\mathrm{Im}(\omega)$ at pinch points in the complex X plane for linearly varying bottom boundary with r_c given by (3.16), and with upper boundary placed at $h_1 = 1$. $\mathrm{Im}(\omega) = 0$ contours are labelled and the solid disc is the double saddle points satisfying (3.6), which occur at the stationary value $dr_c/dX = 0$ when $X = 0$ in (3.8).

The last upper boundary we are considering here for our model problem is therefore $h_1 = 0.8$.

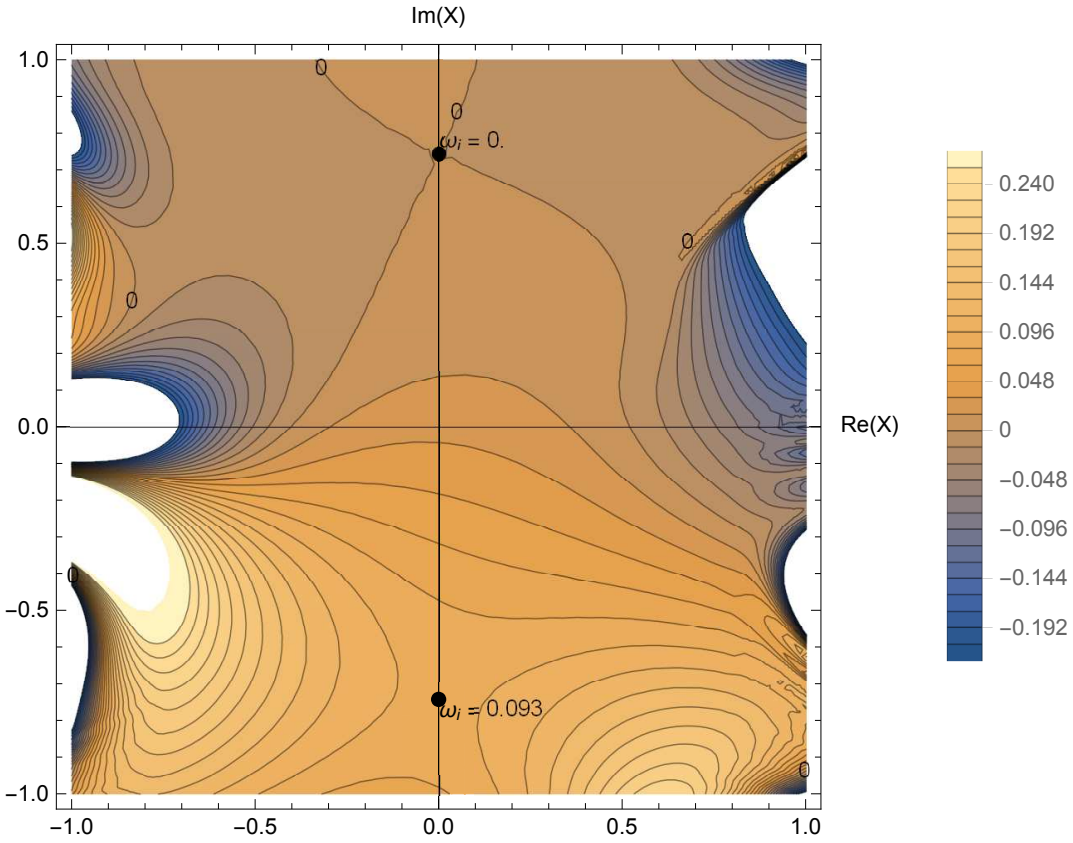

Figure 3.20: Global stability results, case iv) in table 3.3. Contours of constant $\mathrm{Im}(\omega)$ at pinch points in the complex X plane for linearly varying bottom boundary with r_c given by (3.19), and with upper boundary placed at $h_1 = 1$. $\mathrm{Im}(\omega) = 0$ contours are labelled and the solid discs are the double saddle points satisfying (3.6).

3.5 Homogeneous problem of smooth velocity profile with $h_1 = 0.8$

We consider a linear sea bed, sea bed with maxima and minima, sea bed with inflection point and a monotonically decreasing sea bed for which the results are presented in figures 3.21,3.22, 3.23 and 3.24 respectively. The considered model problems and results are given in table 3.4, which summarize the effect of model spatial variation of bottom

Parameters h_1 and r_c	Dominant mode of the problem	
	Frequency	Wavenumber
Case i) $r_c = X + 2.5$	globally stable	
Case ii) $r_c = X^3 - 0.5X + 2.5$	$\omega = 0.8251 + \text{i } 0.019$	$\alpha = 0.8929 - \text{i } 1.141$
Case iii) $r_c = X^3 + 2.5$	$\omega = 0.8334 + \text{i } 0.019$	$\alpha = 0.9413 - \text{i } 1.1712$
Case iv) $r_c = X^3 + 0.847X + 2.5$	$\omega = 0.8284 + \text{i } 0$	$\alpha = 0.8707 - \text{i } 1.23$

Table 3.4: Parameter regimes of model problems (as shown in figure 3.2) considered for global stability analysis. Velocity is given by (2.23) and density is constant. The variation is given by considering different functions for spatial variation of lower boundary $h_2 = r_c(X)h_1$, given by the function $r_c(X)$, where X is the slowly varying spatial variable. Upper boundary is placed at $h_1 = 0.8$.

boundary as discussed above.

For a linearly varying sea bed boundary we consider (3.14), and the results for $h_1 = 0.8$ are shown in figure 3.21. The endpoints of the locally absolutely unstable region, $-0.329 < X < 0.570$ (or $1.972 < r_c(X) < 3.412$) , appear as intersection of the $\text{Im}(\omega) = 0$ contour with the real X axis. As in the previous cases for a linearly sloping bed, there is no double saddle satisfying 3.6 and therefore the problem with linearly sloping bottom boundary is not globally unstable despite the fact that in the region where $-0.329 < X < 0.570$ (or $1.972 < r_c(X) < 3.412$) it is absolutely unstable. On the other hand in comparison with the results for $h_1 = 1$ in figure 3.17 we can see the decrease of the range of parameter space where absolute instability is present, which also agrees with the results of absolute stability analysis in figure 2.19. For a sea bed

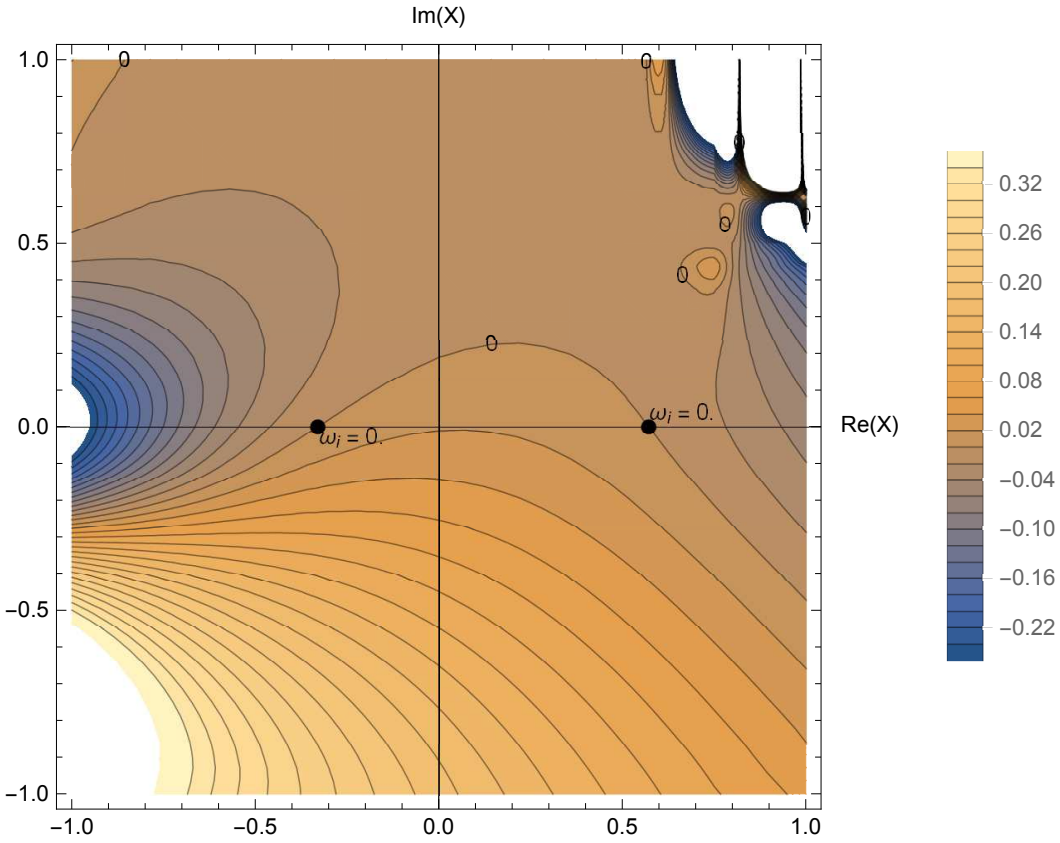

Figure 3.21: Global stability results, case i) in table 3.4. Contours of constant $\mathrm{Im}(\omega)$ at pinch points in the complex X plane for varying bottom boundary with r_c given by (3.14), and with upper boundary placed at $h_1 = 0.8$. $\mathrm{Im}(\omega) = 0$ contours are labelled and the solid discs are the intersections of the zero contour with the real X-axis at -0.329 and 0.570 respectively.

with both maxima and minima, we consider (3.15) for $h_1 = 0.8$ as shown in figure 3.22.

There two double saddles which are associated with stationary values of $dr_c/dX = 0$ along real X-axis, when $X = \pm(-r_1/3)^{1/2}$ in (3.8).

For a sea bed with an inflection point we consider (3.16) with $h_1 = 0.8$ and the complex X plane for this sea bed is shown in figure 3.23 As before, the double saddle condition (3.6) is satisfied at a value of X for sea bed profiles with maxima, minima or inflection point.

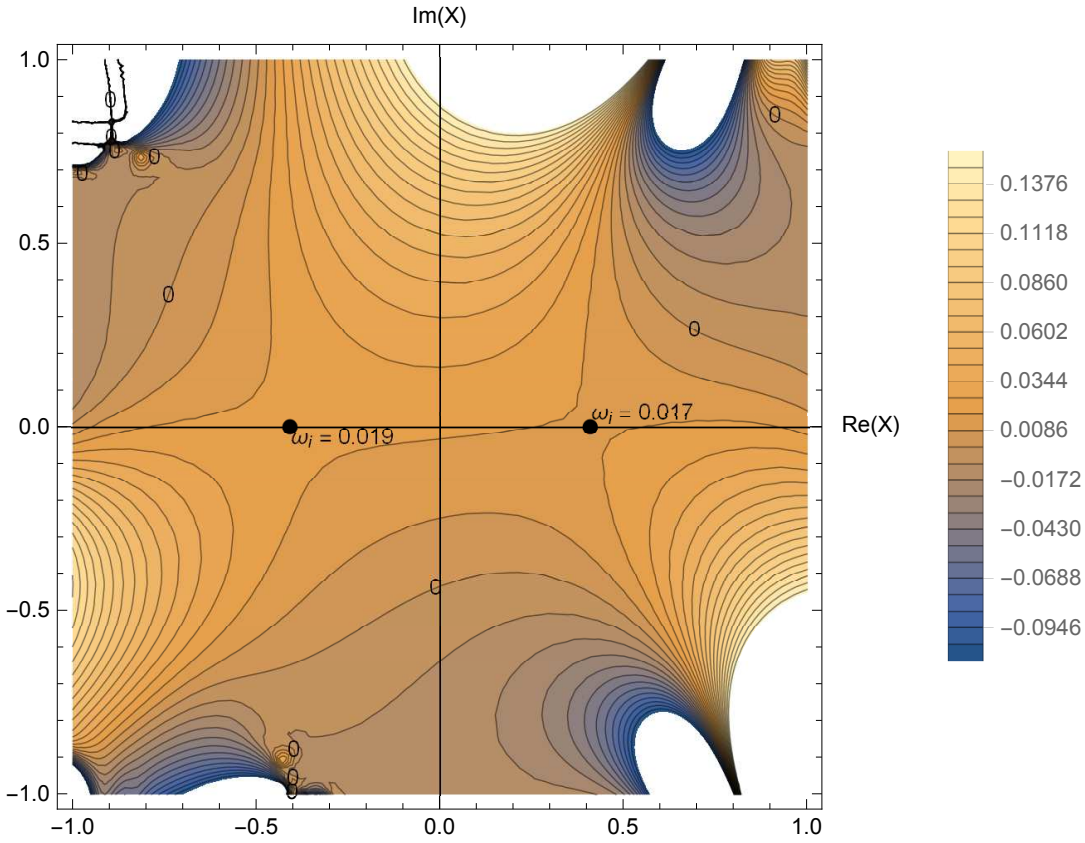

Figure 3.22: Global stability results, case ii) in table 3.4. Contours of constant $\mathrm{Im}(\omega)$ at pinch points in the complex X plane for varying bottom boundary with r_c given by (3.15), and with upper boundary placed at $h_1 = 0.8$. $\mathrm{Im}(\omega) = 0$ contours are labelled and the solid discs are the double saddle points satisfying (3.6), which occur at the stationary values $dr_c/dX = 0$ when $X = \pm(-r_1/3)^{1/2}$ in (3.8).

When r_1 becomes increasingly positive, the stationary point $dr_c/dX = 0$ moves further from the real X axis, and $\mathrm{Im}(\omega)$ reduces. The largest positive value r_1 that supports global instability (for $h_1 = 0.8$) is found to be $r_1 = 0.8475$, which leads to the following equation for r_c as follows,

$$r_c(X) = X^3 + 0.8475X + 2.5. \tag{3.20}$$

Figure 3.24 shows the results for the largest positive value $r_1 = 0.8475$ that

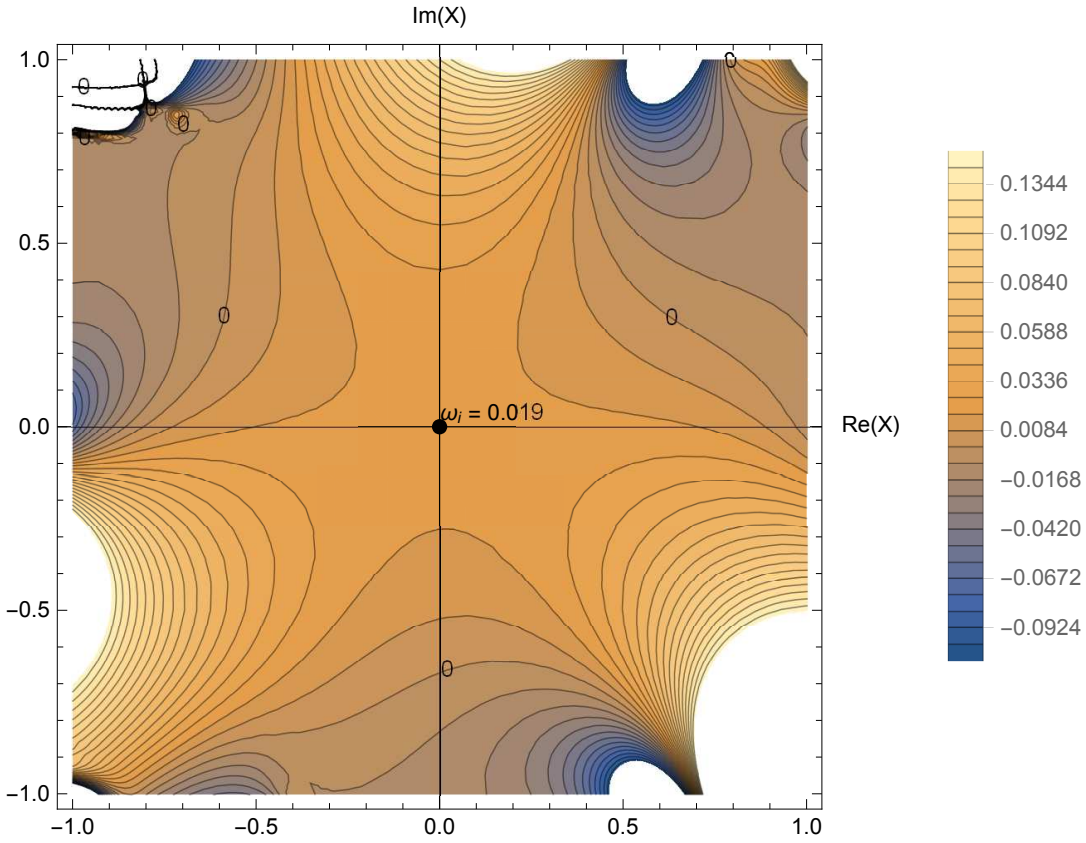

Figure 3.23: Global stability results, case iii) in table 3.4. Contours of constant $\mathrm{Im}(\omega)$ at pinch points in the complex X plane for varying bottom boundary with r_c given by (3.16), and with upper boundary placed at $h_1 = 0.8$. $\mathrm{Im}(\omega) = 0$ contours are labelled and the solid disc is the double saddle points satisfying (3.6), which occur at the stationary value $dr_c/dX = 0$ when $X = 0$ in (3.8).

supports global instability with the upper boundary fixed at $h_1 = 0.8$. There are two double saddles satisfying (3.6) in the results shown in figure 3.24, but only the one in the upper half plane is considered, since we can not deform the integration path trough the saddle point in the lower half plane as discussed previously.

Comparing the results of sea beds with maxima and minima, and with an inflection point, for $h_1 = 1$ and $h_1 = 0.8$ we can see that the value of the globally unstable

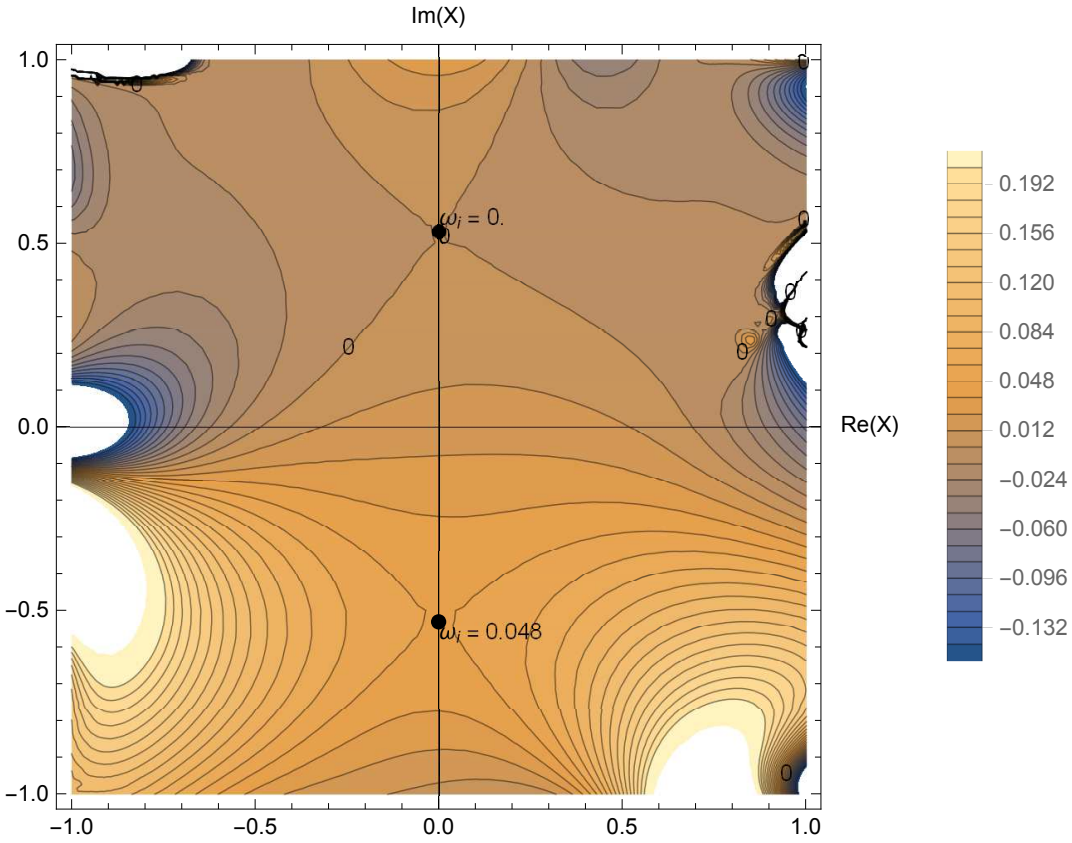

Figure 3.24: Global stability results, case iv) in table 3.4. Contours of constant $\mathrm{Im}(\omega)$ at pinch points in the complex X plane for varying bottom boundary with r_c given by (3.20), and with upper boundary placed at $h_1 = 0.8$. $\mathrm{Im}(\omega) = 0$ contours are labelled and the solid discs are the double saddle points satisfying (3.6).

growth rate at the dominant double saddle is in each case decreased by approximately 50%. Again this agrees well with the results of absolute stability analysis in figure 2.19.

Reducing further the distance of the upper boundary h_1 stabilises the problem and values of $h_1 \leq 0.75$ result in absolutely stable flow and therefore are not considered in our model examples.

Parameters J_0 and r_c	Dominant mode of the problem	
	Frequency	Wavenumber
Case i) $J_=0.01$ $r_c =$ $X^3 + 0.963X + 2.5$	$\omega = 0.7088 + \text{i } 0$	$\alpha = 0.6625 - \text{i } 1.0213$
Case ii) $J_0 = 0.02$ $r_c =$ $X^3 + 0.467X + 2.5$	$\omega = 0.7076 + \text{i } 0$	$\alpha = 0.688 - \text{i } 0.9843$
Case iii) $J_0 = 0.03$ $r_c =$ $X^3 + 2.5$	$\omega = 0.7064 - \text{i } 0.0037$	$\alpha = 0.7060 - \text{i } 0.9623$

Table 3.5: Parameter regimes of model problems (as shown in figure 3.2) considered for global stability analysis. Velocity and density profiles are given by (2.23) and (2.24) respectively. The variation is given by considering different functions for spatial variation of lower boundary $h_2 = r_c(X)h_1$, given by the function $r_c(X)$, where X is the slowly varying spatial variable. Upper boundary is placed at $h_1 = 1$. Considered stratification is for global Richardson number $J_0 = 0.01$, $J_0 = 0.02$ and $J_0 = 0.03$

3.6 Stratified problem of smooth velocity and density profiles with $h_1 = 1$

Adding stable stratification to the flow considered in our work has a stabilising effect on absolute stability, as shown in the absolute stability results in figure 2.19. Here we show that this effect is carried on into the global stability analysis and for model examples we consider the monotonic sloping sea bed in the same manner as in the homogeneous case but with global Richardson number $J_0 = 0.01, 0.02$ and 0.03 to see what is the largest positive value r_1 in (3.8) that supports global instability (for $h_1 = 1$) for stratified flow. The considered model problems and results are given in table 3.5, which summarize the effect of different stratification as discussed above.

The largest positive value r_1 that supports global instability for $h_1 = 1$ and

$J_0 = 0.01$ is found to be $r_1 = 0.963$, which leads to

$$r_c(X) = X^3 + 0.963X + 2.5. \tag{3.21}$$

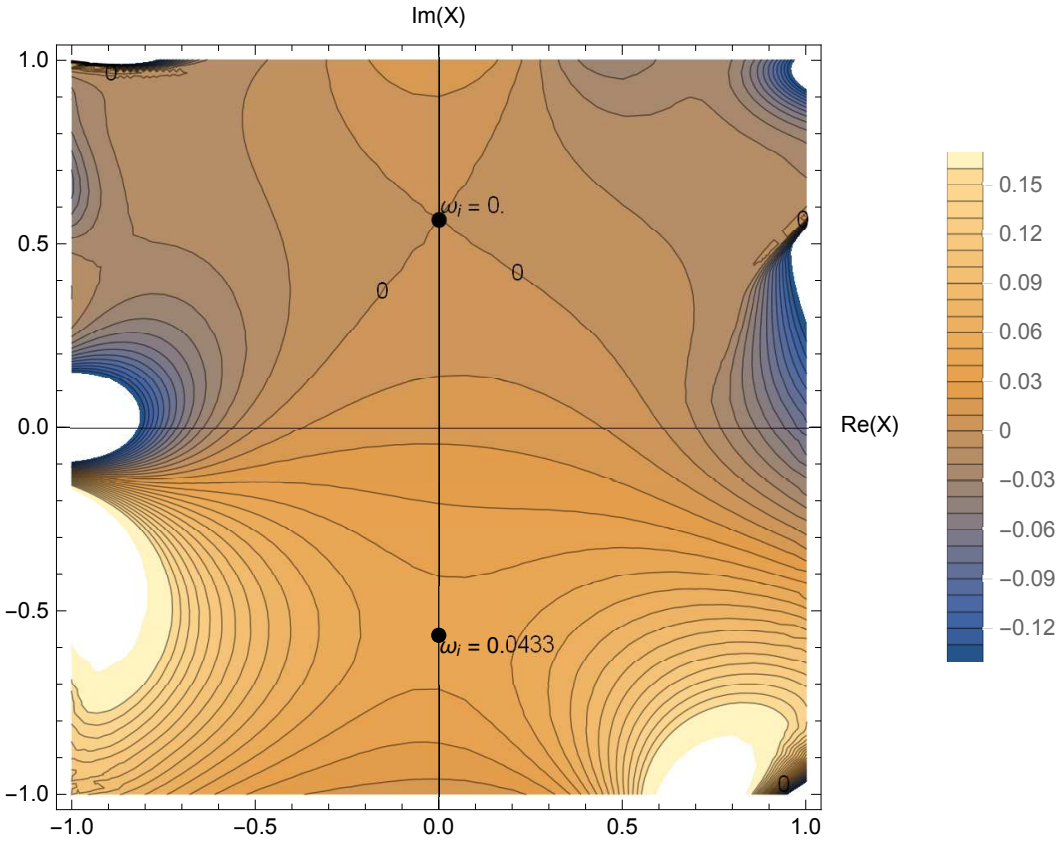

Figure 3.25: Global stability results, case i) in table 3.5. Contours of constant $\mathrm{Im}(\omega)$ at pinch points in the complex X plane for varying bottom boundary with r_c given by (3.21), and with upper boundary placed at $h_1 = 1$ and $J_0 = 0.01$. $\mathrm{Im}(\omega) = 0$ contours are labelled and the solid discs are the double saddle points satisfying (3.6).

Figure 3.25 shows the results for the largest positive value $r_1 = 0.963$ that supports global instability with upper boundary fixed at $h_1 = 1$ and $J_0 = 0.01$.

Comparison of the results with the homogeneous scenario in figure 3.20 shows the stabilising effect of stable stratification, but the results are still globally unstable.

If we increase the stratification further to $J_0 = 0.02$ the results are more stabilised, but the global instability still persists and the largest positive value r_1 that supports global instability for $h_1 = 1$ and $J_0 = 0.02$ is found to be $r_1 = 0.467$, i.e.

$$r_c(X) = X^3 + 0.467X + 2.5. \tag{3.22}$$

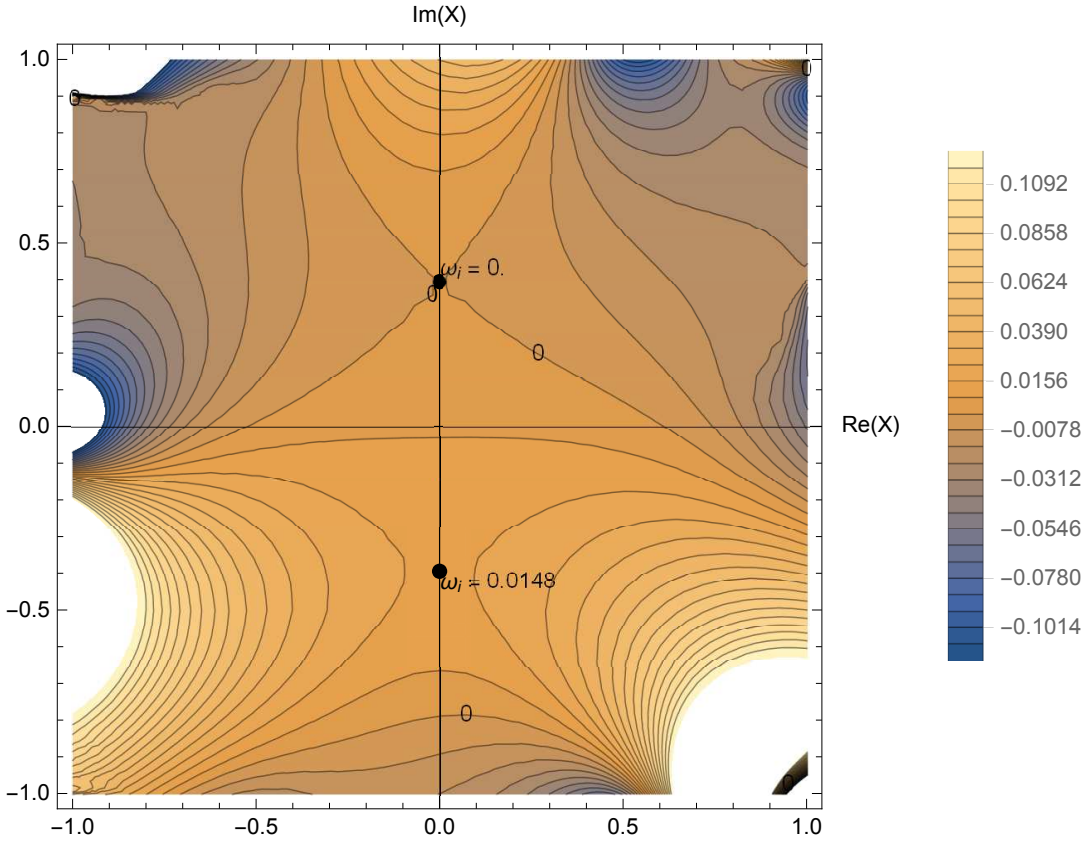

Figure 3.26: Global stability results, case ii) in table 3.5. Contour of constant $\mathrm{Im}(\omega)$ at pinch points in the complex X plane for varying bottom boundary with r_c given by (3.22), and with upper boundary placed at $h_1 = 1$ and $J_0 = 0.02$ $\mathrm{Im}(\omega) = 0$ contours are labelled and the solid discs are the double saddle points satisfying (3.6).

Figure 3.26 shows the results for the largest positive value $r_1 = 0.467$ that supports global instability with upper boundary fixed at $h_1 = 1$ and $J_0 = 0.02$. Increasing

the stable stratification further will stabilise the flow again and if we consider $J_0 = 0.03$ then the flow is absolutely stable as shown in figure 2.19. So despite the fact that the double saddles satisfying (3.6) are still present the value of $\mathrm{Im}(\omega) \leq 0$ and hence the flow is also globally stable. To illustrate this we consider sea bed with inflection point where (3.6) is always satisfied (as it is at maxima and minima) with $r_1 = 0$ in (3.8) i.e. (3.15), which leads to and fix the parameters to be $h_1 = 1, J_0 = 0.03$. The results are shown in figure 3.27. We can see from figure 3.27 that although the double saddle

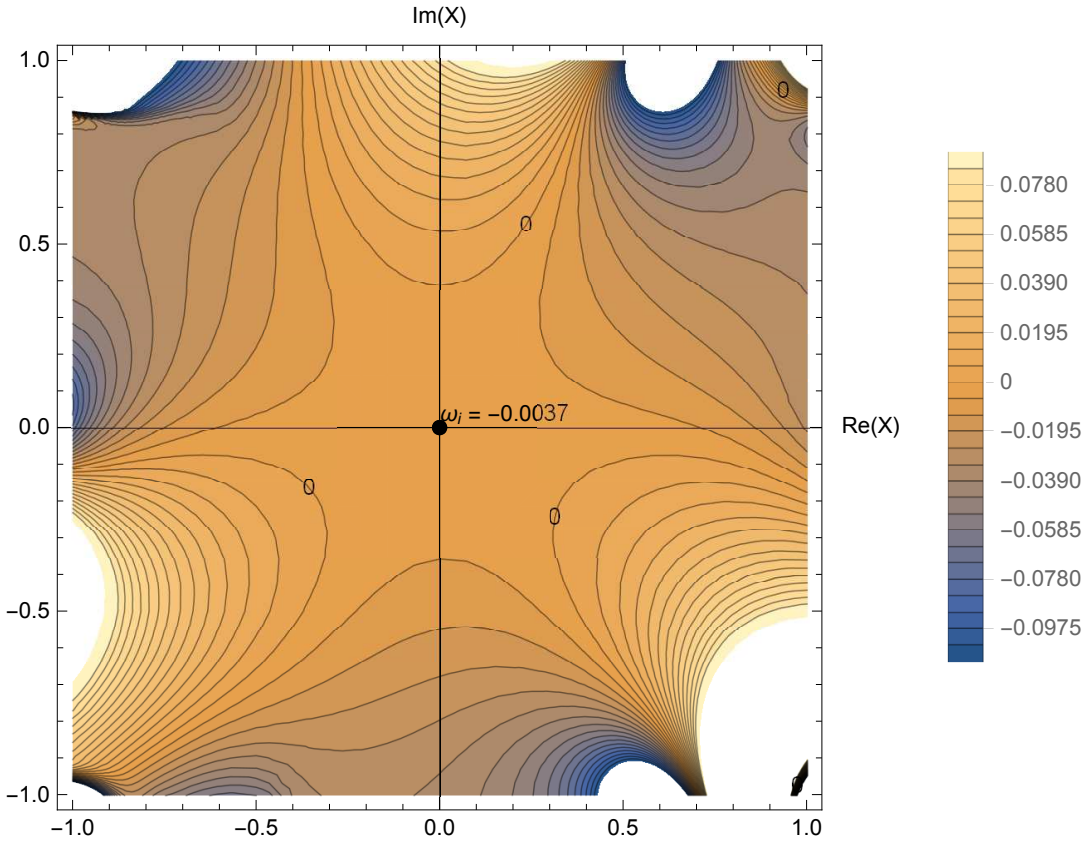

Figure 3.27: Global stability results, case iii) in table 3.5. Contour of constant $\mathrm{Im}(\omega)$ at pinch points in the complex X plane for varying bottom boundary with r_c given by (3.15), and with upper boundary placed at $h_1 = 1$ and $J_0 = 0.03$ $\mathrm{Im}(\omega) = 0$ contours are labelled and the solid discs are the double saddle points satisfying (3.6).

satisfying (3.6) is present the stable stratification is strong enough to stabilise the flow. Therefore there is no need to consider stronger stable stratification for our model as $J_0 \geq 0.025$ will result in absolutely stable flow.

3.7 Conclusion

We have shown here that having derived the parameter regime for which a flow is absolutely unstable we can extend the results to a global mode analysis and for given spatial variation of the problem (in our case variation of the bottom boundary depth) we can calculate global modes. This can be repeated for any variation of bottom boundary and it might well result in globally unstable flow if the parameter regime satisfies the conditions for absolute instability. We also show that there is the possibility of globally stable flow, even if it has locally absolutely unstable results, for example, the linearly sloping bottom boundary as shown in this chapter.

4 Stability of flows with vertically displaced density and velocity gradients

In many physical problems concerned with parallel stratified flow there may be regions of strong density gradient and strong shear that are at different heights. This occurs, for example, in the upper ocean where the upper layer is warmer and less salty compared to the lower layer which is colder and more salty. This results in a stable stratification due to salinity and temperature. If wind blows over the surface of the ocean it moves fluid in the upper part of the ocean creating a velocity shear. Hence we have a moving layer of fluid above stationary fluid (co-flow situation) with stable stratification. Often the maximum density gradient is of different thickness than the velocity shear and in addition the maximum density gradient might be displaced from the center of the strongest velocity shear. Similarly, such a situation can occur in the atmosphere.

In this chapter we consider the effects on absolute instability of different thickness of strongest density gradient compared to velocity shear, and also the effect of displacement of the strongest density gradient from the velocity shear. The velocity and density profiles that will be considered are shown in figure 4.1 with velocity and density profiles defined as follows:

$$U(z) = (1 + \tanh[5z])/2, \tag{4.1}$$

and

$$\bar{\rho}(z) = 1 - d\tanh(\gamma(z - \delta)), \tag{4.2}$$

where $d = \frac{\rho_b - \rho_u}{\rho_b + \rho_u}$ is the dimensionless density parameter and γ is a parameter for relative thickness of density to velocity, and δ is the parameter of displacement of density profile relative to velocity profile. We let global Richardson number $J_0 = 0.01$,

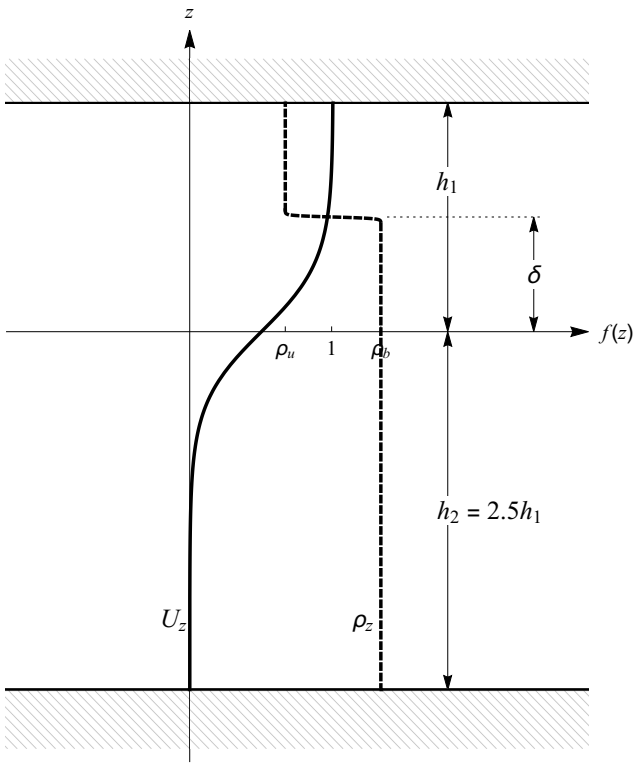

Figure 4.1: The velocity (solid black line) and density (dashed black line) profiles, (4.1), (4.2), for a case where the density interface is much smaller and displaced from the velocity profile by δ.

and consider first the case of no vertical displacement between the density and velocity profiles, $\delta = 0$, and we let $h_1 = 1$ and $r_c = 2.5$. Variation of the parameter γ, with $\delta = 0$, has been considered and the results can be simply stated as follows. When γ decreases from $\gamma = 5$ to $\gamma = 0$, the maximum growth rate of the absolute instability ω_i increases monotonically from $\omega_i = 0.01732$ towards the bounded homogeneous result, for which $\omega_i = 0.028$. When γ increases from $\gamma = 5$ to $\gamma = 100$, the maximum growth rate of the absolute instability ω_i decreases monotonically from $\omega_i = 0.01732$ towards $\omega_i = 0.01642$. These are results as expected because as $\gamma \to 0$ the effects of the density profile weaken because $\frac{\bar{\rho}'}{\bar{\rho}} \propto \gamma$ and the density only enters the problem via $\frac{\bar{\rho}'}{\bar{\rho}}$.

We now consider the effect of displacement of density and velocity profiles, keeping the relative thickness coefficient for the density profile to be $\gamma = 100$, which corresponds to the limit considered by Holmboe (see chapter 1). The layout of the problem is as shown in figure 4.1 with velocity profile (4.1) and density profile (4.2). The absolute stability result for this flow, with parameter parameter $\delta = -0.5$ is shown in figure 4.2.

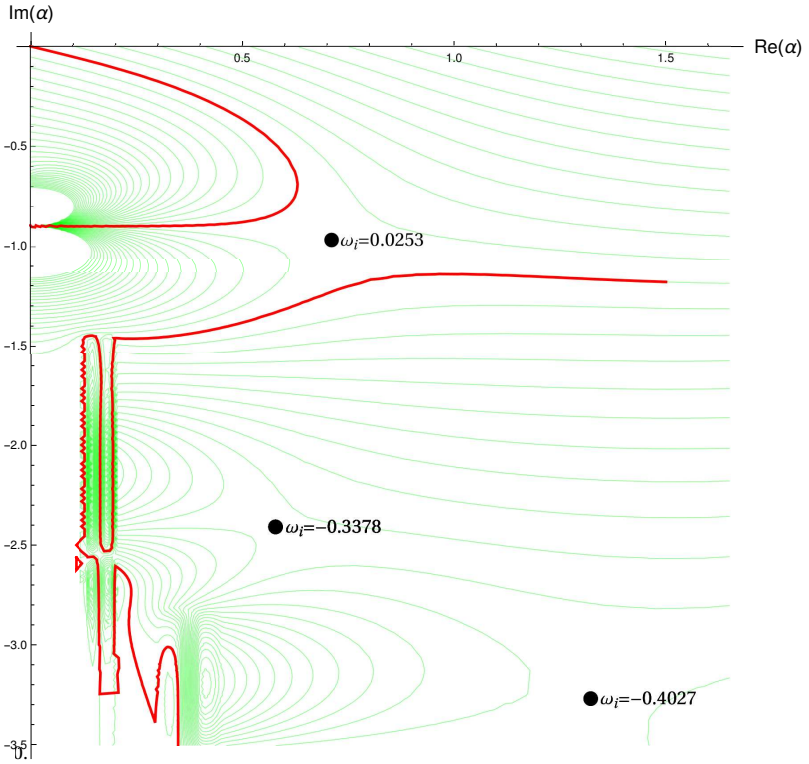

Figure 4.2: Absolute stability results. Contours of constant Im(ω) (green lines) in the complex α plane for solution to (1.17) with velocity and density profiles defined by (4.1) and (4.2), where $\delta = -0.5$. Saddles, where $\frac{\partial \omega}{\partial \alpha} = 0$, are marked as black discs with dominant saddle being the one closest to the origin. The contours Im(ω) = 0 are indicated with red lines.

Variation of δ results in different values of absolute instability growth rate ω_i,

wave number α and phase speed c. We present these quantities as a function of displacement δ in figures 4.3.

Although the variation of the quantities presented in figures 4.3 are relatively small, which is due to the small stratification ($J_0 = 0.01$), we can see in part (a) of figure 4.3 that there is a local maximum $\omega_i = 0.02947$ at $\delta = -1.4$. The counter intuitive result is that this maximum growth rate of bounded stably stratified co-flow is in fact greater than the same bounded co-flow without stratification. In other words we can destabilise the homogeneous bounded flow by introducing stable stratification, if the stratification has small density interface displaced below the velocity interface by $\delta = -1.4$. We want to understand the origins of this behaviour, and we will show that piecewise linear theory captures this effect, and can be used to explain it.

4.1 Piecewise linear approximation to flows with vertically displaced density and velocity gradients

For better understanding of the origins of the behaviour of results from the previous section and for comparison with the numerical result of the Taylor-Goldstein equation (1.18) for the problem shown in figure 4.1, for which the results are presented in figure 4.3, we use piecewise linear theory. Consider the layout of the problem as shown in figure 4.4. with

$$U(z) = \begin{cases} U_1 & : 0 \leq z \leq 1 \\ 0 & : -2.5 \leq z < 0 \end{cases} \tag{4.3}$$

and

$$\rho(z) = \begin{cases} \rho_{up} & : \delta \leq z \leq 1 \\ \rho_{bot} & : -2.5 \leq z < \delta \end{cases} \tag{4.4}$$

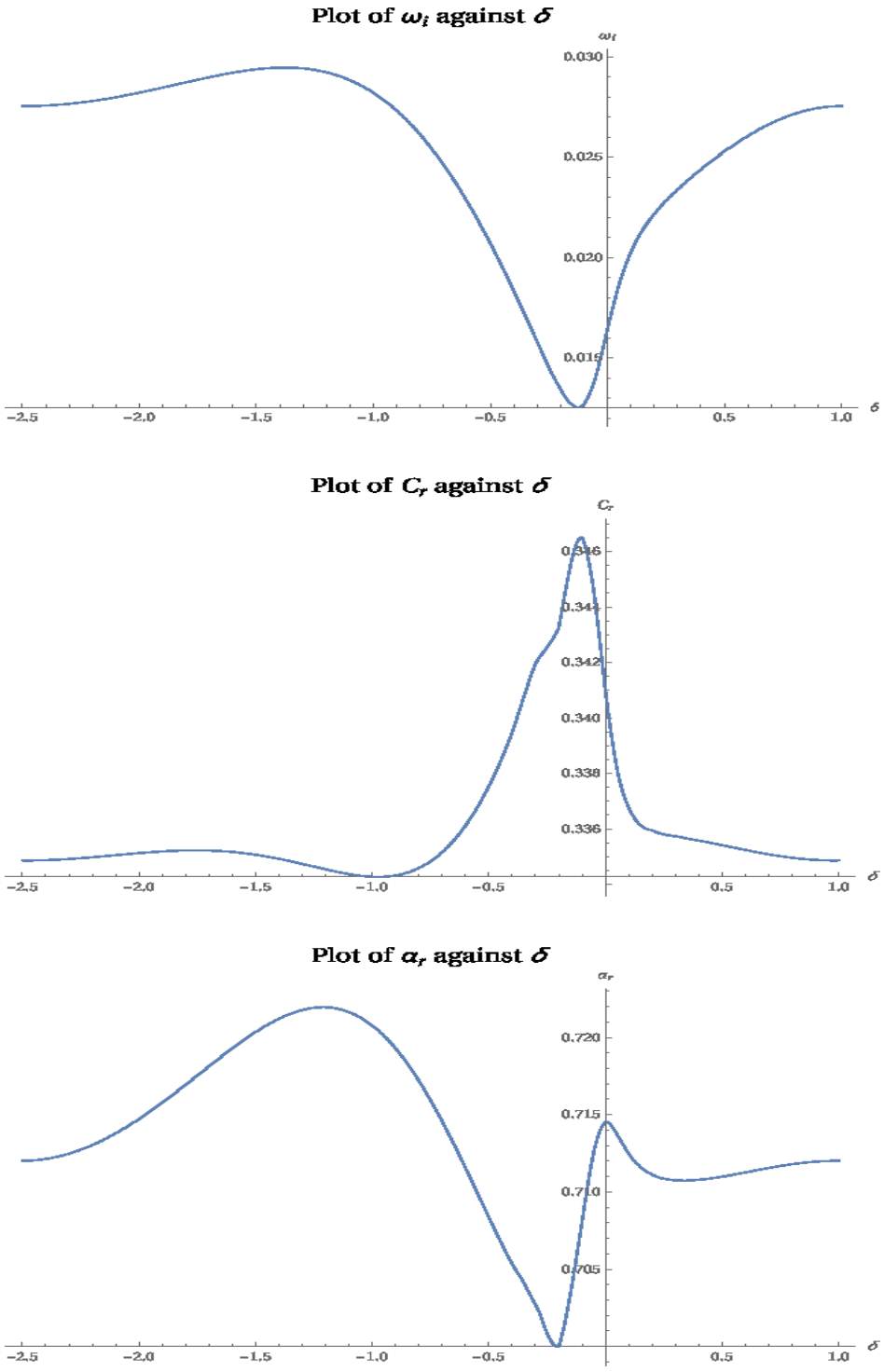

Figure 4.3: Absolute stability results. Top result shows the variation of the growth rate $\mathrm{Im}(\omega)$, at the saddle where $\frac{\partial \omega}{\partial \alpha} = 0$, as a function of displacement of density and velocity profiles δ. Middle result shows the variation of the phase speed c_r, at the saddle, as a function δ. Bottom result shows the variation of the wavenumber α_r, at the saddle, as a function δ.

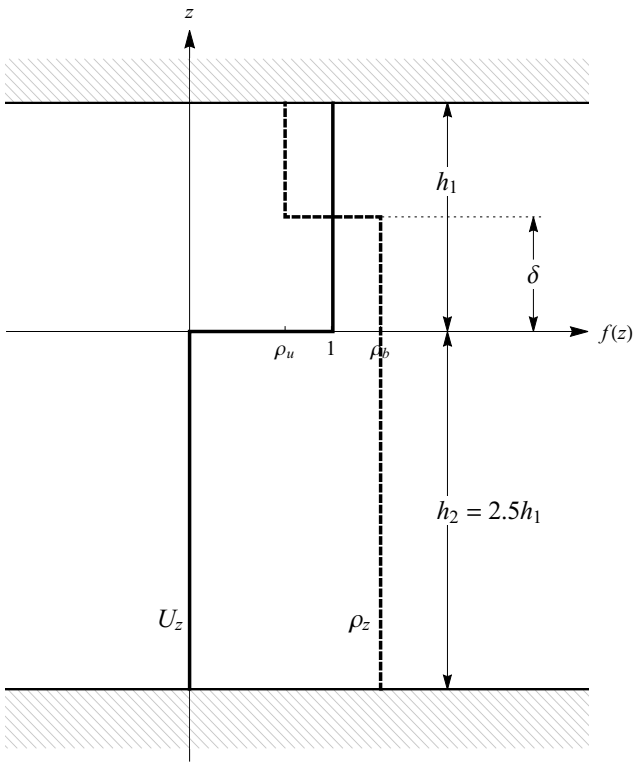

Figure 4.4: The piecewise linear velocity (solid black line) and density (dashed black line) profiles, where the density interface is displaced from velocity by δ.

Using the jump conditions (1.33) and (1.34) the following dispersion relations are obtained:

$$\begin{aligned}\cosh(\alpha)\left(\alpha J_0\omega^2-(\alpha-\omega)^4\tanh\left(\frac{5}{2}\alpha\right)\right)\\ +\cosh(\alpha-2\alpha\delta)\left(-\alpha J_0\omega^2\right)+(\alpha-\omega)^2\left(-\omega^2\sinh(\alpha)\right)\\ +(\alpha-\omega)^2\left(\alpha J_0(\sinh(\alpha)+\sinh(\alpha-2\alpha\delta))\tanh\left(\frac{5}{2}\alpha\right)\right)=0\end{aligned} \tag{4.5}$$

for $0 \leq \delta \leq 1$, and

$$-\omega^2 \cosh\left(\alpha\left(\frac{5}{2}-\delta\right)\right)\left((\alpha-\omega)^2\sinh(\alpha\delta)+\omega^2\cosh(\alpha\delta)\tanh(\alpha)\right)$$
$$+\sinh\left(\alpha\left(\frac{5}{2}-\delta\right)\right)\left(\omega^2\cosh(\alpha\delta)\left(-(\alpha-\omega)^2+2\alpha J_0\tanh(\alpha)\right)\right)$$
$$+\sinh\left(\alpha\left(\frac{5}{2}-\delta\right)\right)\left(\sinh(\alpha\delta)\left(2\alpha J_0(\alpha-\omega)^2-\omega^4\tanh(\alpha)\right)\right)=0, \qquad (4.6)$$

when $-2.5 \leq \delta \leq 0$, where $J_0 = dgL/V_1^2$ is the global Richardson number. For comparison with the numerical result we fix $J_0 = 0.01$. The result of this piecewise linear theory is shown in figure 4.5. This result is in good qualitative agreement with

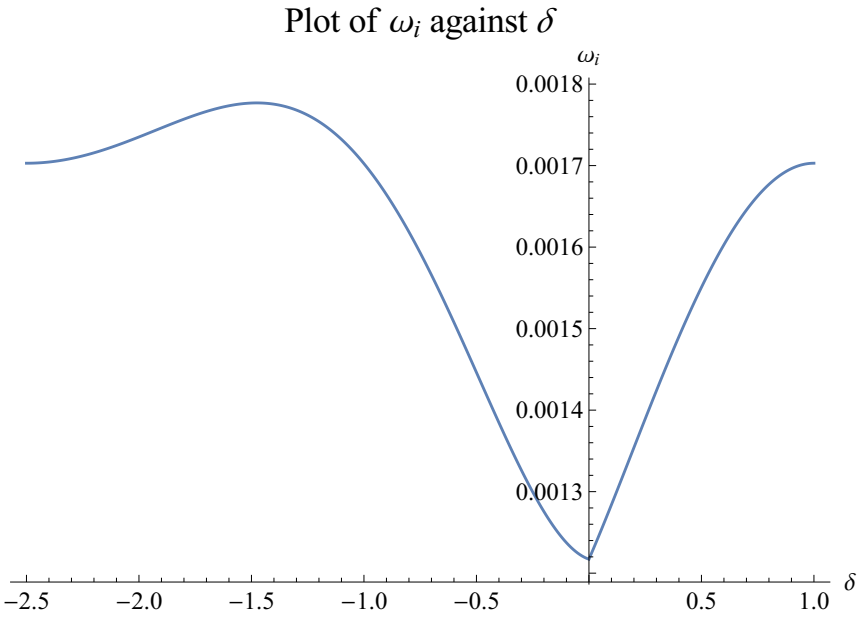

Figure 4.5: Absolute stability results. The growth rate ω_i as a function of displacement δ for the problem described in figure 4.4.

the numerical solutions presented in figure 4.3 and we clearly see the maximum growth rate ω_i when $\delta \approx -1.4$.

In chapter 2 we discussed how adding boundaries to homogeneous flow results in singularities along the imaginary $\alpha-$axis, where the positions of those can be derived

purely from satisfying boundary conditions in Taylor-Goldstein equation 1.18. We have also shown that those singularities may have, in the right parameter space, a destabilising effect on the flow. This brings us to the idea that a similar mechanism is produced by introducing the stratification to homogeneous problem.

Here we may use the piecewise linear theory, since it will result in a dispersion relation in polynomial form, which is easier to analyse in the complex $\alpha-$plane.

To avoid the singularities along the imaginary $\alpha-$axis produced by boundaries we consider unbounded problem with focus on the stratification. Therefore we consider the piecewise liner problem as shown in figure 4.4, but without the boundaries with velocity profile

$$U(z) = \begin{cases} U_1 & : z \geq 0 \\ 0 & : z < 0 \end{cases} \tag{4.7}$$

and density profile

$$\rho(z) = \begin{cases} \rho_{up} & : z \geq \delta \\ \rho_{bot} & : z < \delta \end{cases} \tag{4.8}$$

For convenience we also assume that $\delta < 0$. With the use of the standard techniques for deriving dispersion relations for piecewise linear profiles (see for example Drazin and Reid [6]), we get the dispersion relation.

$$-e^{2\alpha}(\alpha J_0 - \omega^2)(\alpha^2 - 2\alpha\omega + 2\omega^2) + \alpha(\alpha - 2\omega)(\alpha J_0) = 0. \tag{4.9}$$

If this dispersion relation has a pole at some finite value of $\alpha = \alpha_p$, then $\omega \to \infty$ as $\alpha \to \alpha_p$. When $\omega \to \infty$, (4.9) is dominated by the ω^4 term, and therefore, at pole, the coefficient of ω^4 must be zero. The coefficient of ω^4 in (4.9) is

$$-2\mathrm{e}^{2\alpha} \tag{4.10}$$

which is not zero for any finite α, and therefore (4.9) has no poles. Nonetheless, it does contain, saddle points near the imaginary $\alpha-$axis. We present the solution for

the growth rate Im(ω)in the complex $\alpha-$plane. We fix $J_0 = 0.01$ for which the result is shown in figure 4.6. There is a clear appearance of a saddle point which is created by

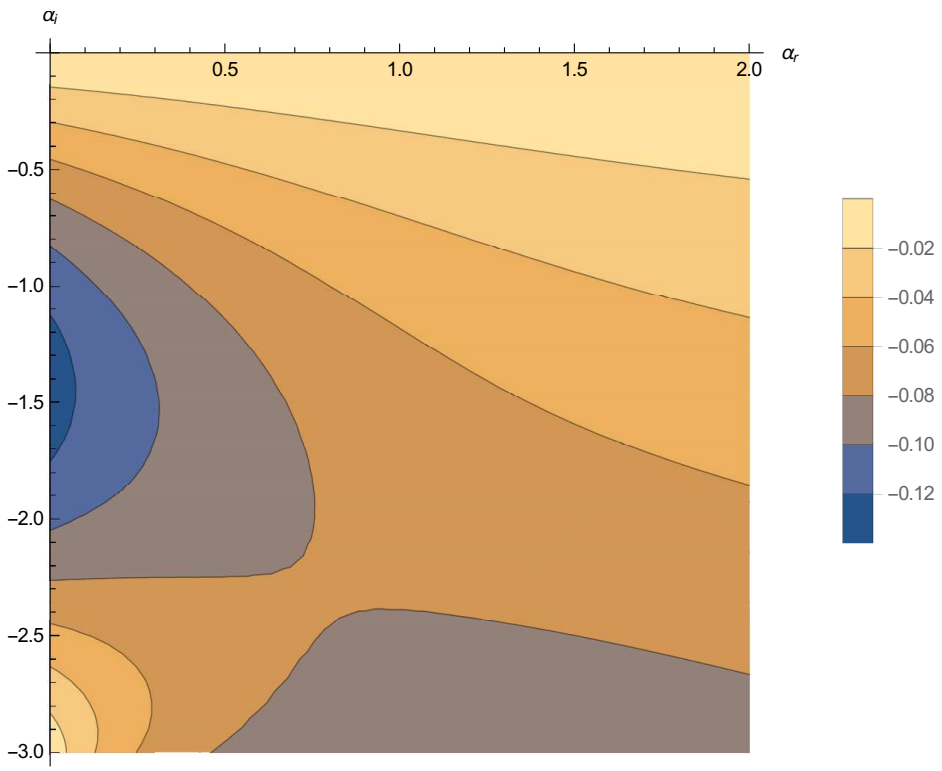

Figure 4.6: Absolute stability results. Growth rate Im(ω) in complex wavenumer plane given by dispersion relation (4.9) with global Richardson number $J_0 = 0.01$.

stratification in the problem, when compared with the homogeneous problem shown in figure 4.7, for which there is no saddle point.

In fact there are infinitely many new saddles in stratified problem which is more apparent in the figure 4.8 where we extend the range of the imaginary wavenumber.

Hence introducing stratification into a homogeneous unbounded problem results in new saddles appearing along the imaginary $\alpha-$ axis, where in the unbounded problem the values of the growth rate Im(ω) < 0 at those saddles and hence the problem

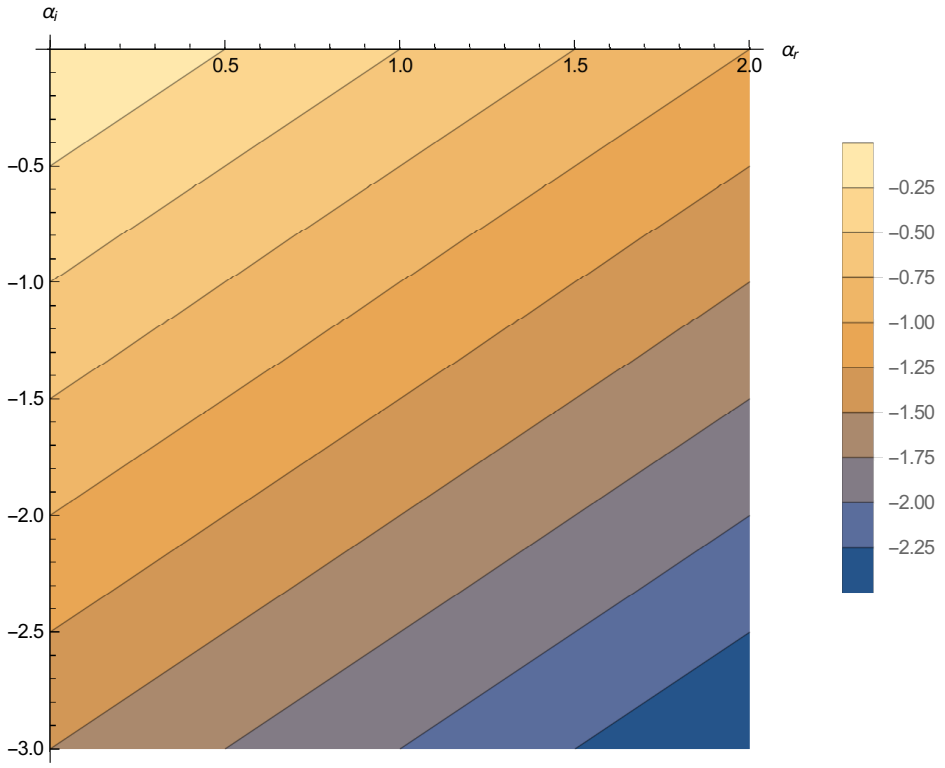

Figure 4.7: Absolute stability results. Growth rate $\mathrm{Im}(\omega)$ in complex wavenumer plane given by dispersion relation (4.9) for homogeneous case ($J_0 = 0$).

is absolutely stable. However, as shown at the beginning of this chapter, when considering a bounded stratified flow there are poles along the imaginary $\alpha-$axis due to the boundaries, and these might be destabilised by introducing the stable stratification in homogeneous problem. This is due to the deformation of the Riemann surface of the homogeneous solution by stratification.

4.2 Conclusion

In the main body of this thesis we considered flows where the density and velocity profiles are of the same thickness and the position of the maximum velocity gradient and

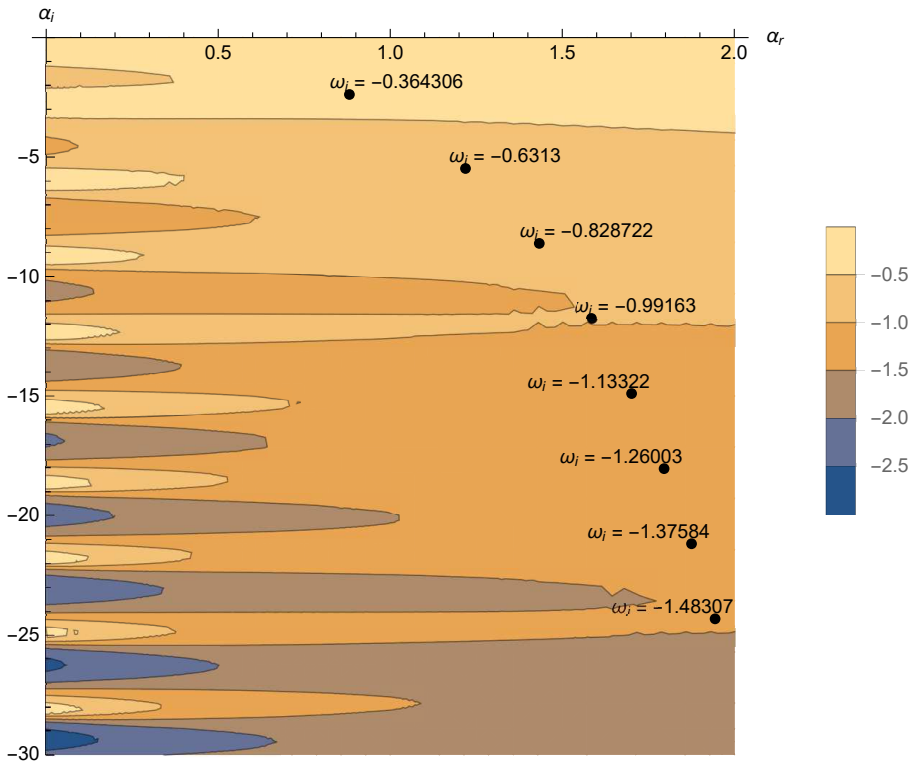

Figure 4.8: Absolute stability results. Growth rate $\mathrm{Im}(\omega)$ in complex wavenumer plane given by dispersion relation (4.9) with global Richardson number $J_0 = 0.01$. The black disks are the saddle points created by introduction of density to homogeneous problem.

maximum density gradient coincide, which often occurs in practice, and this provided a good starting point for our investigation. However, other configurations are possible. In this chapter we have investigated the effects of allowing the profile thicknesses to differ from one another, and also the effects of vertical displacement between the profiles have been studied. The inclusion of additional dimensionless parameters characterizing these modifications to the basic flow inevitably means that we cannot carry out full parameter search. Nonetheless, some new qualitative effects have been found. We investigate the effect of change of relative thickness of the density and velocity profiles,

and find that when the density layer is thinner than the shear layer, the absolute growth rate of absolutely unstable modes decreases, and in the limit of the thickness of the density layer tending to zero, while keeping the thickness of the velocity profile constant, the absolute absolute growth rate decrease from $\omega_i = 0.01732$ to $\omega_i = 0.01642$. The case of increasing the thickness of the strongest density gradient, the absolute growth rate increases monotonically from $\omega_i = 0.01732$ to $\omega_i = 0.028$, which is the absolute growth rate of homogeneous problem with without stratification.

In addition we show here for bounded flows, that if the density layer is much thinner then the shear layer, and displaced vertically downwards with respect to the position of the shear layer, it has a destabilising effect. In fact the destabilisation effect, when the maximum density gradient is at certain position below the maximum velocity gradient ($\delta = -1.4$ in above chapter) is strong enough to produce absolute growth rates which are greater than those of homogeneous flow in same parameter configuration. In other words by introducing stable density stratification into homogeneous flow such that the thickness of the density profile is much thinner than the thickness of the velocity profile, and the density gradient lies below the shear layer, the flow can be more absolutely unstable than the homogeneous case.

5 Conclusions and future work

5.1 Conclusions

In this work we have considered the stability properties of sheared stratified fluid flow. Such flows often arise in coastal oceans where wind stresses on the ocean surface create an upper layer of fluid moving across an essentially stationary lower layer. The main focus of this work has involved the use of linear stability analysis for absolute and global instability of parallel and weakly non-parallel flows, neglecting the effect of viscosity and molecular diffusion.

In the first chapter we introduce the hydrodynamic stability theory which reflects the typical upper ocean scenario, and survey the mathematical techniques used to analyse instabilities. The stability of parallel or weakly non-parallel flows modelling the flows in the upper oceans or atmosphere has been studied extensively since the times of Kelvin and Helmholtz. Despite this long history it is still typical for instability to be considered from purely temporal or spatial standpoint. For example, a temporal investigation describes the local growth of normal modes only in time, and hence we do not know how the disturbance will grow or decay in space (similarly spatial stability analysis does not tell us about growth in time). Therefore the concept of absolute stability is introduced, for parallel flows, which allows for investigation of absolutely unstable growths. If the flow is absolutely unstable we will observe the disturbances growing in the fixed frame of reference, i.e. in time and space simultaneously. We also consider weakly non-parallel flows which introduces spatial variation (in our case bottom boundary distance) of our investigated problems from the global stability analysis. If the flow is globally unstable, then the original velocity and density profiles

will be destroyed in our fixed frame of reference with the potential of creating a wave maker region. It is expected that global instability in the flow will greatly enhance mixing, and therefore is of great interest to oceanographers and climatologists. With the use of normal mode analysis we model parallel stratified flow with the use of the Taylor-Goldstein equation and discuss the techniques for calculating unstable growth rates. We also review the use of piecewise-linear techniques described in the works of Kelvin 1871 [1], Taylor 1931 [14], Holmboe 1962 [15] and Caulfield 1993 [16], which we use for comparison to some of our results. Description of numerical solutions to an eigenvalue problem is also introduced in first chapter.

In chapter 2 we review the methods for obtaining the absolute stability results following Briggs method (see Briggs 1964 [18]) and the work of Huerre and Monkewitz 1985 [19], which are essential to our absolute stability calculations. Many previous parallel flow investigations assumed an unbounded flow domain with the justification that the boundaries are far enough to be neglected. However, Healey 2009 [22] showed that adding boundaries to homogeneous flow at particular distances can have a destabilizing effect, and that this could be strong enough to create absolute instability even when one layer of fluid is moving above essentially stationary flow (co-flow situation). This result was of primary interest, because such scenario is common in geophysical flows in oceans and atmosphere. Since stratification is often important in such cases a relevant question is how density gradients affect the absolute instability. Here we obtain the parameter space for a bounded co-flow with stable stratification for which the flow is absolutely unstable, where the parameters are the distance of the upper and bottom boundaries from the interface as well as the strength of the stable stratification. We show that if the bottom boundary is placed 2.5 times further, from maximum velocity and density gradient, than the upper boundary, the absolute instability of the flow is

supported for stratification given by global Richardson number $J_0 \approx 0.025$ which is typical in upper ocean.

In chapter 3 we consider weakly spatially varying flows, where the spatial variation is produced by the bottom boundary of the problem (i.e. the sea bed of the ocean). In chapter 2 we have shown that for a fixed distance of the upper boundary there is a range of bottom boundary distance where absolute instability is present, for example in the homogeneous co-flow situation if the upper boundary is placed at $h_1 = 1$ then absolute instability is present for bottom boundary distances $1.765 < h_2 < 3.500$. This means that in near shore sea regions where the wind induced movement of an upper layer above essentially stationary fluid creates a co-flow situation, there will be created regions of absolute instability parallel to the shore. This is a situation which may support global instability. Therefore we investigate the effect of variations of bottom boundary (linearly sloping boundary, boundary with maxima, minima, inflection point and monotonically decreasing boundary) to see if they can support a global instability. We present examples of spatially varying bottom boundaries which result in globally unstable flow, and also examples where there is absolute instability present, but the flow is globally stable.

In chapter 4 we consider the scenario where the thickness of the density profile is not the same as the thickness of the velocity profile, and further allow for the different relative vertical positions of the profiles. This might be the situation where the strongest velocity gradient, induced by the wind flow above the ocean surface, and the density stratification of the ocean is given by a thermocline, which has its strongest density gradient in a different position to that of its strongest velocity gradient. We show that introducing stable stratification in the homogeneous problem results in saddles for the growth rate ω_i in the complex $\alpha-$plane (where α is the wavenumber). We

conclude, as expected, that if the thickness of the density profile is greater than that of the velocity profile, then it has destabilising effect on the absolute instability. This is a result of density gradients becoming weaker and the situation approaches that of homogeneous flow, which is expected to be more unstable than stably stratified flow. On the other hand, when the thickness of the density profile is smaller than that of the velocity profile, it has stabilizing effect on absolute instability of the flow. Further we investigate the effect of displacement of the maximum gradient of the density from the maximum gradient of velocity, where the density profile is 20 times thinner than the velocity profile, and obtain the absolute growth rates as a function of the relative displacement. The interesting result of this investigation is that there is a maximum absolute growth rate when the displacement of the maximum density gradient is 1.4 below the maximum velocity gradient, and in fact this growth rate is greater than for the same flow without stratification. In summary we show, under certain parameter regime, that we can destabilise homogeneous flow by adding stable stratification.

5.2 Future work

The research results described in this thesis suggest a number of further lines of investigation that could be undertaken.

One of the biggest assumptions in this work is that we are considering inviscid, non-diffusive flows, and in the real world fluids are viscous and diffusive. The next step therefore would be to relax this assumption and find ranges of Reynolds number (and Prandtl or Schmidt number) for which our proposed theory will be still applicable.

The next obvious extension of this work would be full non-linear analysis with the use of Direct Numerical Simulations (DNS). In fact having discovered the basic

behaviour and the interesting parameter regimes where global and absolute instabilities are present, we are looking to investigate the problem using DNS in collaboration with newly appointed colleague at Keele University, Dr Dan Lucas, to investigate this phenomena in more realistic flows with fewer approximations. We propose to use the DIABLO DNS suite (see Taylor 2008 [45]) which has been widely used to study various phenomena in stratified, shear driven turbulence. Some care will be required when the various instabilities are in competition to diagnose the appropriate signature of each.

In addition we could relax the rigid lid boundary condition at the surface and consider interaction with surface waves, which we have assumed to be much faster than the growth of our instabilities. Also three-dimensional analysis should be considered in the future, which will be relevant in river plumes, where the thickness of the river entering the ocean is finite and so horizontal shear may become important.

There are many possibilities for parameters to be explored in our scenarios, especially in chapter 4, where only a few cases have been considered. It would also be interesting to obtain velocity and density profiles from experiments which we may use in our analysis and which may or may not confirm the relevance of the theoretical mechanism proposed here. A relevant question may be if it is possible to maintain the required profiles over long enough timescales in order to be able to observe the growth of the instabilities discovered here.

A Matching conditions for stratified flows

Recall that the linearised equations for a 2−dimensional stratified flow are equations of momentum, continuity and incompressibility as stated below

$$i\alpha\bar{\rho}\big(U-c\big)u+\bar{\rho}U'w=-i\alpha p \tag{A.1}$$

$$i\alpha\bar{\rho}(U-c)w=-p'-F^{-2}\hat{\rho} \tag{A.2}$$

$$i\alpha u+w'=0 \tag{A.3}$$

$$i\alpha(U-c)\hat{\rho}+\bar{\rho}'w=0 \tag{A.4}$$

as derived in section 1.1.1, where $\bar{\rho}=\bar{\rho}(z)$ is the basic density profile, $\hat{\rho}=\hat{\rho}(z)$ is the disturbance to density field and F is Froude number.

To obtain the first matching condition we eliminate u from (A.3) and rewrite equation of momentum (A.1) as

$$\left(cw'-Uw'+U'w\right)\bar{\rho}=-i\alpha p, \tag{A.5}$$

which may be written as

$$-\frac{w'}{U-c}+\frac{U'w}{(U-c)^2}=-\frac{i\alpha p}{\bar{\rho}\,(U-c)^2} \tag{A.6}$$

or in terms of a derivative as

$$\left[\frac{w}{U-c}\right]'=\frac{i\alpha p}{\bar{\rho}\,(U-c)^2} \tag{A.7}$$

Integrating both sides of (A.7) from $z_0-\varepsilon$ to $z_0+\varepsilon$ gives

$$\Delta\left[\frac{w}{U-c}\right]=\int_{z_0-\varepsilon}^{z_0+\varepsilon}\frac{i\alpha p}{\bar{\rho}\,(U-c)^2}\,dz \tag{A.8}$$

and since integrand on right hand side is at worst a step function, we get the first matching condition to be

$$\Delta\left[\frac{w}{U-c}\right]=0. \tag{A.9}$$

For the second matching condition we write equation (A.2) as

$$-i\alpha p'=\alpha^2(c-U)w\bar{\rho}-F^{-2}\frac{\bar{\rho}'w}{U-c}. \tag{A.10}$$

We differentiate equation (A.1) to get

$$-i\alpha p'=\left[(cw'-Uw'+U'w)\bar{\rho}\right]'. \tag{A.11}$$

Equating equation (A.10) and (A.11) gives

$$\begin{aligned}\left[(cw'-Uw'+U'w)\bar{\rho}\right]' &= \alpha^2(c-U)w\bar{\rho}-F^{-2}\frac{\bar{\rho}'w}{U-c}\\ &= \alpha^2(c-U)w\bar{\rho}+\left[F^{-2}\frac{\bar{\rho}w}{U-c}\right]'-F^{-2}\bar{\rho}\left[\frac{w}{U-c}\right]'\end{aligned}$$

and hence

$$\left[(cw'-Uw'+U'w)\bar{\rho}-F^{-2}\frac{\bar{\rho}w}{U-c}\right]'=\alpha^2(c-U)w\bar{\rho}-F^{-2}\bar{\rho}\left[\frac{w}{U-c}\right]'. \tag{A.12}$$

Integrating both sides of (A.12) from $z_0-\varepsilon$ to $z_0+\varepsilon$ gives

$$\Delta\left[\bar{\rho}\,(U-c)\,w'-\bar{\rho}U'w-F^{-2}\frac{\bar{\rho}w}{U-c}\right]=\int_{z_0-\varepsilon}^{z_0+\varepsilon}\left(\alpha^2\,(U-c)\,\bar{\rho}w-F^{-2}\bar{\rho}\left[\frac{w}{U-c}\right]'\right)dz. \tag{A.13}$$

The integrand on the right hand side of (A.13) is at worst a step function since $w/(U-c)$ is continuous. Hence the second matching condition is

$$\Delta\left[\bar{\rho}\,(U-c)\,w'-\bar{\rho}U'w-F^{-2}\frac{\bar{\rho}w}{U-c}\right]=0. \tag{A.14}$$

B Piecewise linaear dispersion relation for initial guesses in shoothing method

Consider the flow with basic velocity $U(z)$ profile given by (2.26). Solving Rayleigh equation (1.22) in each layer, where the layers are defined by the jumps at $z = \pm l$ gives

$$\phi(z) = \begin{cases} A\sinh\alpha(h_1 - z) & : l < z < h_1 \\ B\sinh\alpha z + C\cosh\alpha z & : |z| < l \\ D\sinh\alpha(h_2 + z) & : -h_2 < z < -l, \end{cases} \tag{B.1}$$

from which it follows that

$$\phi'(z) = \begin{cases} A(-\alpha)\cosh\alpha(h_1 - z) & : l < z < h_1 \\ B\alpha\cosh\alpha z + C\alpha\sinh\alpha z & : |z| < l \\ D\alpha\cosh\alpha(h_2 + z) & : -h_2 < z < -l. \end{cases} \tag{B.2}$$

In the upper layer at $z = l$, where the basic velocity profile is $U(z) = 1$ and $U'(z) = 0$, we have

$$\begin{aligned} \phi(l) &= A\sinh\alpha(h_1 - l) \\ \phi'(l) &= -\alpha A\cosh\alpha(h_1 - l). \end{aligned} \tag{B.3}$$

In the middle layer at $z = l$, where the basic velocity profile is $U(z) = \frac{z}{l}$ and $U'z) = \frac{1}{l}$, we have

$$\begin{aligned} \phi(l) &= B\sinh\alpha(\delta) + C.\cosh\alpha l \\ \phi'(l) &= \alpha B\cosh\alpha l + \alpha C\sinh\alpha l, \end{aligned} \tag{B.4}$$

and at $z = -l$, where the basic velocity profile is $U(z) = \frac{z}{l}$ and $U'(z) = \frac{1}{l}$, we have

$$\begin{aligned} \phi(-l) &= B.\sinh\alpha(-l) + C\cosh\alpha(-l) \\ \phi'(-l) &= \alpha B\cosh\alpha(-l) + \alpha C\sinh\alpha(-l). \end{aligned} \tag{B.5}$$

In the bottom layer at $z = -l$, where the basic velocity profile is $U(z) = -1$ and $U'(z) = 0$ we have

$$\phi(-l) = D \sinh \alpha(h_2 - l)$$
$$\phi'(-l) = +\alpha D. \cosh \alpha(h_2 - l). \tag{B.6}$$

B.0.0.1 Applying matching conditions at $z = l$

Applying first matching condition (1.29) between upper and middle layer at $z = l$, and with solutions to ϕ given by (B.3) and (B.4) yields to

$$(1-c)(-A\alpha \cosh \alpha(h_1 - l)) - 0 =$$
$$(1-c)(\alpha B \cosh \alpha l + \alpha C \sinh \alpha l) - \frac{1}{l}(B \sinh \alpha l + C \cosh \alpha l). \tag{B.7}$$

Applying second matching condition (1.32) between upper and middle layer at $z = l$, and with solutions to ϕ given by (B.3) and (B.4) yields to

$$\frac{A \sinh \alpha(h_1 - l)}{1-c} = \frac{B \sinh \alpha(l) + C \cosh \alpha l}{1-c}$$
$$\Rightarrow A = \frac{B \sinh \alpha(l) + C \cosh \alpha l}{\sinh \alpha(h_1 - l)}. \tag{B.8}$$

Substituting (B.8) into (B.7) gives

$$(1-c)(-\alpha)\frac{B \sinh \alpha l + C \cosh \alpha l}{\sinh \alpha(h_1 - l)} \cosh \alpha(h_1 - l) =$$
$$(1-c)(\alpha B \cosh \alpha l + C \sinh \alpha l) - \frac{1}{l}(B \sinh \alpha l + C \cosh \alpha l), \tag{B.9}$$

which can be rearranged as

$$\alpha(1-c)(B \sinh \alpha l + C \cosh \alpha l)\left(\frac{\cosh \alpha(h_1 - l)}{\sinh \alpha(h_1 - l)} + \frac{B \cosh \alpha l + C \sinh \alpha l}{B \sinh \alpha l + C \cosh \alpha l}\right)$$
$$= \frac{1}{l}(B \sinh \alpha l + C \cosh \alpha l), \tag{B.10}$$

giving us the result

$$\frac{B\cosh\alpha l + C\sinh\alpha l}{B\sinh\alpha l + C\cosh\alpha l} = \frac{1}{l\alpha(1-c)} - \frac{\cosh\alpha(h_1-l)}{\sinh\alpha(h_1-l)}. \tag{B.11}$$

By letting $Y_1 = \tanh\alpha(h_1 - l)$ we rewrite (B.11) as

$$\frac{B\cosh\alpha l}{B\sinh\alpha l + C\cosh\alpha l} + \frac{C\sinh\alpha l}{B\sinh\alpha l + C\cosh\alpha l} = \frac{1}{l\alpha(1-c)} - \frac{1}{Y_1}, \tag{B.12}$$

which we can be rearranged to

$$\frac{1}{\tanh\alpha l + \frac{C}{B}} + \frac{1}{\frac{B}{C} + \frac{1}{\tanh\alpha l}} = \frac{1}{l\alpha(1-c)} - \frac{1}{Y_1}. \tag{B.13}$$

We let $X = \tanh\alpha l$ and rewrite (B.13) as

$$\frac{1}{X + \frac{C}{B}} + \frac{1}{\frac{B}{C} + \frac{1}{X}} = \frac{1}{l\alpha(1-c)} - \frac{1}{Y_1}. \tag{B.14}$$

B.0.0.2 Applying matching conditions at $z = -l$

Applying first matching condition (1.29) between middle and bottom layer at $z = -l$, and with solutions to ϕ given by (B.5) and (B.6) yields to

$$\begin{aligned}(-1-c)(\alpha D\cosh\alpha(h_2-l)) - 0 = \\ (-1-c)(\alpha B\cosh\alpha(-l) + \alpha C\sinh\alpha(-l)) - \frac{1}{l}(B\sinh\alpha(-l) + C\cosh\alpha(-l)).\end{aligned} \tag{B.15}$$

Applying second matching condition (1.32) between middle and bottom layer at $z = -l$, and with solutions to ϕ given by (B.5) and (B.6) yields to

$$\begin{aligned}\frac{D\sinh\alpha(h_2-l)}{-1-c} &= \frac{B\sinh\alpha(-l) + C\cosh\alpha(-l)}{-1-c} \\ \Rightarrow D &= \frac{B\sinh\alpha(-l) + C\cosh\alpha(-l)}{\sinh\alpha(h_2-l)}.\end{aligned} \tag{B.16}$$

Substituting (B.16) into (B.15) gives

$$(-1-c)(\alpha)\frac{B\sinh\alpha(-l)+C\cosh\alpha(-l)}{\sinh\alpha(h_2-l)}\cosh\alpha(h_2-l)= \\ (-1-c)(\alpha B\cosh\alpha(-l)+C\sinh\alpha(-l))-\frac{1}{l}(B\sinh\alpha(-l)+C\cosh\alpha(-l)), \tag{B.17}$$

which can be rearranged to give

$$\alpha(-1-c)(B\sinh\alpha(-l)+C\cosh\alpha(-l))\left(\frac{\cosh\alpha(h_2-l)}{\sinh\alpha(h_2-l)}-\frac{B\cosh\alpha(-l)+C\sinh\alpha(-l)}{B\sinh\alpha(-l)+C\cosh\alpha(-l)}\right) \\ =\frac{-1}{l}(B\sinh\alpha(-l)+C\cosh\alpha(-l)), \tag{B.18}$$

from which it follows that

$$\frac{B\cosh\alpha(-l)+C\sinh\alpha(-l)}{B\sinh\alpha(-l)+C\cosh\alpha(-l)}=\frac{1}{l\alpha(-1-c)}+\frac{\cosh\alpha(h_2-l)}{\sinh\alpha(h_2-l)}. \tag{B.19}$$

By letting $Y_2=\tanh\alpha(h_2-l)$ we rewrite (B.19) as

$$\frac{B\cosh\alpha(-l)}{B\sinh\alpha(-l)+C\cosh\alpha(-l)}+\frac{C\sinh\alpha(-l)}{B\sinh\alpha(-l)+C\cosh\alpha(-l)}=\frac{1}{l\alpha(-1-c)}+\frac{1}{Y_2}, \tag{B.20}$$

which can be simplified as

$$\frac{1}{\tanh\alpha(-l)+\frac{C}{B}}+\frac{1}{\frac{B}{C}+\frac{1}{\tanh\alpha(-l)}}=\frac{1}{l\alpha(-1-c)}+\frac{1}{Y_2}. \tag{B.21}$$

Letting $X=\tanh\alpha l$, and with the use of identity $\tanh(-\alpha l)=-\tanh\alpha l=-X$ we rewrite (B.21) as

$$\frac{1}{-X+\frac{C}{B}}+\frac{1}{\frac{B}{C}-\frac{1}{X}}=\frac{1}{l\alpha(1-c)}+\frac{1}{Y_2}. \tag{B.22}$$

B.0.0.3 combining results (B.14) and (B.22)

Letting $\frac{B}{C} = E$ in (B.14) and (B.22) leads to system of two equations given bellow

$$\frac{1}{X + \frac{1}{E}} + \frac{1}{E + \frac{1}{X}} = \frac{1}{l\alpha(1-c)} - \frac{1}{Y_1} \tag{B.23}$$

$$\frac{1}{-X + \frac{1}{E}} + \frac{1}{E - \frac{1}{X}} = \frac{1}{l\alpha(-1-c)} + \frac{1}{Y_2}, \tag{B.24}$$

which can be rearranged to give

$$\frac{E}{EX+1} + \frac{X}{EX+1} = \frac{1}{l\alpha(1-c)} - \frac{1}{Y_1} \tag{B.25}$$

$$\frac{E}{-EX+1} + \frac{X}{EX-1} = \frac{1}{l\alpha(-1-c)} + \frac{1}{Y_2}, \tag{B.26}$$

from which it follows that

$$\frac{E+X}{EX+1} = \frac{1}{l\alpha(1-c)} - \frac{1}{Y_1} \tag{B.27}$$

$$\frac{E-X}{1-EX} = \frac{1}{l\alpha(-1-c)} + \frac{1}{Y_2}. \tag{B.28}$$

We can further simplify (B.27) and (B.28) as follows

$$E + X = (EX+1)\left(\frac{1}{l\alpha(1-c)} - \frac{1}{Y_1}\right) \tag{B.29}$$

$$E - X = (1-EX)\left(\frac{1}{l\alpha(-1-c)} + \frac{1}{Y_2}\right), \tag{B.30}$$

allowing to express the constant E as

$$E = \frac{\frac{1}{\alpha l(1-c)} - \frac{1}{Y_1} - X}{1 + \frac{X}{Y_1} - \frac{X}{\alpha l(1-c)}} \tag{B.31}$$

$$E = \frac{\frac{1}{\alpha l(-1-c)} + \frac{1}{Y_2} + X}{1 + \frac{X}{Y_2} + \frac{X}{\alpha l(-1-c)}}. \tag{B.32}$$

B.0.0.4 Dispersion relation

Equating the results (B.31) and (B.32) yields to

$$\frac{\frac{1}{\alpha l(1-c)} - \frac{1}{Y_1} - X}{1 + \frac{X}{Y_1} - \frac{X}{\alpha l(1-c)}} = \frac{\frac{1}{\alpha l(-1-c)} + \frac{1}{Y_2} + X}{1 + \frac{X}{Y_2} + \frac{X}{\alpha l(-1-c)}}. \tag{B.33}$$

Multiplying left-hand side by $\frac{Y_1 \alpha l(1-c)}{Y_1 \alpha l(1-c)}$ and right-hand side by $\frac{Y_2 \alpha l(-1-c)}{Y_2 \alpha l(-1-c)}$ gives

$$\frac{Y_1 - \alpha l + \alpha l c - X Y_1 \alpha l + X Y_1 \alpha l c}{Y_1 \alpha l - Y_1 \alpha l c + X \alpha l - X \alpha l c - X Y_1} = \frac{Y_2 - \alpha l - \alpha l c - X Y_2 \alpha l - X Y_2 \alpha l c}{-Y_2 \alpha l - Y_2 \alpha l c - X \alpha l - X \alpha l c + X Y_2}. \tag{B.34}$$

Factorising the velocity c yields to dispersion relation

$$\frac{c(\alpha l + X Y_1 \alpha l) + Y_1 - \alpha l - X Y_1 \alpha l}{c(-Y_1 \alpha l - X \alpha l) + Y_1 \alpha l + X \alpha l - X Y_1} = \frac{c(-\alpha l - X Y_2 \alpha l) + Y_2 - \alpha l - X Y_2 \alpha l}{c(-Y_2 \alpha l - X \alpha l) - Y_2 \alpha l - X \alpha l + X Y_2}, \tag{B.35}$$

or

$$\frac{c(\alpha l + X Y_1 \alpha l) + Y_1 - \alpha l - X Y_1 \alpha l}{c(-Y_1 \alpha l - X \alpha l) + Y_1 \alpha l + X \alpha l - X Y_1} + \frac{c(-\alpha l - X Y_2 \alpha l) + Y_2 - \alpha l - X Y_2 \alpha l}{-c(-Y_2 \alpha l - X \alpha l) + Y_2 \alpha l + X \alpha l - X Y_2} = 0, \tag{B.36}$$

which can be used for initial guesses for numerical calculations, and where $X = \tanh \alpha l$, $Y_2 = \tanh \alpha(h_2 - l)$ and $Y_1 = \tanh \alpha(h_1 - l)$. Hence, for example, rescaling the above dispersion relation to a co-flow with $h_1 = 10$ and $h_2 = 25$, gives dispersion relation shown in figure B.1 shown below.

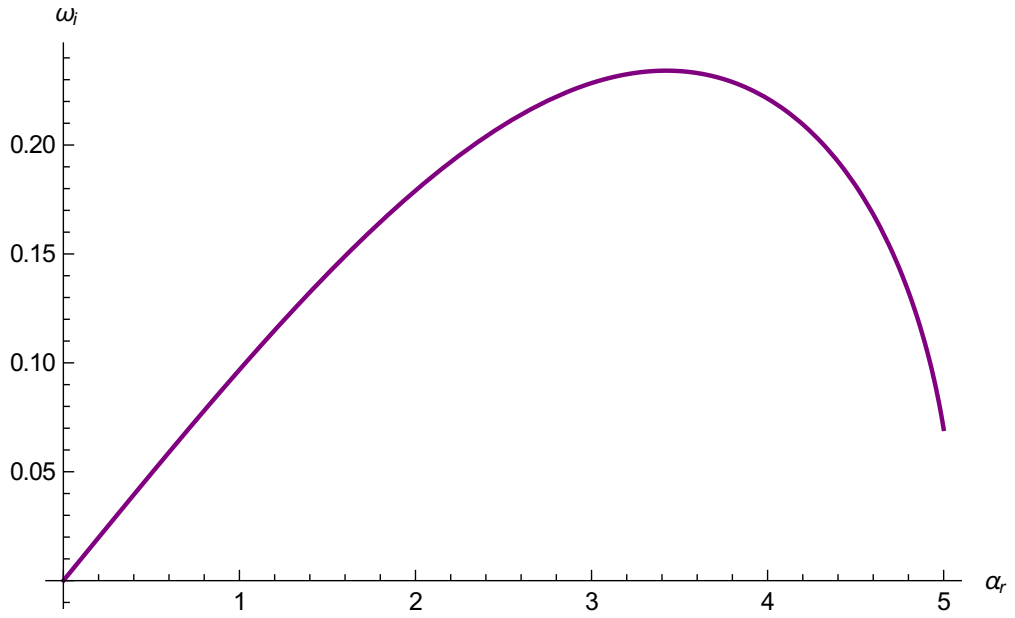

Figure B.1: Dispersion relation ω_i as function of wavenumber α given by (B.36) for initial guesses of shooting method for numerical calculations.

C Mathematica code for calculating temporal stability results

C.1 Functions

To solve the Taylor -Goldstein equation (1.17) numerically in Mathematica [9] we set a functions describing the velocity $U(z)$ ($U[z]$ in the code) and density $\rho(z)$ ($Ro[z]$ in the code) profiles, where ru, rb are the upper layer and bottom layer densities respectively and $h0$ is the displacement of strongest velocity gradient relative to strongest density gradient. We also define a Froude's number function ($FF[V, G, L]$ in the code) which depends on the scaling quantities for speed V, length L and the magnitude of gravity G .

```
FF[V_, G_, L_] = V/Sqrt[G  L];
U[z_] = (1+Tanh[5z])/2
Rrro[R1_, z_, ru_, rb_, h0_] = (
  rb + ru + (-rb + ru) Tanh[R1 (z - h0)])/(rb + ru);
Ro[z_] = Rrro[5, z, 1030, 1029.7, 0];
```

C.2 Parameters

We next set the parameters for Froude's number F, Global Richardson number $J0$, and the wavenumber α (a in the code). Note that in the case of temporal stability analysis the wavenumber is a real quantity, and in the case of Absolute or Global stability analysis the wavenumber is a complex quantity.

```
F = FF[1, 9.81, 1];
d = (1 - 1029.7/1030)/(1 + 1029.7/1030) // N
J0 = d F^(-2)
a = 0.25
```

C.3 Upper layer solution

We integrate the upper solution from the upper boundary (*bup* in the code) to zero which in our case is set in the middle of the velocity shear. The upper boundary is to satisfy the so-called rigid lid boundary. In the case of temporal and absolute stability analysis this boundary condition is purely real. In the case of Global stability analysis this boundary condition is also real since the global variation is considered due to variation of bottom boundary.

```
solup[c_] :=
  NDSolve[{(U[z] - c) (v''[z] - a^2 v[z]) - D[D[U[z], z], z] v[z] -
      v[z]/(F^2 (U[z] - c)) (D[Ro[z], z]/Ro[z]) + (D[Ro[z], z]/
         Ro[z]) ((U[z] - c) v'[z] - D[U[z], z] v[z]) == 0,
    v[bup] == 0, v'[bup] == 1}, v, {z, 0, bup}];
```

C.4 Bottom layer solution

We integrate the bottom solution from the bottom boundary h_2 ($bbot + i\,hi$ in the code) to zero which in our case is set in the middle of the velocity shear. The bottom boundary is to satisfy the solid wall boundary condition. In the case of temporal and absolute stability analysis this boundary condition is purely real. In the case of Global stability analysis this boundary condition is complex. The solution for v below the shear layer is $v = \sinh[\alpha(z + h_2)]$, $v' = \alpha \cosh[\alpha(z + h_2)]$ regardless of whether h_2 is real or complex. These expressions are used to obtain the initial conditions at $z = -bbot$, and therefore, $v[z = -bbot]$ is not zero and $v'[z = -bbot]$ is not 1. In such case $v[-bbot] = \sinh[i\,hi\,\alpha]$ and $v'[-bbot] = \alpha \cosh[i\,hi\,\alpha]$, where $bbot$ and hi are the real and imaginary parts respectively of the complex value of the distance of the bottom boundary. Note that in all of our considered stability analysis (temporal, absolute and global) the integration path stays on the real $z-$axis since we are calculating the unstable solutions for which the phase speed c is a complex quantity and hence the singularity of the Taylor-Goldstein equation (1.17) lies in the complex $z-$plane. In addition the integration path for global stability calculations also stays on the real $z-$axis as in such case there is only additional requirement of satisfying complex boundary condition, which does not require to deform the integration path into complex $z-$plane. Such complex boundary condition

modifies the value of the phase speed c for different value of hi. The integration path is always on real axis and this gives the physical solution because the path must lie bellow critical points according to Lin's rule (see Lin 1955), and this is the case for unstable waves when the path is on real axis. This is still the case when $h_2 = bbot + i\,hi$ (distance of the bottom boundary) is complex.

```
soldown[c_] :=
  NDSolve[{(U[z] - c) (v''[z] - a^2 v[z]) - D[D[U[z], z], z] v[z] -
      v[z]/(F^2 (U[z] - c)) (D[Ro[z], z]/Ro[z]) + (D[Ro[z], z]/
         Ro[z]) ((U[z] - c) v'[z] - D[U[z], z] v[z]) == 0,
    v[-bbot] == Sinh[I hi a], v'[-bbot] == a Cosh[I hi a]}, v, {z, 0, -bbot}];
```

C.5 Error function at the matching of Upper and bottom layer solutions (at $z = 0$)

We define an error function $g(c)$ which matches the upper and bottom layer solution at the middle of the velocity shear, which in our case is at $z = 0$.

```
g[c_] := (v[0] /. soldown[c][[1]]) (v'[0] /.
     solup[c][[1]]) - (v[0] /. solup[c][[1]]) (v'[0] /.
     soldown[c][[1]])
```

C.6 Initial guesses of phase speed c for shooting method

For shooting method we require two initial guesses of the eigenvalue c. These values have to sufficiently close to resultant value for the code to converge. For the initial

guesses of temporal stability analysis the results from piecewise linear theory is used.

```
c1 = -0.85 + 0.01 I;
c2 = -0.88 + 0.011 I;
```

C.7 Secant method to find c to desired accuracy

With the use of the error function $g(c)$ we use the secant method which is repeated until the difference between two consequent values of c is sufficiently small (in our case the relative tolerance is $\Delta c/c < 10^{-4}$ which yields to $c(n) - c(n+1) < 10^{-6}$).

```
c3 = (g[
      c1] c2 - g[c2] c1)/(g[c1] - g[c2])
c4 = (g[c2] c3 - g[c3] c2)/(g[c2] - g[c3])
c5 = (g[c3] c4 - g[c4] c3)/(g[c3] - g[c4])
.
.
.
```

This process is then repeated for all considered wavenumbers in case of temporal and absolute stability analysis for $\alpha + \Delta\alpha$, where we fix $\Delta\alpha = 1/1000$. In the calculations of Global stability results this has to be in addition repeated for all considered values of the complex part of the boundary condition (hi in the code) on grid $\Delta hi = 1/1000$.

Bibliography

[1] L. Kelvin, "Hydrokinetic solutions and observations.," *Phil.Mag.*, vol. 42, pp. 362–377, 1871.

[2] H. Helmhotlz, "On discontinuous movement of fluids.," *Phil.Mag.*, vol. 36, pp. 337–346, 1868.

[3] O. Reynolds, *An experimental investigation of the circumstances which determine whether the motion of water in parallel channels shall be direct or sinuous and of the law of resistance in parallel channels.* Cambridge University Press, 1883.

[4] L. Rayleigh, "On the stability of jets.," *Proc.London Mtah.Soc.*, vol. 10, pp. 4–13, 1879.

[5] V. Shrira and P. Forget, "On the nature of near-inertial oscillations in the uppermost part of the ocean and possible route towards HF radar probing of stratification," *J. of Physical Oceanography*, vol. 45, pp. 2660–2678, 2015.

[6] P. Drazin and W. Reid, *Hydrodynamic stability.* Cambridge University Press, 1981.

[7] A. Nayfeh, *Introduction to perturbation techniques.* Wiley, 1973.

[8] M. Van Dyke, *Perturbation methods in fluid mechanics.* Parabolic Press, 1975.

[9] Mathematica, "http://www.wolfram.com/products/."

[10] I. The MathWorks, "Matlab."

[11] J. Turner, *Buoyancy effects in fluids.* Cambridge University Press, 1973.

[12] P. Huerre, "Open shear flow instabilities. ," *In Perspective in Fluid Dynamics, by G. K. Batchelor, H. K. Moffatt and M. G. Worster*, CUP. 2000.

[13] H. Squire, "On the stability of three dimensional disturbances of viscous flow between parallel walls," *Proc. Roy. Soc.*, vol. 142, pp. 621–628, 1933.

[14] G. Taylor, "Effect of variation in density on the stability of superposed streams of fluid," *Proc. Roy. Soc.*, vol. 132, pp. 499–523, 1931.

[15] J. Holmboe, "On behaviour of symetric waves in stratified shear layers," *Geophys.Publ.*, vol. 24, pp. 67–113, 1962.

[16] C. Caulfield, "Multiple linear instability of layered stratified shear flow," *J. Fluid Mech.*, vol. 258, pp. 255–285, 1993.

[17] P. Schmid and H. D.S., *Stability and transition in shear flows.* Springer, N.Y., 2001.

[18] R. Briggs, *Electron-Stream Interaction with Plasmas.* MIT Press, 1964.

[19] P. Huerre and P. Monkewitz, "Absolute and convective instabilities in free shear layers," *J. Fluid Mech.*, vol. 159, pp. 151–168, 1985.

[20] P. Huerre and P. Monkewitz, "Local and global instabilities in spatially developing flows," *Annu. Rev. Fuid Mech.*, vol. 1, pp. 473–537, 1990.

[21] J. Healey, "Enhancing the absolute instability of a boundary layer by adding a far away plate," *J. Fluid Mech.*, vol. 579, pp. 29–61, 2007.

[22] J. Healey, "Destabilizing effects of confinement on homogeneous mixing layers," *J. Fluid Mech.*, vol. 623, pp. 241–271, 2009.

[23] C. Arratia, S. Mowlavi and F. Gallaire "Absolute/convective instabilities and the role of confinement in free shear layers.," *Physics.Flu-Dyn.*, arXiv:1707.07558v1, 2017.

[24] M. Juniper, "The effect of confinement on the stability of two-dimensional shear flows.," *J.Fuid Mech.*, vol. 565, pp. 171–195, 2006.

[25] M. Juniper, "The full-impulse response of two-dimensional jet/wake flows and implications for confinement.," *J.Fuid Mech.*, vol. 590, pp. 163–185, 2007.

[26] A. Soward and C. A. Jones, "The linear stability of the floww in narrow gap between two cocentric rotating spheres.," *Quart. J. Mech. Appl. Math.*, vol. 36, pp. 19–42, 1983.

[27] P. Huerre and M. Rossi, "Hydrodynamic instabilities in open flows," *In C. Godrche and P. Manneville (Eds.), Hydrodynamics and Nonlinear Instabilities (Collection Alea-Saclay: Monographs and Texts in Statistical Physics*, no. CUP, pp. 81–294, 1998. Cambridge University Press.

[28] C. Davies and P. Carpenter, "Global behaviour corresponding to the absolute instability of rotating boundary layers.," *J.Fuid Mech.*, vol. 486, pp. 287–329, 2003.

[29] C. Davies and C. Thomas, "Global stability of the rotating disc boundary layer.," *J. Eng. Math.*, vol. 57(3), pp. 219–236, 2007.

[30] C. Davies and C. Thomas, "The effects of mass transfer on the global stability of the rotating disk boundary layer.," *J.Fuid Mech.*, vol. 663, pp. 401–433, 2010.

[31] C. Davies and C. Thomas, "Global stability of the rotating disk boundary layer with an axial magnetic field.," *J.Fuid Mech.*, vol. 724, pp. 510–526, 2013.

[32] C. Davies and C. Thomas, "Global stability behaviour for the BEK family of rotating boundary layers.," *Theo. Comput. Fluid Dyn.*, vol. 31, pp. 519–536, 2016.

[33] S. Chandrasekhar, *Hydrodynamic and Hydromagnetic Stability.* Oxford, 1961.

[34] A. Soloviev and L. R., *The Near-Surface Layer of the Ocean: Structure, Dynamics and applications.* Springer, 2014.

[35] J. Matas, "Inviscid versus viscous instability mechanism of an air-water mixing layer.," *J. Fluid Mech.*, vol. 768, pp. 375–387, 2015.

[36] G. Lawrence and L. Redekopp, "The stability of sheared density interface," *Phys. Fluids.*, vol. A3, pp. 2360–2370, 1991.

[37] J. Healey, Magic course module *Hydrodynamics stability* . "http://maths-magic.ac.uk/courses.php", 2017.

[38] M. Gaster, "A note on the relation between temporally-increasing and spatially-increasing disturbances in hydrodynamic stability," *J. Fluid Mech.*, vol. 14, pp. 222–224, 1962.

[39] C. Lin, *The theory of hydrodynamics stability.* Cambridge University Press, 1955.

[40] M. Gaster, "On the effects of boundary layer growth on flow stability," *J. Fluid Mech.*, vol. 66, pp. 465–480, 1974.

[41] F. Smith, "On the non-parallel flow stability of the Blasius boundary layer," *Proc. R. Soc. Lond.*, vol. A 366, pp. 91–109, 1979.

[42] F. Bertolottti, T. Herbert and T. Spalart, "Linear and nonlinear stability of Blasius boundary layer," *J. Fluid Mech.*, vol. 242, pp. 441–474, 1992.

[43] E. Strang and H. Fernando, "Entrainment and mixing in stratified shear flows.," *J.Fuid Mech.*, vol. 428, pp. 349–386, 2001.

[44] G. Lawrence and S. Haigh, "Symmetric and nonsymmetric Holmboe instabilities in an inviscid flow," *Physical processes in Lakes and Oceans*, vol. 54, pp. 295–304, 1999.

[45] J. Taylor, "Numerical simulations of the stratified oceanic bottom boundary layer.," *PhD Thesis.*, University of California, 2008.